Twisted bilayer graphene probed with nano-optics

Sai Swaroop Sunku

Submitted in partial fulfillment of the
requirements for the degree of
Doctor of Philosophy
under the Executive Committee
of the Graduate School of Arts and Sciences

COLUMBIA UNIVERSITY

2021

Abstract

Twisted bilayer graphene probed with nano-optics

Sai Swaroop Sunku

The discovery of strongly correlated electronic phases in twisted bilayer graphene has led to an enormous interest in twisted van der Waals (vdW) heterostructures. While twisting vdW layers provides a new control knob and never before seen functionalities, it also leads to large spatial variations in the electronic properties. Scanning probe experiments are therefore necessary to fully understand the properties of twisted vdW heterostructures.

In this thesis, we studied twisted bilayer graphene (TBG) with two scanning probe techniques at two twist angle regimes. At small twist angles, our nano-infrared images resolved the spatial variations of the electronic structure occurring within a Moiré unit cell and uncovered a quantum photonic crystal. Meanwhile, with nano-photocurrent experiments, we resolved DC Seebeck coefficient changes occurring in domain walls on nanometer length scales. At larger twist angles, we mapped the twist angle variations naturally occurring in our device with a combination of nano-photocurrent and nano-infrared imaging. Finally, we also investigated different materials for use as nano-optics compatible top gates in future experiments on TBG. Our results demonstrate the power of nano-optics techniques in uncovering the rich, spatially inhomogeneous physics of twisted vdW heterostructures.

Table of Contents

Acknowledgments iii

Chapter 1: Introduction 1

1.1 Graphene and twisted bilayer graphene 1

1.2 Scattering SNOM and plasmon polaritons 7

1.3 Photocurrent and nano-photocurrent in graphene 11

1.4 Outline 13

Chapter 2: Quantum Photonic Crystal 16

2.1 Introduction 16

2.2 Nano-infrared imaging of single domain walls 19

2.3 Nano-infrared imaging of the quantum photonic crystal 20

2.4 Modeling and tunability of the photonic crystal 22

2.5 Conclusion 25

2.6 Supplementary Material 26

Chapter 3: Mapping the Twist Angle with Nano-Optics 43

3.1 Introduction 43

3.2 Nano-photocurrent at the interface between twisted bilayer and monolayer graphene 45

3.3 Nano-infrared measurements of large angle twisted bilayer graphene 51

3.4 Interband transitions and twist angle dependent nano-infrared signal 54

3.5 Conclusion 56

3.6 Supplementary Material 56

Chapter 4: Domain walls and their photocurrent response 70

4.1 Introduction 70

4.2 Photocurrent imaging at $\boldsymbol{\omega = 900\ cm - 1}$ 72

4.3 Photocurrent imaging at frequencies within the Reststrahlen band of hBN 77

4.4 Conclusion 81

4.5 Supplementary Material 82

Chapter 5: Nano-optics compatible top gates 96

5.1 Introduction 96

5.2 Strengths and weaknesses of a MoS_2 top gate 100

5.3 Strengths and weaknesses of a monolayer graphene top gate 104

5.4 Direct comparison between MoS_2 and monolayer graphene top gates 106

5.5 Supplementary material 108

Concluding Remarks 121

References 122

Acknowledgments

First and foremost, I would like to thank my advisor Prof. Dmitri Basov. Dmitri is a brilliant scientist, a mentor par excellence and a tireless leader. His empathetic approach brings out the best in all of us. I am immensely grateful to have worked in his group. I'm also grateful to Prof. Cory Dean for letting me work in his lab during the first two years of my PhD and for serving on my dissertation committee. I would also like thank Prof. Latha Venkataraman, Prof. Aron Pinczuk and Prof. Nanfang Yu for graciously agreeing to serve on my committee.

None of the experiments reported here would have been possible without our collaborators who produced the devices we needed before we did any work. The data in Chapters 2, 3, and parts of Chapter 5 are from devices produced by Hyobin Yoo and Rebecca Enegelke in the group of Prof. Philip Kim. The data in Chapter 4 are from a device produced by Shaowen Chen and Derick E. Gonzalez-Acevedo in group of Prof. Cory Dean. Some of the data in Chapter 5 are from devices produced by Nate Finney, Nicola Curreli and Cheng Tan in the group of Prof. James Hone.

I'm privileged and lucky to have worked with several amazing scientists during my time in the Basov Lab. Guangxin Ni and Alex Frenzel taught me the foundations of nano-optics experiments on graphene. Aaron Sternbach showed me that it's always possible to align to two irises. Alex McLeod was an endless source of inspiration and new ideas. Dorri Halbertal was a wise and knowledgeable mentor. Yinming Shao, Lin Xiong, Rocco Vitalone, Sam Moore, Frank Ruta, Ran Jing, Dan Rizzo and Mike Berkowitz, thank you for being wonderful colleagues. Thanks to Judy Winstead and Karen Canaan for reimbursing my conference trips. Thanks also to the staff in the physics department, John Carr, Jennifer Chiu, Michael Adan and Sonnia Andrade for placing

my last minute orders and to the staff in APAM, Montse Fernandez-Pinkley and David Barrera, for making sure I was registered for the right courses.

Collecting experimental data is often only a fraction of the struggle. Understanding and interpreting it is the bigger problem. For solving this bigger problem, I have to thank the group of Prof. Misha Fogler and Tobias Stauber at CSIC in Madrid. Misha and his students Bor-Yuan Jiang and Andrey Rikhter developed models to explain much of our results. Tobias was always willing to do more calculations even if he had already done too many.

I've learned much from scientists in other groups at Columbia including Prof. Abhay Pasupathy, Apoorv Jindal (sorry CNTs didn't work out), Alex Kerelsky, Rebeca Ribeiro-Palau, En-Min Shih, Andrew Wieteska, Yihang Zeng, Julia Zhang and many others. Thank you for sharing your expertise freely.

My time at Columbia was made memorable by the people I met outside the lab. Andriy and Reeto, thank you for everything. Yi, Anthony, Mihir and Akhilesh, thank you for always cheering me up. John, thanks for the road trip and the board games. Mel and E-Dean, thank you for hanging out way too late after APAM Fridays and for introducing me to Broadway. Thanks also to Raj, Diana, Mirella, Yiting, Kevin, and the rest of the OSA/SPIE student chapter for all the outreach work we did. Andrew and E-Dean, I couldn't have gotten a job without you!

Last and never the least, I thank my family. I thank my parents for their innumerable sacrifices. Sumanth babai and Latha pinni, you're a second family to me. Sravanthi, thank you for making the lockdown bearable and even fun at times. Jasmine, thank you for the never ending support and the silliest of jokes. I could not have completed the PhD journey without all of you.

Chapter 1: Introduction

Optical spectroscopy has established itself as a powerful and insightful probe of the wide variety of electronic phases in condensed matter systems (*1*). In conventional optical spectroscopy, the diffraction limit determines the size of the smallest observable features. Recent developments in nano-optics have led to sub-diffractional probes that can achieve orders of magnitude better spatial resolution. In this thesis, we use such a deeply sub-diffractional technique known as scattering scanning near-field optical microscopy (scattering SNOM) (*2*, *3*) and a closely related variant, nano-photocurrent imaging (*4*), to study twisted bilayer graphene (TBG).

1.1 Graphene and twisted bilayer graphene

1.1.1 Graphene, two-dimensional materials and van der Waals heterostructures

Graphene is an allotrope of carbon consisting of atomically-thin two-dimensional sheets. Graphite, the more commonly known carbon allotrope, can be thought of as layers of graphene stacked over each other. Monolayer graphene, consisting of a single sheet of carbon atoms, was first isolated in 2004 (*5*) and has been extensively investigated in the years since (*6*, *7*). Graphene sheets with multiple layers such as bilayer and trilayer graphene have also been comprehensively studied. In this chapter, we focus on monolayer graphene (MLG) and bilayer graphene (BLG).

Monolayer graphene consists of carbon atoms arranged in a honeycomb lattice, as shown in Fig 1.1(A). The low-energy band structure consists of cones located at the K and K' points in the Brillouin zone (BZ) (Fig 1.1(B)). Because the linear energy dispersion is reminiscent of the solution to the Dirac's equation, the cones are often called Dirac cones. The K and K' points are also referred to as different valleys. Bilayer graphene (BLG) consists of two graphene sheets (Fig

1.1(C)). The electronic structure of BLG is tunable with electric field. Fig 1.1(D) shows a schematic of the BLG band structure for different combinations of displacement fields above and below the graphene layer. With no displacement fields, the band structure at low energies is approximately parabolic (*8*). If equal displacement fields are applied above and below the graphene layer, a finite band gap Δ is opened (*8*–*10*). The carrier density in the BLG layer can be controlled independently of Δ by the difference between the top and bottom electric fields. Typically, such electric fields are applied by metallic gates placed above and below the graphene layer.

Research into graphene has led to the discovery of a broad variety of two-dimensional (2D) materials. A very incomplete list includes hexagonal boron nitride (hBN), semiconductors such as the transition metal dichalcogenides (TMDs) MoS_2 and WS_2, superconductors such as $NbSe_2$, and ferromagnets such as CrI_3 (*11*). 2D materials can be isolated to form atomically thin sheets because the atoms within the layers form strong covalent bonds and the layers themselves are held together by weak van der Waals forces. 2D materials have attracted intense interest because their properties are highly tunable. The extremely thin nature of 2D materials allows their properties to be easily modified by electrostatic gates, as demonstrated above for the case of bilayer graphene. Because 2D materials have no 'dangling bonds' in the third dimension, they can be arbitrarily stacked over other 2D materials with no concerns of lattice mismatch. Such heterostructures, called van der Waals (vdW) heterostructures (Fig 1.1(E)) (*12*), have drawn comparison to an atomic scale LEGO set.

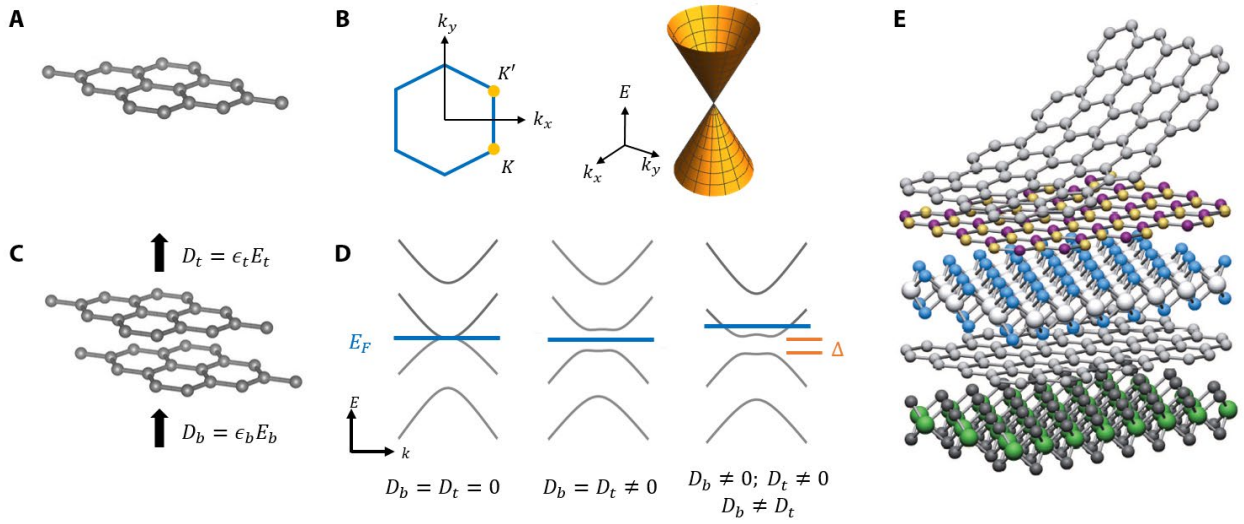

Figure 1.1 | Electronic structure of monolayer and bilayer graphene. (A) Schematic of the atomic structure of monolayer graphene. The grey circles represent carbon atoms. (B) Left: The first Brillouin zone of MLG. The special points known as the K and K' points are marked in orange. Right: A schematic of the low energy band structure of MLG at the K and K' points. (C) Schematic of the atomic structure of naturally occurring bilayer graphene. D_b (D_t), ϵ_b (ϵ_t) and E_b (E_t) refer to the displacement field, dielectric constant and electric field below and above the graphene layer. (D) Schematic of the low energy band structure close to K and K' points for different configurations of displacement fields. E_F is the Fermi energy and Δ is the energy gap. (E) Schematic illustration of van der Waals heterostructures. Figure from (*12*).

1.1.2 Twisted bilayer graphene and its electronic structure

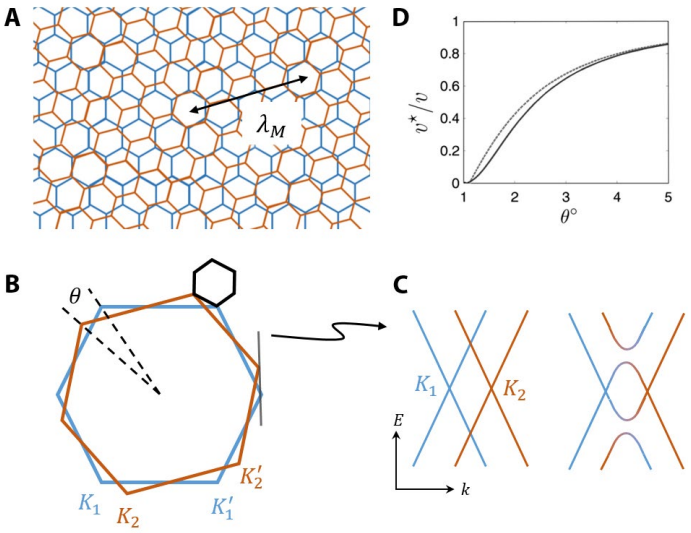

Figure 1.2 | Twisted bilayer graphene at large twist angles. (A) Schematic depiction of two twisted graphene sheets. The periodicity of the resulting moiré pattern λ_M is also depicted. (B) The Brillouin zone of TBG. The BZs of the individual graphene layers rotated by twist angle θ are represented as blue and red hexagons respectively. The K and K' points of the individual layers are also marked. The BZ of the resulting TBG structure is the smaller black hexagon. The band structure along the grey line is shown in (C). (C) Schematic band structure of TBG without (left) and with (right) interaction between the two MLG layers. (D) A plot of the reduced Fermi velocity of TBG for twist angles above the first magic angle. v^* and v are the Fermi velocities of TBG and MLG respectively. Figure from (*13*).

A recent development in the field of two-dimensional materials is the discovery of yet another control knob for tuning the electronic properties of vdW heterostructures: the relative twist angle between neighboring layers. Graphene and hBN have the same crystal structure but with a slightly different lattice constant. Placing graphene on a hBN substrate leads to a long-range

periodic pattern called a moiré pattern. At small twist angles, a bandgap appears in MLG and a long-sought phenomena known as the Hofstadter's Butterfly has been observed (*14–17*).

Bistritzer and MacDonald were the first to apply a similar principle to two sheets of graphene (*13*). They predicted that when two graphene layers are twisted relative to each other (Fig 1.2(A)), the band structure of the resulting heterostructure is dramatically affected (*13*). Specifically, they predicted that at low energies, the electronic structure of twisted bilayer graphene resembles that of monolayer graphene but with a smaller, twist angle-dependent Fermi velocity (Fig 1.2(D)). This change in Fermi velocity is the direct result of hybridization between the Dirac cones in neighboring graphene layers (Fig 1.2(C)). They also predicted that at a series of 'magic' twist angles, the Fermi velocity would approach zero, leading to localized carriers and the possibility of strongly correlated phenomena.

The dramatic confirmation of these predictions in 2018 by the group of Pablo Jarillo-Herrero, who discovered correlated Mott-like insulating states (*18*) and superconductivity (*19*) at the first magic angle of $\theta \sim 1.1°$ has fueled enormous interest in TBG and twisted vdW heterostructures. Further experiments have discovered strange metal behavior (*20*), nematicity (*21*), ferromagnetism (*22*) and quantum anomalous Hall behavior (*23*) in TBG. Similar experiments on twisted TMDs have also discovered correlated insulating states (*24*).

The schematic in Fig 1.2(A) assumes that the graphene layers are perfectly rigid, which is a reasonable approximation for twist angles much greater than 1 degree. At smaller twist angles, transmission electron microscopy (TEM) images show a domain structure separated by domain walls (Fig 1.3(B)). Large scale elastic simulations show that the formation of the domains is driven by the difference in the stability of different atomic stackings in bilayer graphene (Fig 1.3(A)) (*25*, *26*). The most stable stacking for bilayer graphene is called the Bernal stacking or AB/BA stacking

(Fig 1.3(A)). This stacking is realized in bulk graphite and entails half of the carbon atoms in top layer (A sublattice) lying directly above carbon atoms in the bottom layer (B sublattice). Since the A and B sublattices are labeled arbitrarily, AB and BA stacking simply correspond to a switching of the sublattices. In AA stacking, all carbon atoms in the top layer lie directly on top of other carbon atoms in the bottom layer (Fig 1.3(A)). AA stacking is known to be less stable than Bernal stacking. Therefore, the minimal energy TBG structure maximizes the area of the AB and BA domains and minimizes the area of the AA stacked regions. This shrinking of AA domains and expansion of AB and BA domains is also termed atomic relaxation.

Atomic relaxation also modifies the electronic structure of small angle TBG. Bernal stacked BLG is topologically trivial with a total Chern number of 0. However, when Bernal stacked BLG is gapped, the Chern number at the K and K' valleys are 1 and -1 respectively (*27*). At the interface between AB and BA stacking, the Chern number changes by a total of 2 at each valley. Therefore, two topologically protected states must be localized to the boundary (*27–30*) per valley.

Such domain walls between AB and BA stacking also occur as defects in naturally exfoliated bilayer graphene (*31–34*). The only back scattering channel for these states is scattering from K valley to K' valley which is known as intervalley scattering. Since intervalley scattering is strongly suppressed at low temperatures, these states have a significantly longer mean free path, as confirmed by transport experiments (*26*, *32*).

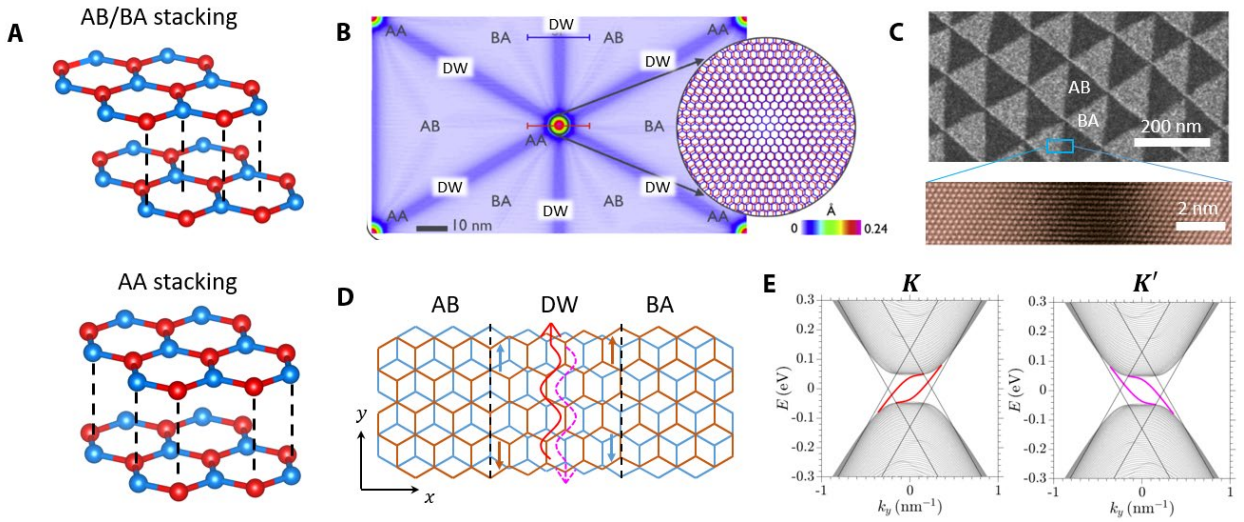

Figure 1.3 | Twisted bilayer graphene at small twist angles. (A) Schematic illustration of the AB and BA stackings. (B) Local out-of-plane displacement of the graphene layers obtained from large scale elastic simulations. Figure from (*25*). (C) Top: Large area transmission electron microscopy (TEM) image of TBG with a twist angle $\theta = 0.1°$. Figure from (*26*). Bottom: A zoom-in view of the domain wall showing a width of ~6 nm. Figure from (*31*). (D) A schematic showing the change in the atomic stacking at the domain wall. The topologically protected states localized to the domain wall are represented by red and pink arrows. (E). The dispersion of the topologically protected states. The left and right panels correspond to K and K' valleys.

1.2 Scattering SNOM and plasmon polaritons

1.2.1 Scattering SNOM

Scattering scanning near-field microscopy (scattering SNOM) or nano-infrared imaging is a deeply sub-diffractional scanning optical microscopy technique based on the atomic force microscope (AFM). A schematic is shown in Fig 1.4(A). Incident light (E_{inc}) polarizes the apex of the tip and induces a dipole of magnitude p_z. This tip dipole interacts with the sample to produce

an image dipole inside the sample. Because of the near-field interaction between the tip and image dipoles, some of the incident light is scattered into the far field (E_{scat}) which is then detected with a conventional detector (*2*, *3*). The tip is typically metallic which leads to an enhanced electric field at the apex due to antenna or lightning rod effects (*35*). The spatial resolution of scattering SNOM is only limited by the radius of curvature of the metallic tip and can be as small as 5 nm (*36*).

A major experimental challenge in scattering SNOM is the suppression of background signals that arise from light scattered off other parts of the tip and the sample. Several techniques are used in combination to isolate the near-field signal that arises from the apex of the tip. The most important technique is operating the AFM in tapping mode and demodulating the signal from the optical detector at a harmonic of the tip tapping frequency. Because the near-field interaction between the tip and image dipole decays exponentially with the tip-sample distance and the background stays relatively constant, the higher harmonics overwhelmingly contain the near-field signal of interest. Demodulation at the second to the fifth harmonic are used in typical experiments.

The scattered field E_{scat} is proportional to the dipole moment of the tip p_z and is directly related to the dielectric constant ϵ of the sample being studied. However, careful modeling is necessary to extract ϵ from the measured E_{scat} since E_{scat} is also strongly affected by the geometry of the tip (*35*).

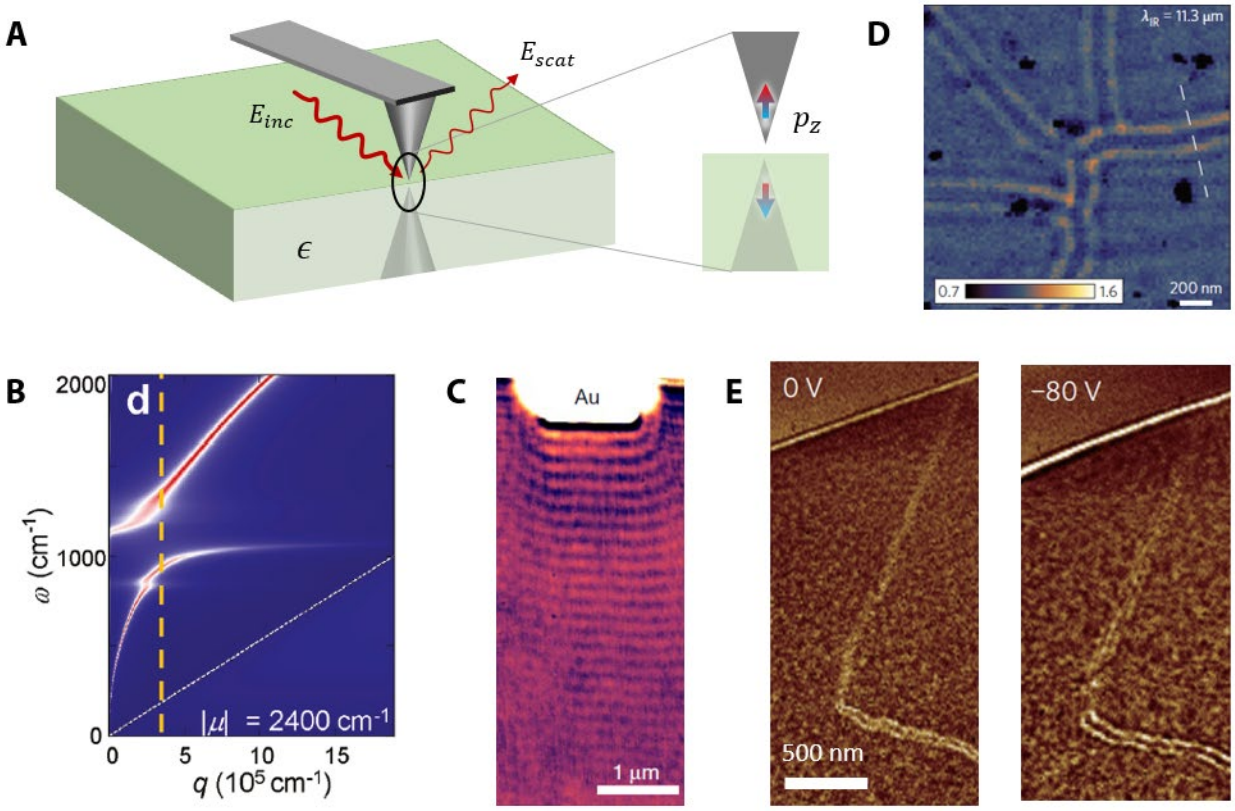

Figure 1.4 | Scattering SNOM and plasmons in graphene. (A) Schematic of scattering SNOM. E_{inc} and E_{scat} are the incident and scattered fields, ϵ is the substrate dielectric constant and p_z is the z component of the dipole moment of the tip. (B) Dispersion relation for SPPs in graphene with chemical potential $\mu = 2400\ \mathrm{cm}^{-1}$ which corresponds to a carrier density $n = 6.5 \cdot 10^{12}\ \mathrm{cm}^{-2}$. The vertical dashed line represents the momentum that the tip most strongly couples to. Figure from (*37*). (C) SNOM image of propagating SPPs launched by a gold antenna. Figure from (*38*). (D) SNOM image showing plasmons reflected by atomic scale grain boundaries in monolayer graphene. Figure from (*39*). (E) SNOM image showing SPPs reflected by AB-BA domain walls in bilayer graphene. Figure from (*33*).

1.2.2 Plasmon polaritons in graphene

The solutions to Maxwell's equations at the interface between materials with dielectric constant of opposite signs include a mode confined to the interface. The electric field of this mode decays exponentially away from the interface on both sides. The origin of the negative dielectric constant can be due to any resonance in the material. This hybrid light-matter mode is known as a surface polariton. The polariton wavelength can be orders of magnitude smaller the wavelength of light in vacuum, making polaritons promising for various nano-photonics applications (*40*).

The most commonly investigated form of surface polaritons are the surface plasmon polaritons (SPPs) where the negative dielectric constant arises from the metallic nature of the material. However, phonon polaritons and exciton polaritons arising from strong phonon and exciton resonances respectively, have also been investigated experimentally (*41*, *42*). Several other forms of polaritons have been predicted theoretically (*43*, *44*).

Graphene, being an excellent electrical conductor, was predicted to sustain SPPs at infrared frequencies (*45*). This prediction was verified by scattering SNOM experiments which demonstrated a confinement factor of >50 and SPP lifetime of about 0.1 ps, both of which were the highest known for infrared plasmonics at that time. Experiments on graphene encapsulated with hBN (*46*, *47*) and at low temperatures (*38*) have shown that the SPP lifetime in graphene can reach 1.6 ps and clarified the scattering mechanisms responsible for SPP dissipation in graphene.

Propagating SPPs appear directly in SNOM images as fringes. They can be launched by gold antennas which directly couple to the incident infrared light, as shown in Fig 1.4(C). SPPs can also launched by the metallic tip which can then detect the same SPPs if they are reflected by physical boundaries such as the edge of a graphene sheet (*48*, *49*). Purely electronic, atomic scale boundaries are also capable of reflecting SPPs, as shown in Figs 1.4(D) and 1.4(E). In Fig 1.4(D),

the defects are grain boundaries in monolayer graphene grown by chemical vapor deposition (CVD) (*39*) and in Fig 1.4(E), the defects are domain walls between AB-stacked and BA-stacked graphene discussed in Section 1.1.2 (*33*, *34*). Despite the atomic scale of the defects, the optical conductivity change at the defect is strong enough to cause significant reflection of SPPs which can be detected with SNOM.

AB-BA domain walls are predicted to host more exotic SPPs. Theoretical calculations predict that the domain walls host one-dimensional SPPs propagating along the domain walls. Because of the reduced scattering of the topological states along the domain walls, the lifetime of the 1D SPPs is expected to approach 100 ps (*50*, *51*). Such 1D plasmons have not yet been observed in experiment.

1.3 Photocurrent and nano-photocurrent in graphene

1.3.1 Photothermoelectric effect in graphene

In most materials, the predominant dissipation source for excited electrons is electron-phonon (e-ph) coupling where the hot carriers emit phonons and decay to a lower energy state. However, this coupling is weak in graphene compared to typical three dimensional metals because of the very small Fermi surface of graphene (*52*, *53*). Such weak e-ph coupling leads to long lived hot carriers in graphene (*54*). Therefore, when such hot carriers in graphene encounter spatial variations in Seebeck coefficient, they generate thermoelectric voltages. Laser light incident on graphene generates hot carriers and the resulting thermoelectric currents are the dominant source of photocurrent in graphene. This mechanism has been termed the photothermoelectric effect (PTE) and is illustrated schematically in Fig 1.5(A).

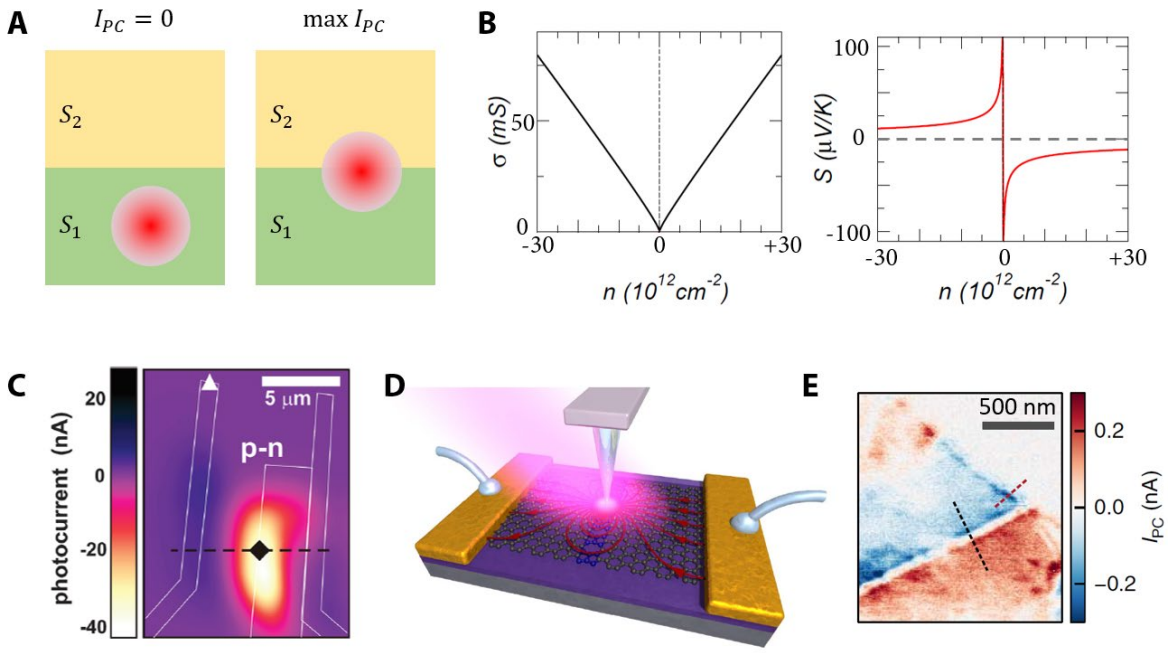

Figure 1.5 | Nano-photocurrent in graphene. (A) Schematic of photocurrent generation in graphene. The green and orange rectangles represent regions with different Seebeck coefficient and the red spot represents the incident laser beam. (B) Carrier density dependence of conductivity and Seebeck coefficient for monolayer graphene. (C) Scanning photocurrent image of a graphene pn junction obtained by scanning a diffraction limited laser spot. The measured photocurrent is maximal at the junction. Figure from (*55*). (D) Schematic of nano-photocurrent imaging. (E) Representative nano-photocurrent image showing a significantly improved spatial resolution in comparison to (C). Panels (D) and (E) from (*4*).

The Seebeck coefficient in graphene can be modified by physically changing the graphene layer (e.g. an interface between monolayer and bilayer graphene). However, the strongly gate tunable conductivity of graphene also leads to a gate dependent Seebeck coefficient (*56*, *57*), as shown in Figure 1.5(B). Therefore, a graphene junction with different carrier densities on either

side can generate photocurrent, as shown in Figure 1.5(C). This effect was used to conclusively show that the PTE mechanism dominates the photocurrent generation in graphene (*55*, *58*). Scanning photocurrent experiments also show complex spatial patterns. A theoretical formalism known as the Shockley-Ramo formalism (*59*) has been developed to predict the spatial photocurrent patterns. We discuss this formalism in more detail in Chapter 4.

1.3.2 Nano-photocurrent measurements on graphene

The early photocurrent experiments used a focused laser spot that was diffraction limited (*55*, *60*). Therefore, their spatial resolution was limited, as can be seen in Fig 1.5(C). Later, the same experimental setup used for scattering SNOM was used to perform photocurrent experiments which led to a significantly higher spatial resolution limited only by the properties of graphene (Figs 1.5(D) and 1.5(E)). This technique has since been called nano-photocurrent (*4*). Since photocurrent experiments on graphene are sensitive to the DC Seebeck coefficient, nano-photocurrent imaging can be thought of as a complementary technique to scattering SNOM.

1.4 Outline

In this thesis, we used scattering SNOM and nano-photocurrent imaging, to study twisted bilayer graphene (TBG) in two different twist angle regimes: $\theta < 0.5°$ (small) and $\theta > 0.5°$ (large). The boundary between the two regimes roughly corresponds to a moiré period equal to the spatial resolution of our nano-optics probes. Therefore, in the small twist angle regime, we resolve variations within the moiré unit cell while in the large twist angle regime, we measure the electronic properties of TBG averaged over the moiré unit cell.

Chapter 2 details our scattering SNOM study of small twist angle TBG. We imaged the atomic relaxation and the spatially inhomogeneous features within the moiré unit cell of TBG. Our experiments and modeling showed that the periodic moiré pattern acts as a photonic crystal for propagating SPPs. Chapter 2, in full, is a reprint of "Photonic crystals for nano-light in moiré graphene superlattices" by S. S. Sunku, G. X. Ni, B. Y. Jiang, H. Yoo, A. Sternbach, A. S. McLeod, T. Stauber, L. Xiong, T. Taniguchi, K. Watanabe, P. Kim, M. M. Fogler, D. N. Basov, *Science* **362**:1153 (2018). The dissertation author was the co-primary researcher and author of this material.

In Chapter 3, we studied TBG in the large angle regime. We developed a method to locally determined the twist angle of TBG with nano-photocurrent experiments and confirmed the measured twist angles with nano-infrared imaging. Chapter 3, in full, is a reprint of "Nano-photocurrent Mapping of Local Electronic Structure in Twisted Bilayer Graphene" by Sai S. Sunku, Alexander S. McLeod, Tobias Stauber, Hyobin Yoo, Dorri Halbertal, Guangxin Ni, Aaron Sternbach, Bor-Yuan Jiang, Takashi Taniguchi, Kenji Watanabe, Philip Kim, Michael M. Fogler, D. N. Basov, *Nano Letters* **5**:2958 (2020). The dissertation author was the co-primary researcher and author of this material.

In Chapter 4, we study small twist angle TBG with nano-photocurrent imaging. Our experiments provided insight into the nanoscale variations in Seebeck coefficient that occur at the domain walls in small angle TBG. Chapter 4, in full, is a reprint of "Hyperbolic enhancement of photocurrent patterns in minimally twisted bilayer graphene" by Sai S. Sunku, Dorri Halbertal, Tobias Stauber, Shaowen Chen, Alexander S. McLeod, Andrey Rikhter, Michael E. Berkowitz, Chiu Fan Bowen Lo, Derick E. Gonzalez-Acevedo, James C. Hone, Cory R. Dean, Michael M.

Fogler, D. N. Basov, to appear in *Nature Communications*. The dissertation author was the co-primary researcher and author of this material.

A dual gated structure is essential for studying the rich physics that appears in gapped bilayer graphene including the 1D plasmons discussed in Section 1.2.2. In Chapter 5, we investigate monolayer graphene and MoS_2 as potential candidates for a nano-optics compatible top gate and identify their strengths and weaknesses. Chapter 5, in full, is a reprint of "Dual-gated graphene devices for near-field nano-imaging" by Sai S. Sunku, Dorri Halbertal, Rebecca Engelke, Hyobin Yoo, Nathan R. Finney, Nicola Curreli, Guangxin Ni, Cheng Tan, Alexander S. McLeod, Chiu Fan Bowen Lo, Cory R. Dean, James C. Hone, Philip Kim, D. N. Basov, to appear in *Nano Letters*. The dissertation author was the co-primary researcher and author of this material.

Chapter 2: Quantum Photonic Crystal

2.1 Introduction

Graphene is an atomically thin plasmonic medium that supports highly confined plasmon polaritons, or nano-light, with very low loss. Electronic properties of graphene can be drastically altered when it is laid upon another graphene layer, resulting in a moiré superlattice. The relative twist angle between the two layers is a key tuning parameter of the interlayer coupling in thus obtained twisted bilayer graphene (TBG). We studied propagation of plasmon polaritons in TBG by infrared nano-imaging. We discovered that the atomic reconstruction occurring at small twist angles transforms the TBG into a natural plasmon photonic crystal for propagating nano-light. This discovery points to a pathway towards controlling nano-light by exploiting quantum properties of graphene and other atomically layered van der Waals materials eliminating need for arduous top-down nanofabrication.

When light of wavelength λ_0 travels through media with periodic variations of the refractive index, one witnesses an assortment of optical phenomena categorized under the notion of a photonic crystal (*61*). The additional periodicity imposed on light can trigger the formation of a full photonic band gap (*62*) and may also produce chiral one-dimensional (1D) edge states (*63*) or exotic photonic dispersions emulating that of Dirac and Weyl quasiparticles (*64*). In principle, the photonic crystal concept is also applicable for controlling the propagation of "nano-light": coupled oscillations of photons and electrons confined to the surface of conducting media and referred to as surface plasmon polaritons (SPPs) (*48*, *49*, *65*). The wavelength of SPPs, λ_{SPP}, is reduced compared to λ_0 by up to three orders of magnitude (*66*). However, this virtuous

confinement poses challenges for the implementation of the nano-light photonic crystals by standard top-down techniques (*67*, *68*).

Graphene has emerged as an extremely capable plasmonic medium in view of ultra-strong confinement, quantified by $\lambda_0/\lambda_{SPP} \geq 1000$ (*66*) attained in the regime of weak loss (*38*, *47*). Plasmonic properties of graphene can be readily controlled by carrier density (*48*, *49*), dielectric environment (*47*, *69*) and ultrafast optical pulses (*46*). Here, we have explored and exploited yet another control route based on the twist angle θ between neighboring graphene layers (*26*, *69–73*). In TBG, the local stacking order changes smoothly across the narrow solitons separating AB- from BA- domains (*31*), as revealed (Fig. 2.1(B)) by dark field (DF) transmission electron microscopy (TEM). Previous nano-IR experiments on isolated solitons in Bernal-stacked bilayer graphene (BLG) have shown that SPPs in BLG are scattered by the solitons (*33*, *34*) analogous to the scattering of SPPs by grain boundaries in monolayer graphene (*39*). Therefore, a regular pattern of such solitons (Fig. 2.1(B)) is expected to act as a periodic array of scatterers thus fulfilling the key pre-condition for nano-light photonic crystal. Unlike all previous implementations of photonic crystals (*74*, *75*), our approach exploits local changes in the electronic band structure of the plasmonic medium, a quantum effect, to control optical phenomena. We explored this novel and fundamentally quantum approach for manipulating plasmons via direct nano-imaging experiments, modeling and theory.

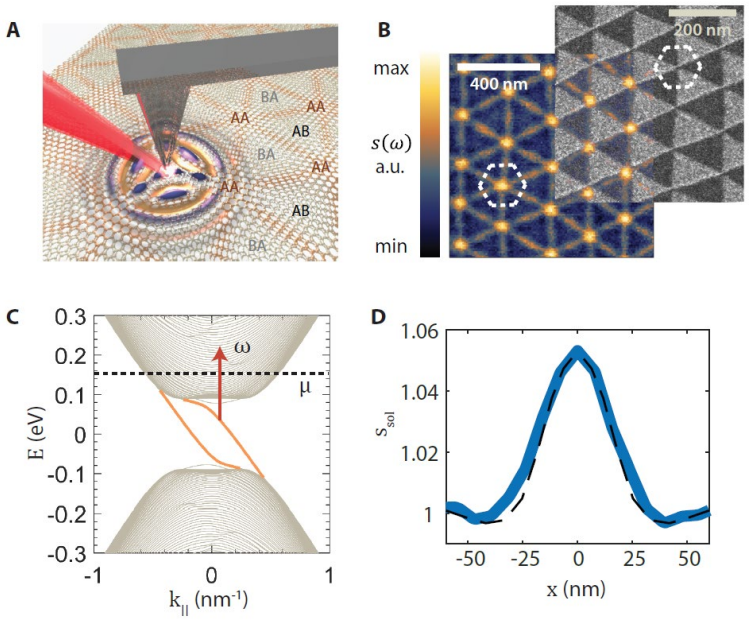

Figure 2.1 | Nano-light photonic crystal formed by a network of solitons in twisted bilayer graphene. (A) Schematic of the infrared nano-imaging experimental setup. AB, BA, AA label periodically occurring stacking types of graphene layers. (B) Left: Visualizing the nano-light photonic crystal formed by the soliton lattice. The contrast is due to enhanced local optical conductivity at solitons. Right: Dark-field transmission electron microscopy image of a twisted bilayer graphene sample showing contrast between AB and BA triangular domains. The dashed white hexagons represent unit cells of the crystals. (C) Electronic band structure of a single infinitely long soliton (only the K valley is shown). Chiral 1D states are depicted in orange. Optical transitions such as those indicated by the red arrow are responsible for the enhanced local conductivity at the location of solitons. (D) Experimental (solid) and calculated (dashed) near-field signal $s_{sol}(x)$ across a single soliton line. Calculation parameters are frequency $\omega = 1180\text{cm}^{-1}$, Fermi energy $\mu = 0.3\text{eV}$, interlayer bias $V_i = 0.2\text{V}$ and dimensionless damping $\eta = 0.2$ (see text).

2.2 Nano-infrared imaging of single domain walls

Infrared nano-imaging (Fig. 2.1(A)) is central to unveiling the physics of a quantum photonic crystal for plasmons. In our experiments, infrared light at frequency $\omega = 1/\lambda_0$ is focused on the apex of a metallic tip. The amplitude of the backscattered signal $s(\omega)$ and its phase $\phi(\omega)$ are recorded using an interferometric detection (Section 2.6). When ω is close to the optical phonon of the SiO_2 substrate, as in Fig. 2.1(B), IR nano-imaging effectively reveals local variations of the optical conductivity ((*37*), Section 2.6). In Figure 2.1(B), we observed a six-fold pattern of bright line-like features with even stronger contrast at the intersections. A dark field TEM image of a similar TBG sample also reveals the same six-fold symmetry with features matching the nano-IR data. The periods of both patterns are consistent with the moiré length scales anticipated for a nominal twist angle of ~ 0.1°. An accurate estimate of the periodicity a for our device can be directly read off the near-field image: given the observed $a \simeq 230$ nm we obtain a twist angle of $\theta \simeq 0.06^{\circ}$ (Section 2.6). We therefore conclude that the near-field image constitutes a direct visualization of the solitonic lattice.

The nano-IR contrast at the solitons is the result of topological changes to the electronic structure. When inversion symmetry is broken by an application of a perpendicular displacement field using the back gate, the Bernal stacked AB and BA domains reveal a bandgap (*10*) and the valley Chern number at K and K' valleys is ±1 (*76*). As the stacking order evolves across the soliton, the Chern numbers also change sign. The difference in Chern number leads to topologically protected one-dimensional states along the soliton (*27*, *28*). The key implication of this band structure effect (*34*) is that optical transitions from the topologically protected states to empty states above the Fermi level prompt an enhanced conductivity at the soliton (Fig. 2.1(C)).

Consistent with this view, resistivity experiments signal ballistic electron transport along the solitonic channels (*26*, *32*).

Our qualitative understanding of the near-field contrast is corroborated by modeling. The near-field amplitude and phase profiles, $s_{sol}(x)$ and $\phi_{sol}(x)$, x is the coordinate normal to the soliton, depend on the Fermi energy μ, the interlayer bias V_i and the plasmonic damping rate η (Section 2.6.4). These latter profiles obtained for isolated solitons (*33*, *34*) were fully elucidated by combining electronic structure calculations, scattering theory, and numerical modeling of the tip-sample coupling (*34*, *77*). Figure 2.1(D) shows the calculated $s_{sol}(x)$ using parameters that most closely correspond to the experiment in Fig 2.1(B).

2.3 Nano-infrared imaging of the quantum photonic crystal

We now discuss the impact of periodically varying conductivity in TBG on propagating plasmon polaritons. In our experiments, SPPs of wavelength λ_p of the order of the soliton periodicity a are introduced by the metallic tip (Figure 2.1(A) and Refs. (*46*, *47*)). In order to launch propagating polaritons, we choose ω to be away from phonon resonances. In this regime, the scattering of SPPs by the solitons produces fringes in both $s(\omega)$ (*48*, *49*) and $\phi(\omega)$ (*78*) corresponding to standing waves. Two-dimensional (2D) maps of both observables are displayed in Figure 2.2. We obtained these images in different regimes of λ_p/a by tuning the gate voltage V_G and/or λ_0. All images are dominated by maxima and minima in the nano-IR contrast, indicating the presence of constructive and destructive interference of SPPs triggered by the solitonic lattice.

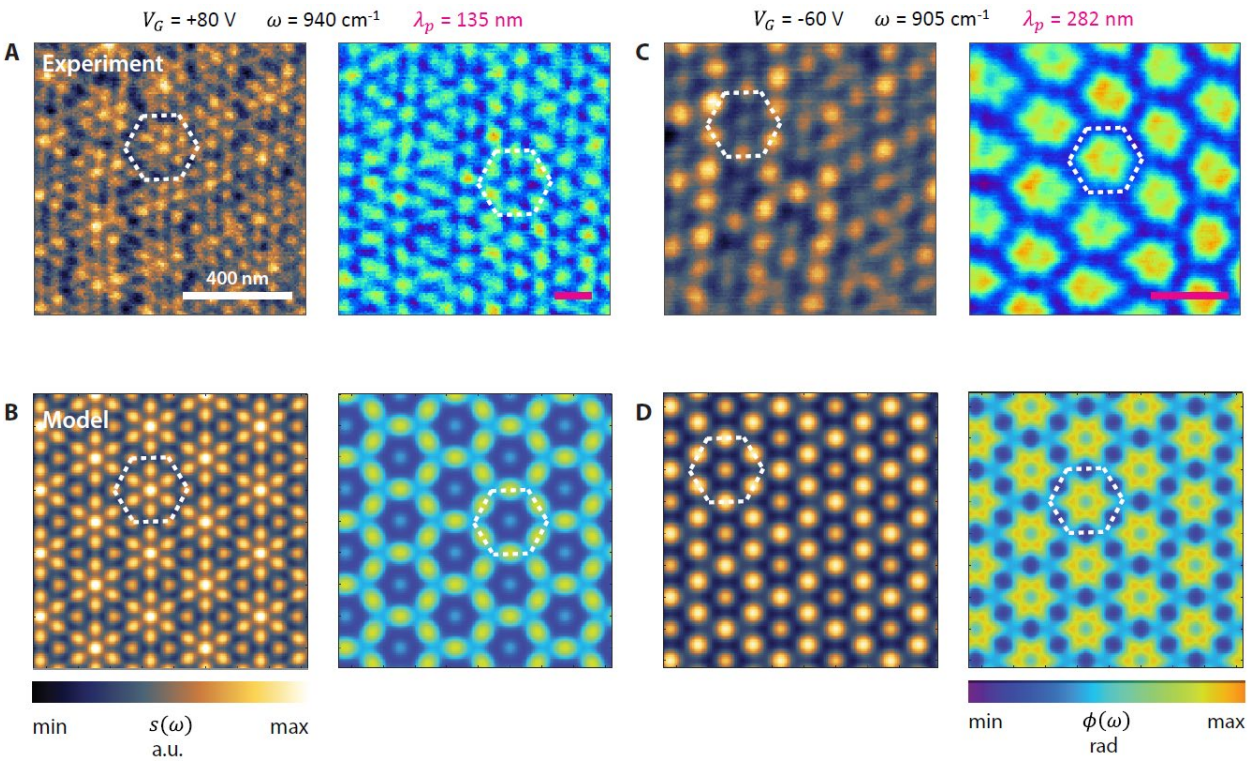

Figure 2.2 | Plasmon interference patterns and superposition model analysis. (A, C) Nano-IR images obtained for λ_p = 135 nm and 282 nm. (B, D) Near-field amplitude and phase images calculated using the superposition model (introduced in the text). The model parameters used to obtain the images are: (B) $\mu = 0.23$eV, $V_i = 0.3$V, $\eta = 0.2$ (D) $\mu = 0.35$eV, $V_i = 0.1$V, $\eta = 0.2$. The dashed-line hexagons represent the boundaries of a single unit cell and the magenta bars represent the SPP wavelengths.

The Fourier analysis of the $s(\omega)$ images shown in Figures 2.3 (A, B) supports our conjecture of a photonic crystal. We denote the magnitude of the 2D spatial Fourier transform of the $s(\omega)$ image as $\tilde{s}(q)$. Figure 2.3(A) shows $\tilde{s}(q)$ extracted from the spatially varying conductivity image displayed in Figure 1(B) and is seen to have six-fold rotational symmetry. This symmetry is preserved in the $\tilde{s}(q)$ images obtained by transforming data in Figure 2.2 in the regime where our

structures support propagating SPPs. Figure 2.3(B) shows the line profiles taken along one of the high-symmetry directions for all $\tilde{s}(q)$ images. The peaks in all the images are anchored at the same momenta in Fourier space, indicating that the periodicity of the polaritonic nano-IR patterns matches that of the moiré lattice. Our nano IR imaging and its Fourier transformed patterns thus give further evidence of plasmonic interference in the soliton crystal formed in TBG.

2.4 Modeling and tunability of the photonic crystal

For a quantitative analysis of the SPP interference, we introduce a superposition model. In this simplified model, we neglect multiple scattering of plasmons by these domain walls and disregard any interaction of the domain walls at their intersections. In other words, we treat the domain walls as interpenetrating and decoupled objects. We compute the near-field signal produced by a single (infinitely long) soliton as accurately as realistically possible via microscopic calculations of the electron band structure, optical conductivity, and tip-sample coupling (*34*, *77*). The superposition model takes as a basic input the profiles of the near-field amplitude $s_{sol}(x)$ and phase $\phi_{sol}(x)$ (Fig 2.1(D) and Section 2.6.4) for a single soliton. It is easy to see that the 2D soliton lattice consists of three one-dimensional periodic arrays rotated in-plane by 120° with respect to one another. Consider one such array where solitons located at equidistant positions x_k. Within the superposition model, this array produces the complex near-field signal equal to the sum $\sum_k s_{sol}(x - x_k)e^{i\phi_{sol}(x-x_k)}$. Since $s_{sol}(x)$ is rapidly decreasing away from the solitons, it is sufficient to keep only a few nearest-neighbor terms in this summation. The signal from the remaining one-dimensional arrays is calculated in a similar way. The superposition of all these signals yields the images displayed in Figures 2.2(B) and 2.2(D). This procedure yields a close correspondence between the experimental data and the model in both amplitude and phase.

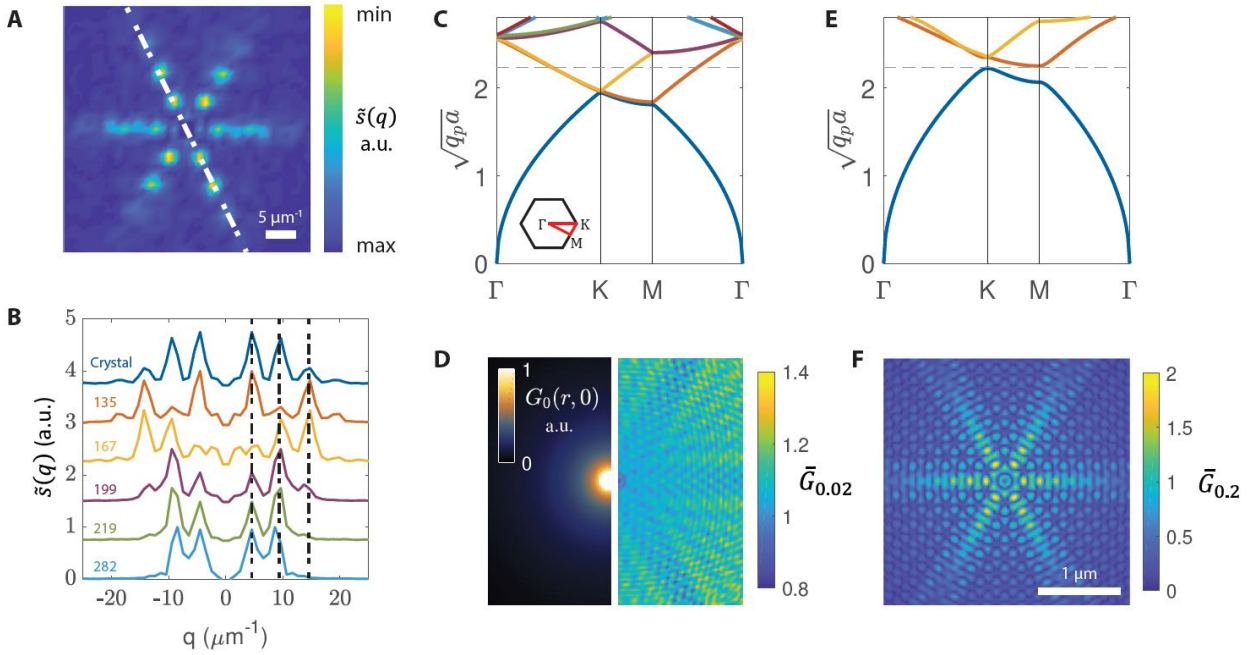

Figure 2.3 | Properties of the graphene-based quantum photonic crystal. (A) Fourier transform $\tilde{s}(q)$ of the photonic crystal image with no propagating SPPs (as in Fig. 2.1(B)). (B) Line profiles of $\tilde{s}(q)$ taken along the white dashed line in (A) for the crystal devoid of propagating SPPs and for the same crystal with propagating SPPs of various wavelengths λ_p. The curves are vertically offset for clarity. (C) Plasmonic band structure for dimensionless scattering strength $t = 0.02$ defined the text; $t = 0.02$ most closely corresponds to the experimentally studied crystal. (E) Plasmonic band structure for $t = 0.2$ showing the formation of a full plasmonic gap. (D) Near-field signal calculated for a point source at an AA vertex. The left half shows G_0, the near-field signal computed for the empty lattice ($t = 0$). The right half depicts the ratio $\bar{G}_{0.02} = G_{0.02}/G_0$, where $G_{0.02}$ is the signal for $t = 0.02$. (F) Near-field signal ratio $\bar{G}_{0.2} = G_{0.2}/G_0$ where $G_{0.2}$ is the signal for $t = 0.2$. The frequency in both (D) and (F) corresponds to the plasmon momentum, q_p that satisfies $\sqrt{q_p a} = 2.23$, shown by the dashed lines in (C, E). When this frequency is outside (inside) the

band gap, the plasmonic patterns are delocalized (localized) and weakly (strongly) anisotropic, *cf.* panel D (panel F). See Section 2.6.7 for details of these calculations.

A key feature of moiré photonic crystal is its tunability. The periodicity of the crystal, a, can be continuously varied by changing the twist angle (*26*) and the SPP-soliton scattering strength can be modulated by the carrier density and the interlayer bias (*34*). In order to illustrate the tunability, we introduce the dimensionless scattering strength

$$t = \frac{1}{a}\int_{-\infty}^{\infty} dx \, \frac{\sigma_s(x) - \sigma_0}{\sigma_0}, \tag{2.1}$$

that governs the interaction between the SPPs and the solitons. Here $\sigma_s(x)$ is the local infrared conductivity along the direction perpendicular to the soliton and σ_0 is the asymptotic value of this conductivity far away from the soliton (*34*, *77*). Note that parameter t governs the long-range behavior of the SPP waves scattered by a soliton. The details of the short-range behavior (an example of which is shown in Figs. 2.1(D) and 2.2(B), 2.2(D)) depend, in general, on the exact profile $\sigma_s(x)$. However, the plasmon band structure is predominantly sensitive to the long-range processes, so a single parameter t suffices. We now evaluate the plasmonic band structure in momentum space for selected t values using a reciprocal-space method ((*79*), Section 2.6). Figure 2.3(C) shows the band structure for parameters that correspond most closely to our current experiment (a = 230 nm, t = 0.02); we notice that the plasmonic gap is insignificant. However, a larger scattering strength that is likely to be attained in future experiments does yield a full band gap arresting plasmonic propagation (Figure 2.3(E)). We also remark that a point-like source in plain graphene launches an isotropic cylindrical wave (Figure 2.3(D), left half) whose amplitude decays asymptotically as the square root of the distance. While the decay is expected to be the same

for a plasmonic crystal at frequencies within the plasmonic bands, the rotational symmetry of the waves must reduce to comply with the symmetry of the crystal. The reduction to six-fold symmetry for our crystal can be revealed by dividing the signals with and without the crystal pointwise (Figure 2.3(D), right half). In contrast, excitations at frequencies inside the bandgap must be localized, showing exponential decay of the amplitude away from the source. We also predict that the localized states are strongly anisotropic, yielding signal distributions resembling snowflakes (Figure 2.3(F)) or three-pointed stars (Figure 2.1(A) and (Section 2.6)). To generate patterns of this kind, one can add point-like plasmonic emitters, e.g., small gold disks (*80*) to the system.

2.5 Conclusion

The nano-light photonic crystal devised, implemented and investigated in this work is unique in several ways. First, the local variation of the response is rooted in topological electronic phenomena occurring at the solitons at variance with commonplace classical photonic crystals based on locally perforated media. Second, its key parameters (periodicity and band structure) can be continuously tuned electrostatically and/or nanomechanically (*17*) and do not require extremely challenging top-down fabrication. In closing, we remark that it would be interesting to explore the regime close to the charge neutrality, where the solitons are predicted to host 1D plasmon modes (*34*, *50*). In this regime our structure would act as a 2D network or possibly, a controllable circuit capable of routing such 1D plasmons.

2.6 Supplementary Material

2.6.1 Materials and Methods

2.6.1.1 Device fabrication

Twisted bilayer graphene was produced by the 'tear-and-stack' dry transfer technique as detailed in Ref (*26*). First a layer of boron nitride (BN) is picked up using an adhesive polymer poly(bisphenol A carbonate) (PC) coated on a stamp made of transparent elastomer polydimethylsiloxane (PDMS). A large flake of monolayer graphene is identified and the BN flake is used to tear the graphene flake into two and pick up one half. The substrate is then rotated by a controlled angle and the second half of the graphene flake is picked up. The entire stack is then placed on a clean silicon dioxide/silicon substrate. The thickness of the BN used for the device in this work is 6nm.

2.6.1.2 Infrared nano-imaging

Infrared nano-imaging was performed with a commercial scattering-type scanning near-field optical microscope (Neaspec GmbH) based on a tapping mode atomic force microscope. Our light source was a quantum cascade laser obtained from DRS Daylight Solutions, tunable from 900 cm^{-1} to 1200 cm^{-1}. The light from the laser was focused onto a metallic tip oscillating at a tapping frequency of around 250 kHz with a tapping amplitude of around 60 nm. The scattered light was detected using a liquid nitrogen cooled HgCdTe (MCT) detector. To suppress far-field background signals, the detected signal was demodulated at a harmonic n of the tapping frequency. In this work, we used $n = 4$.

2.6.2 Visualizing the soliton lattice

As shown in Figure 2.1(B), we were able to visualize the soliton lattice by measuring $s(\omega)$ at $\omega = 1180$ cm^{-1}. In Figure 2.4(A), we show a color plot of the imaginary part of the reflection coefficient Im(r_p) for our heterostructure when the graphene stacking configuration is Bernal stacking. By comparing the polaritonic dispersion at the three frequencies used in this work (905 cm^{-1}, 940 cm^{-1} and 1180 cm^{-1}), we see that at the highest frequency, the group velocity of the polariton is highly suppressed (Section 2.6.2). Furthermore, the damping of the polariton is also highest at 1180 cm^{-1}. Figure 2.4(B) shows line profiles at 905 cm^{-1} and 1180 cm^{-1}. The broad maximum at 1180 cm^{-1} indicates that the polariton damping is high at this frequency. The combination of these two effects leads to a very short propagation length for the polariton at 1180 cm^{-1} and results in the soliton appearing as a single bright line in our nano-infrared images.

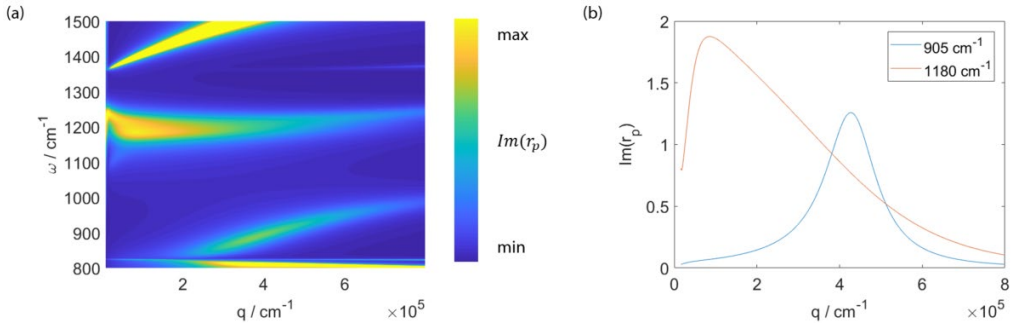

Figure 2.4 | Polariton dispersion. (a) Color plot of the imaginary part of the Fresnel reflection coefficient for p-polarized light $Im(r_p)$ for the heterostructure studied in this work when the graphene stacking is Bernal stacking. (b) Plot of Im(r_p) as a function of q at 905 cm^{-1} and 1180 cm^{-1}.

The magnitude of the near-field contrast is known to be a complicated functional of the optical conductivity of the sample and the tip-sample coupling. The latter may sensitively depend on the exact geometry of the tip and other experimental parameters (*35*, *81*). While a higher local conductivity typically leads to a higher near-field signal, in general, there is no simple quantitative relation between the two. Extensive numerical modeling (similar to (*34*)) is necessary for a quantitative comparison between the experimental data and the expected $\sigma_s(x) - \sigma_0$.

Note also that "brightest" regions of the obtained images are centered at intersections of solitons (the "vertices"). Within our "superposition" approach, this property follows simply from the fact that the scattering signal at a vertex has strong contributions from all three intersecting walls. We certainly do not think that this approximation is physical, i.e., we do not think that domain walls at a vertex run straight through one another without any interaction. Nevertheless, our simulations based on the superposition approximation are in a qualitative agreement with the data, see Fig. 2.9. Additional dedicated experiments and theoretical calculations would be necessary to understand the structure of the vertex and its near-field response. This is a challenging problem that goes beyond the scope of the present work. Note, for example, that the plasmon wavelength is much longer than the characteristic physical dimension of the vertex. It is therefore quite difficult to resolve the microscopic structure of a vertex with the plasmon nano-imaging.

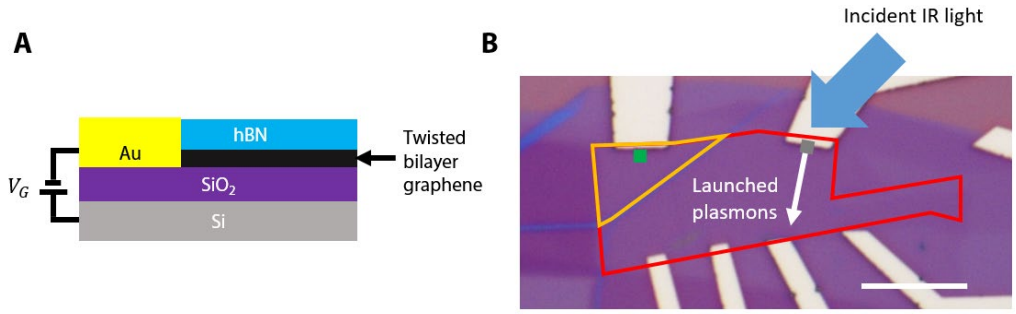

Figure 2.5 | Location and direction of gold electrode launched plasmons. (a) Schematic cross section of the device studied in this work. (b) Optical microscope image of the device. The red polygon encloses the twisted bilayer region and the orange polygon encloses the photonic crystal region. The green square indicates the region investigated in Figure 2.2 and the first two columns of Figure 2.3. The grey square indicates the region measured in the fourth column of Figure 2.5. Scale bar 10 μm.

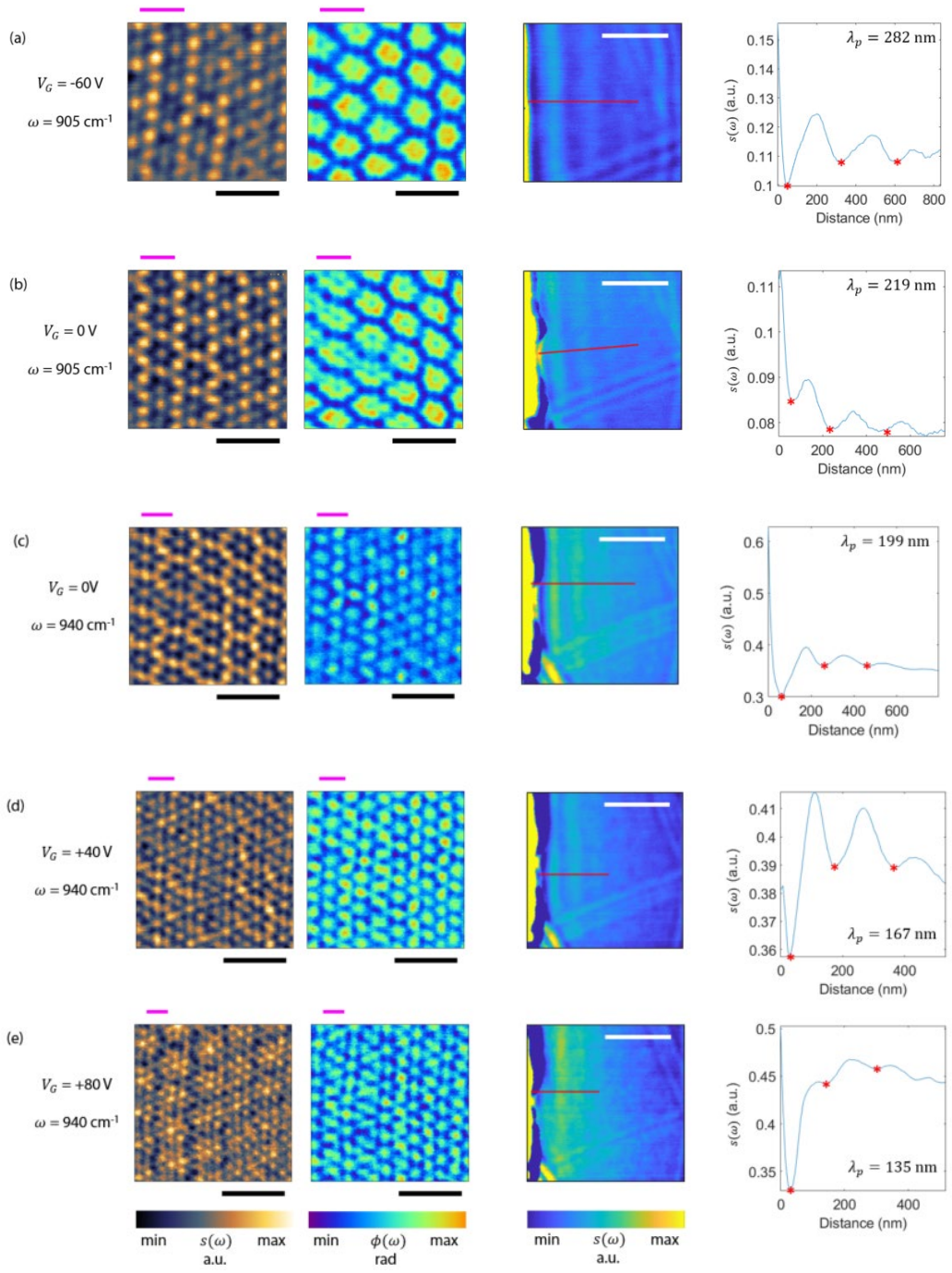

Figure 2.6 | Determination of the plasmon wavelength. The leftmost two columns show $s(\omega)$ and $\phi(\omega)$ images for various values of λ_p. Images from panels (a) and (e) are shown in Figure 2.2. Black scale bar 400 nm. The magenta bars represent the SPP wavelength. The measured region is shown as a green square in Figure 2.5(B). The third column shows images of the electrode launched

plasmons under the same conditions. The bright yellow feature visible on the left of the images in this column is the gold electrode. White scale bar 400 nm. The measured region is shown as a gray square in Figure 2.5(B). The rightmost column shows the line-profile taken along the red line in the third column and averaged over a width of 80 nm. The red stars mark the first three minima. λ_p is extracted by taking the average of the spacing between these minima.

2.6.3 Estimating the twist angle

For twisted bilayer graphene, the periodicity of the Moiré pattern λ_M and the twist angle θ are related by $\lambda_M = a_0/[2\sin(\theta/2)]$ where a_0 = 0.246 nm is the lattice constant of monolayer graphene. From Figure 2.1(B), we extract the periodicity to be approximately 230 nm and this corresponds to the twist angle of 0.06°. Since the Moiré periodicity is significantly longer than the inter-atomic spacing, the lattice is incommensurate despite the atomic relaxation (*25*).

2.6.4 Nano-IR images at other values of λ_p

In this section, we show the nano-IR images taken at values of λ_p other than those shown in Figure 2.2. First we describe our method for extracting λ_p. We investigated a different region of the sample where we were able to images plasmons launched by a gold electrode (Figure 2.5). The fringes from the electrode-launched plasmons are known to have the same periodicity as the plasmon wavelength (*38*, *82*). The raw data is shown in Figure 2.6. At the bottom of each image, a three-peaked structure is present corresponding to a single shear soliton (*33*, *34*). The presence of this soliton to confirms that the region above the soliton is Bernal-stacked bilayer graphene with zero twist angle.

We now comment on plasmonic lifetimes and quality factors of our devices. The devices studied in this work are proof-of-concept devices. Their plasmonic lifetimes are below the record values reported in the literature (*38*, *47*) but nevertheless sufficiently long for us to demonstrate rich interference patterns. To compare the lifetime in our device with values in the literature, we define the quality factor for plasmons: $Q = \mathrm{Re}(q_p)/\mathrm{Im}(q_p)$ where q_p is the complex plasmon momentum. Based on the extracted line profiles in Figure 2.5, we estimate that $Q \sim 10$ in our case. This value is typical for devices where the graphene is directly on SiO_2 (*48*, *49*). We note that previous works on high-quality, fully hBN-encapsulated monolayer graphene (MLG) heterostructures has shown that the plasmonic lifetime is limited by the dielectric properties of the hBN and not by the graphene itself (*38*, *47*). Therefore, we expect that lifetimes similar to the record-high values reported for MLG heterostructures, $Q \sim 125$ (*38*), can also be achieved in twisted bilayer graphene heterostructures.

2.6.5 Superposition model

The Bernal-stacked bilayer graphene regions in our sample possess an electronic gap. Inducing a bandgap in bilayer graphene requires the breaking of inversion symmetry and a single gate is sufficient for this purpose (*83*–*85*). However, the limitation of a single gate is that it is not possible to independently tune the bandgap and the Fermi energy.

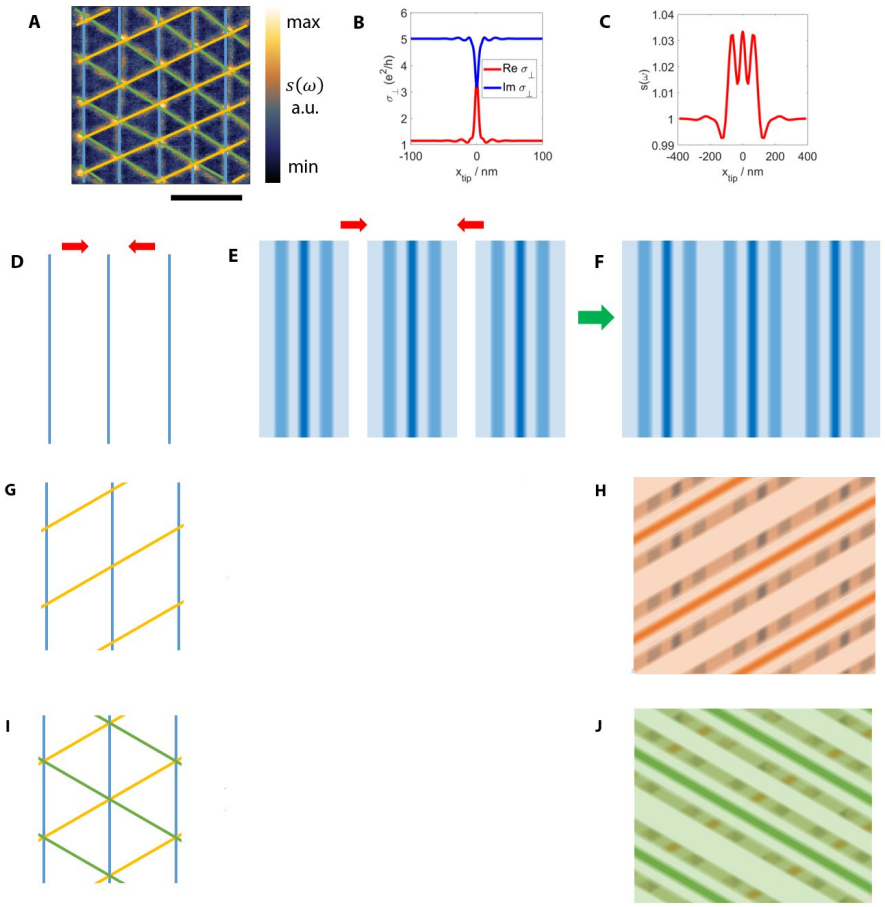

Figure 2.7 | Schematic illustration of the superposition model. (A) The soliton lattice can be decomposed into three sublattices each of which consist of solitons parallel to each other. Each sublattice is highlighted by a different set of colored lines. (B) The real and imaginary parts of the conductivity across the soliton. (C) Near-field profile due to plasmons scattering off a single isolated soliton calculated for $\mu = 0.23\text{eV}$, $V_i = 0.3\text{V}$, $\eta = 0.2$ (corresponding to Figure 2.2(B)). (D) Schematic illustration of the solitons in the sublattice highlighted in (A). The red arrows illustrate the reduction in spacing between the solitons. (E) Schematic demonstrating the superposition of the near-field profiles as the solitons are brought closer together. (F) Schematic of the final result after superposition. (G), (H) and (I), (J) Similar schematics as (D) and (F) after the addition of the second and third sublattice respectively.

The model images in Figure 2.2 were created by superposing the simulated near-field response $s_{sol}\, e^{i\phi_{sol}}$ of a single soliton. Functions $s_{sol}(x)$ and $\phi_{sol}(x)$ were found by calculating the conductivity profile $\sigma_s(x)$ due to the soliton from the Kubo formula and using it as the input to our custom electromagnetic solver. This procedure is described in detail in our previous work (*34*) and references therein. An example of the profile $s_{sol}(x)$ we used is shown in Figure 2.6(C). The three adjustable parameters in this model, chemical potential μ, the interlayer bias V_i and the plasmonic damping rate η, were tuned until a good match with the experimental images was obtained. The scattering strength t was then computed from $\sigma_s(x)$ via Eq. (2.1). The conductivity $\sigma_s(x)$ is in fact anisotropic and complex. Thus, instead of a single parameter t, one should in principle discuss two parameters, t_x and t_y. For Figure 2.2(B), where $\mu = 0.23$ eV and $V_i = 0.3$ V, these scattering parameters are $t_x = -0.032 - 0.027i$ and $t_y = 0.022 - 0.015i$, which produces the band structure shown in Figure 2.7(A). For Figure 2.2(D), where $\mu = 0.35$ eV and $V_i = 0.1$ V, the scattering parameters are $t_x = -0.011 - 0.011i$ and $t_y = 0.025 - 0.002i$, which produces the band structure shown in Figure 2.7(B). Since Figure 2.3 was meant to be a qualitative illustration, we presented the results for two simple isotropic examples, $t \equiv t_x = t_y = 0.02$ (panel C) and 0.2 (panel E).

For the structures we study, it is safe to assume that the Bloch minibands are so closely spaced in energy that they do not produce any observable effects. This is because the electron Fermi wavelength is very short compared to the period of the soliton crystal: a few nanometers compared to several hundred nanometers. In other words, for electrons, unlike plasmons, the periodic potential of the soliton crystal can be considered a slowly varying, adiabatic perturbation.

Therefore, the energy width of the Bloch minibands and minigaps is exponentially small. The good agreement between the experimental data and our "superposition model" further suggests that the latter model, which neglects the Bloch minibands, is nevertheless adequate in the regime of very small twist angle studied here.

The plasmon wavelength corresponding to the above Fermi energies are of the order of several nanometers. Non-local effects in the optical conductivity are only appreciable when the Fermi wavelength becomes comparable to the plasmon wavelength. Therefore, they can be neglected in our system. Such effects can become important when the plasmonic crystal is fabricated in proximity to a metallic gate (*86*).

In principle, plasmons can be launched when incident light scatters off any inhomogeneity present in the system, e.g., the solitonic lattice itself. We do not include this in our model of the near-field contrast because it must be a negligibly small effect. Indeed, even scattering of plasmons into plasmons by the solitons is weak ($t \ll 1$). Coupling of free-space photons to plasmons must be even weaker. Indeed, a good agreement between the experiment and the model leads us to conclude that polaritons launched by the tip and/or metallic contacts dominate our images.

2.6.6 Comparison of line profiles from experiment and superposition model

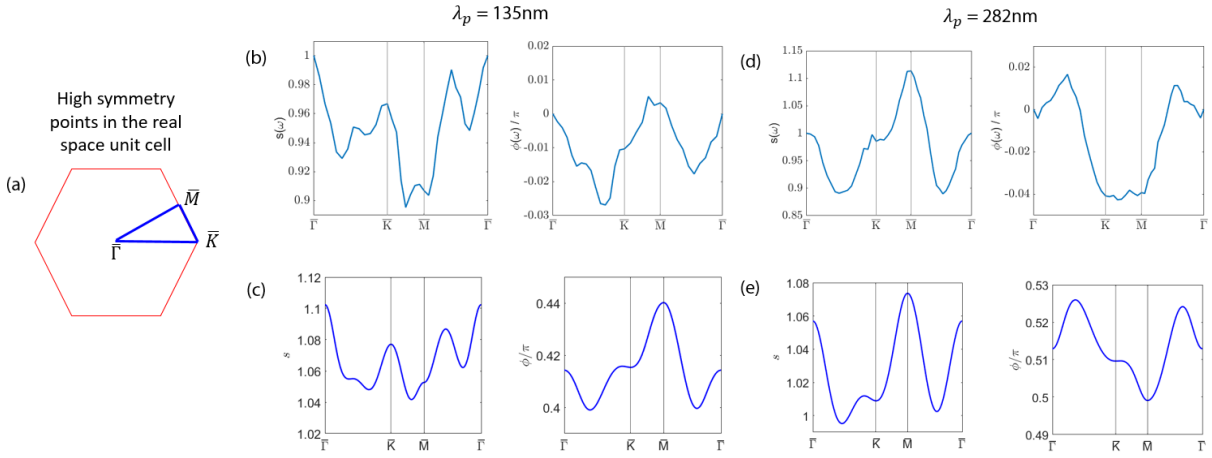

Figure 2.8 | Comparison of line profiles from experiment and superposition model. (a) Schematic showing the high-symmetry points of the real space hexagonal unit cell. (b, c) Experimental (b) and corresponding superposition model (c) line profiles for λ_p = 135nm. (d, e) Experimental (d) and corresponding superposition model (e) line profiles for λ_p = 282nm.

We further compared the experimental data with the superposition model by extracting line profiles from the images. In Figure 2.8(A), we label the high symmetry points of the real-space hexagonal unit cell. We then take line profiles along the paths between these points for both the experimental images and the images obtained from the superposition model. The comparison of line profiles is shown in Figure 2.8(B)-(E).

2.6.7 Fourier analysis of the scattering amplitude $s(\omega)$ images

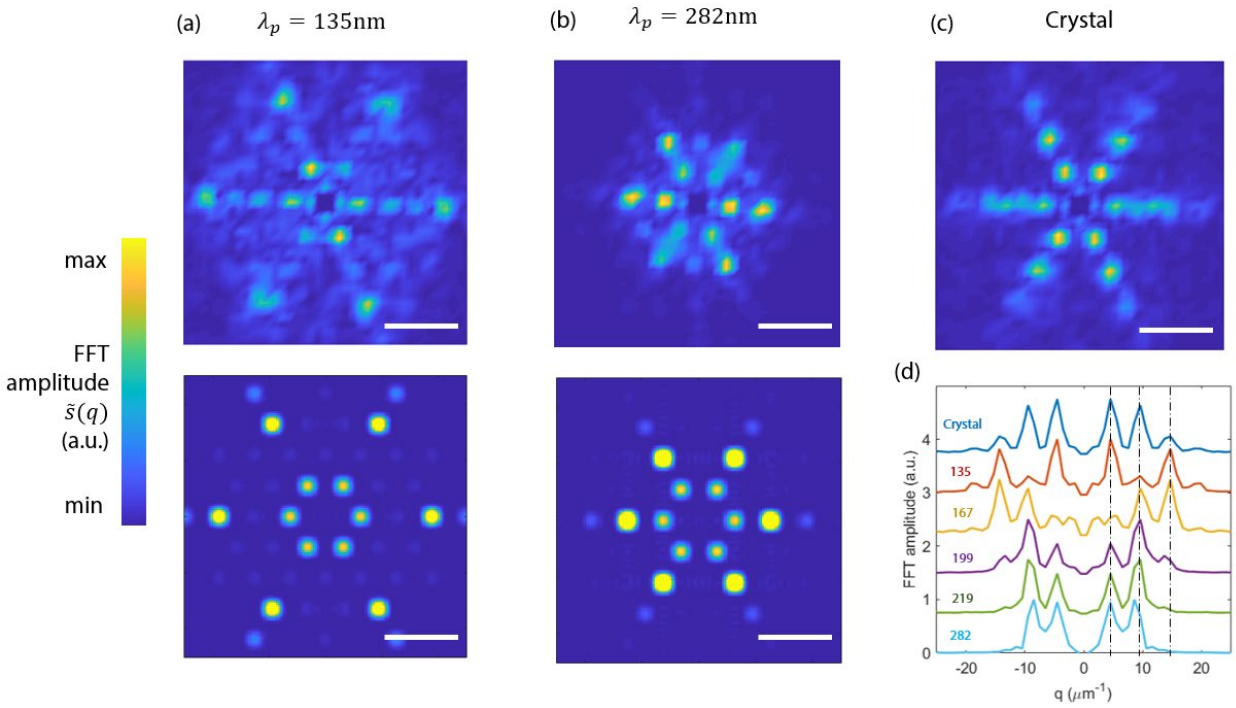

Figure 2.9 | Fourier analysis of the interference patterns. (a, b) Top: Fourier transforms of the experimental near-field amplitude, $\tilde{s}(q)$ for λ_p of 135nm and 282nm Bottom: Fourier transforms of the near-field amplitude obtained from the superposition model. (c) Fourier transform of the bare crystal imaged experimentally (Fig 2.1(C)). (d) Line-profiles extracted from the experimental Fourier amplitude for the bare crystal and for different values of λ_p taken along the white dashed line shown in (c). The black vertical dashed lines show the periodicities of the bare crystal. Scale bar 10μm^{-1}. The intense peak at the origin has been artificially removed from the experimental data.

Figures 2.9(A) and 2.9(B) show a comparison the Fourier transform of the near-field amplitude images obtained from experiment and the superposition model. All Fourier transforms show six-fold hexagonal symmetry, as expected from the symmetry of the crystal. Figure 2.3(B)

shows a plot of the line-profiles of the Fourier transforms taken along one of the high-symmetry directions. We notice that the peaks in the Fourier transforms always occur at the same positions as the peaks in the bare crystal. The only change in the line-profiles is the relative intensity of the peaks. This result shows that the periodicity of the near-field amplitude pattern at all plasmon wavelengths retains the periodicity of the bare crystal.

2.6.8 Plasmonic band structure

The plasmonic band structure can be derived directly from the equation for the quasistatic plasmon potential $\phi(\vec{r})$ for a periodically varying conductivity tensor $\sigma(\vec{r})$,

$$\phi(\vec{r}) = -\left(\frac{1}{\kappa r}\right) * \vec{\nabla} \cdot \left(\frac{1}{i\omega}\overleftrightarrow{\sigma}(\vec{r})\vec{\nabla}\phi(\vec{r})\right), \quad \vec{r} = (x, y). \tag{2.2}$$

The elements of the periodic conductivity tensor can be written in terms of reciprocal lattice vectors Q_i,

$$\sigma_{\alpha\beta}(\vec{r}) = \sigma_0\left(\delta_{\alpha\beta} + \sum_i \Sigma_{\alpha\beta}(\vec{Q}_i)e^{i\vec{Q}_i\cdot\vec{r}}\right), \{\alpha, \beta\} \in \{x, y\}$$

where σ_0 is the background conductivity. The potential $\phi(\vec{r})$ has the Bloch form

$$\phi_k(\vec{r}) = \sum_i c_i(\vec{k})e^{i(\vec{k}+\vec{Q}_i)\cdot\vec{r}}.$$

Equation (2.2) then becomes an eigenproblem. In k-space,

$$HC = q_p a C,$$

where the elements of H are

$$H_{ij} = \frac{1}{\sqrt{|\vec{k}+\vec{Q}_i||\vec{k}+\vec{Q}_j|}}(\vec{k}+\vec{Q}_i)\cdot\left[\overleftrightarrow{\Sigma}(Q_i - Q_j) + \delta_{ij}\right]\cdot(\vec{k}+\vec{Q}_j),$$

the eigenvector C has elements $C_i = \sqrt{|\vec{k}+\vec{Q}_i|}\cdot c_i$, and the eigenvalue is $q_p a = \frac{i\kappa\omega}{2\pi\sigma_0}a$.

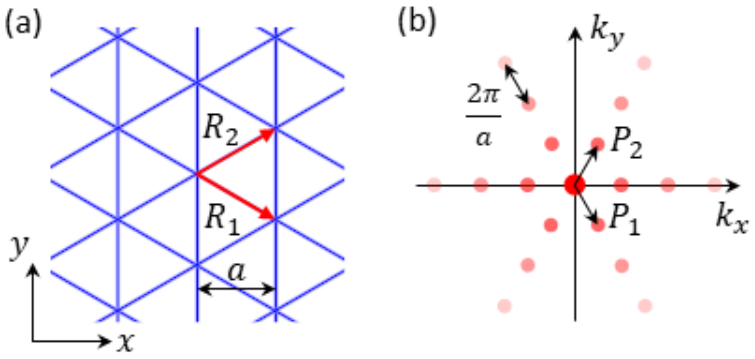

Figure 2.10 | Plasmonic crystal model (a) Lattice of domain walls in real space. R_1 and R_2 are the primitive lattice vectors, and a is the periodicity of the walls. (b) In k-space the crystal is represented by the Bragg peaks (red dots), where P_1 and P_2 are the primitive reciprocal lattice vectors.

In our model the crystal is composed of the superposition of domain walls in three directions with a periodicity a, as shown in Fig. 2.10(A). Each domain wall is assumed to have an isotropic conductivity profile,

$$\sigma_{\text{wall}}(x_\perp) = \sigma_0 \left[1 + \frac{ta}{\sqrt{2\pi}w} \cdot \exp\left(-\frac{x_\perp^2}{2w^2}\right)\right]$$

where the wall width $w = 6$ nm (*31*) and $x_\perp$ is the perpendicular distance to the wall.

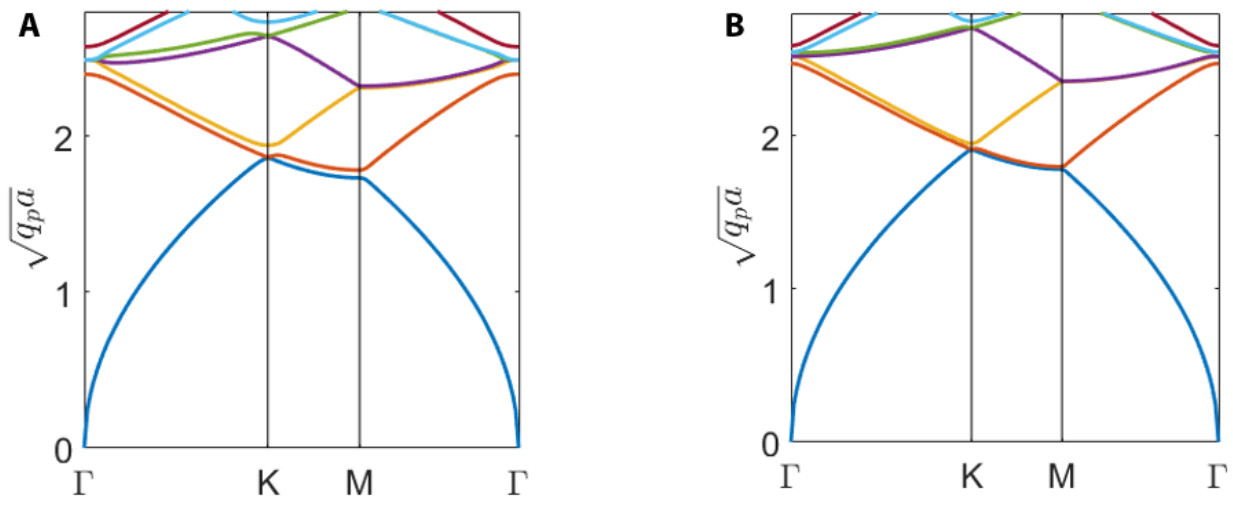

Figure 2.11 | Plasmonic band structures calculated using the parameters from superposition model. (A) Band structure corresponding to Figure 2.2(C) calculated using the following parameters: $\mu = 0.23$ eV, $V_i = 0.3$ V, $t_x = -0.032 - 0.027i$ and $t_y = 0.022 - 0.015i$. (B) Band structure corresponding to Figure 2.2(D) calculated using the following parameters: where $\mu = 0.35$ eV and $V_i = 0.1$ V, $t_x = -0.011 - 0.011i$ and $t_y = 0.025 - 0.002i$.

The dimensionless scattering strength t, assumed constant over all frequencies, is defined as

$$t = \frac{1}{a}\int_{-\infty}^{\infty} dx \, \frac{\sigma_{\text{wall}}(x) - \sigma_0}{\sigma_0}.$$

(Same as Equation (2.1)). We then have

$$\vec{\vec{\Sigma}}(\vec{Q}_i) = t\left(1 + 2\delta_{Q_i,0}\right)\exp\left(-\frac{w^2 Q_i^2}{2}\right)\cdot I, \vec{Q}_i \parallel \{\vec{P}_1, \vec{P}_2, \vec{P}_1 + \vec{P}_2\},$$

where I is the identity matrix and $\vec{P}_1$ and $\vec{P}_2$ are the primitive reciprocal lattice vectors, Fig. 2.10(B). The eigenvalues $q_p a$ can now be calculated numerically given a grid of $\vec{Q}_i$, which is chosen large enough that the results are independent of the grid size.

The plasmon wave around a δ-function impurity located at $\vec{r}'$ is given by the Green's function,

$$G(\vec{r},\vec{r}') = \int \frac{d^2k}{(2\pi)^2} e^{i\vec{k}\cdot(\vec{r}-\vec{r}')} \sum_i \tilde{G}_{\vec{k},\vec{k}+\vec{Q}_i} e^{-i\vec{Q}_i\cdot\vec{r}'},$$

where

$$\tilde{G}(E) = [H - (E + i0^+)]^{-1}.$$

Given an eigenvalue E, the location $\vec{r}'$, and the scattering strength t, the wave function $G(\vec{r},\vec{r}')$ can be found. The Green's function can also be used to simulate the SNOM image, with the tip replacing the impurity as both the launcher and the detector. The SNOM signal is then $|G(\vec{r},\vec{r})|$. To account for the finite size of the tip, we add the factor $F(\vec{k}) = k^2 e^{-2kd}$ to the integral(*81*) so that

$$G_{\text{tip}}(\vec{r}) = \int \frac{d^2k}{(2\pi)^2} F(\vec{k}) \sum_i \tilde{G}_{\vec{k},\vec{k}+\vec{Q}_i} e^{-i\vec{Q}_i\cdot\vec{r}} F(\vec{k}+\vec{Q}_i).$$

Here $d = 30$ nm is the radius of curvature of the SNOM tip.

2.6.9 Defect state located around the AB-region

In Figure 2.3(D) and 2.3(F), we showed the localized modes that arise from a point defect located at the AA region. A similar source at the center of the AB region leads to a three-fold symmetric pattern, as shown in Figure S9. The difference in the patterns directly reflects the difference in the symmetry of the plasmon wavefunction around that region and are helpful in visualizing the effect of the lattice on propagating plasmons.

We further comment that the observation of the localized plasmon patterns would require improvements to the experiment. First, since $t \propto (\mu a)^{-1}$, where μ is the chemical potential of the

TBG, the scattering strength can be increased by lowering μ and increasing a. In our experiment $\mu \simeq 0.25$ eV and $a \simeq 230$ nm, so a scattering strength of $t = 0.2$ at the same frequency can be achieved, for example, by reducing a to 70 nm and μ to 0.08 eV. A top gate may also be required to maintain the same value of perpendicular displacement field. Second, plasmonic damping can be reduced by fully encapsulating the TBG and performing the experiment at low temperature (*38*).

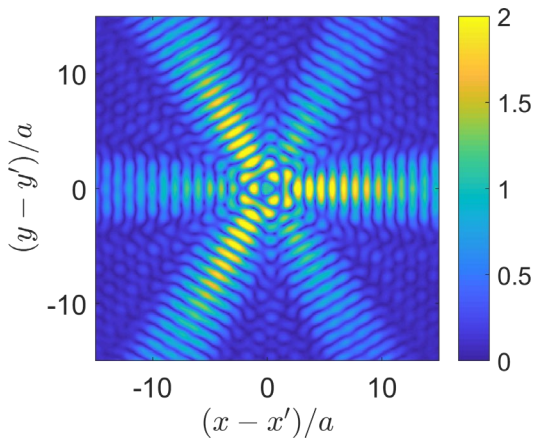

Figure 2.12 | Plasmon wave function $|G(\vec{r},\vec{r}')|$ around an impurity located at the center of the triangular AB region, $\vec{r}' = (0, 2a/3)$, normalized to the empty-lattice wave function. Parameters: $= 0.2$, $\sqrt{q_p a} = 2.23$.

Chapter 3: Mapping the Twist Angle with Nano-Optics

3.1 Introduction

We report a combined nano-photocurrent and infrared nanoscopy study of twisted bilayer graphene (TBG) enabling access to the local electronic phenomena at length scales as short as 20 nm. We show that the photocurrent changes sign at carrier densities tracking the local superlattice density of states of TBG. We use this property to identify domains of varying local twist angle by local photo-thermoelectric effect. Consistent with the photocurrent study, infrared nano-imaging experiments reveal optical conductivity features dominated by twist-angle dependent interband transitions. Our results provide a fast and robust method for mapping the electronic structure of TBG and suggest that similar methods can be broadly applied to probe electronic inhomogeneities of moiré superlattices in other van der Waals heterostructures.

The relative twist angle θ between proximal atomic layers is emerging as an extremely capable control parameter in van der Waals (vdW) heterostructures including twisted bilayer graphene (TBG). The twist leads to a spatial variation of the atomic stacking of proximal layers with the period given by $\lambda_M = 0.246\ \text{nm}/(2\sin(\theta/2))$ (*13*). The resultant structure is referred to as a moiré superlattice. The electronic structure of such a superlattice consists of a large number of minibands (*11*, *87*), exhibiting strong θ-dependent Van Hove singularities in the density of states (*13*, *88*, *89*). When θ is close to 1.1° ($\lambda_M \approx 13\text{nm}$), the lowest energy minibands in TBG specimens become nearly flat. At such "magic angle", TBG is found to host unconventional correlated electronic phases (*18*–*20*, *22*).

The electronic structure of TBG is not spatially uniform. Within the Moiré unit cell, changes in the atomic stacking lead to differences in the local density of states that have been observed by

scanning tunneling microscopy (STM) experiments (*90*–*93*). At small twist angles, where atomic relaxation leads to a periodic array of topologically protected states (*25*, *26*), scanning nano-infrared (Ref (*94*), Chapter 2) and STM (*73*) experiments have directly visualized such states. At larger length scales, variations in θ itself have been observed with multiple techniques. Low temperature transport experiments carried out as a function of the carrier density reveal a drop in conductivity when the four lowest energy minibands (which are nearly spin-valley degenerate) are completely filled (*89*, *95*) and the chemical potential reaches the superlattice band edge (SBE). The carrier density at the SBE, $n_s = 8/(\sqrt{3}\,\lambda_M^2)$, is governed by the superlattice period, and so, by θ. In such transport experiments done on different parts of the same TBG device, the drop in conductivity appeared at different carrier densities, indicating a change in θ across the device (*96*). STM (*90*, *92*), transmission electron microscopy (TEM) (*26*), scanning superconducting quantum interference device (SQUID) (*97*) and scanning single electron transistor (SET) (*98*) experiments have confirmed that the electronic structure variations persist down to sub-micron scales. Moreover, experiments on magic-angle TBG suggest that reducing such fluctuations can reveal the intrinsic transport properties of TBG (*99*). Taken together, these observations suggest that understanding the variations in electronic structure of TBG on a nanometer length scale is crucial.

Here we report that a nascent optoelectronic probe, scanning photocurrent nanoscopy (*4*, *100*, *101*), can map the DC conductivity of TBG as a function of carrier density, and thereby its twist angle, with a resolution better than 20 nm. In our experiments, the DC photo-generated current across the device is measured as a function of the position of a sharp metallized tip (Fig. 3.1(A)) (*4*). Room-temperature photocurrent imaging has been previously used to study excitations such as plasmon polaritons (*100*, *101*) and phonon polaritons (*102*) in other van der Waals materials. A crucial new element of our approach was performing the experiments at

cryogenic temperatures, which allowed us to visualize the insulating states in TBG (*89*, *95*). We further augmented our photocurrent results with room temperature nano-infrared imaging experiments. In tandem, our infrared and photocurrent data lead to a consistent interpretation of all the observables in terms of TBG twist-angle domains.

3.2 Nano-photocurrent at the interface between twisted bilayer and monolayer graphene

Our nano-photocurrent experiments rely on the photothermoelectric effect, the dominant mechanism for photocurrent generation in graphene layers (*55*, *59*). At the boundary between MLG and TBG, which we studied in this work, the magnitude of photocurrent is proportional to the difference in Seebeck coefficients of MLG and TBG. By exploiting this relationship, we determined the twist angle of the TBG region immediately adjacent to the boundary. We then performed carrier density dependent nano-infrared measurements which validated our nano-photocurrent results and provided further insight into the interband transitions that dominate the optical properties of TBG.

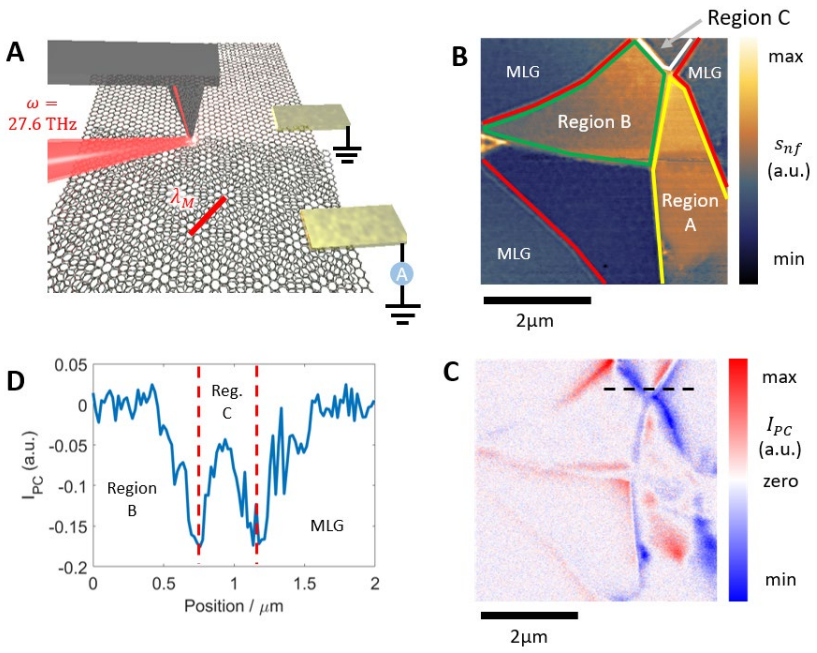

Figure 3.1 | Nano-photocurrent imaging of multi-domain twisted bilayer graphene. (A) Schematic of the experimental setup. The periodicity of the moiré pattern in TBG is denoted by λ_M. (B) Nano-infrared amplitude s_{nf} image showing contrast between TBG domains. The red lines enclose the TBG region. Scale bar 2μm. (C) Nano-photocurrent image of the same region as (B) at $T = 300$K. Scale bar 2μm. (D) Line profile of nano-photocurrent across the dashed line in (C) at $T = 300$K.

Our TBG structures were fabricated using the standard tear-and-stack method. The full devices included a thin top layer of hBN, the TBG, the SiO_2 substrate, Si gate, and electrical contacts (see Methods). The lack of an underlying hBN layer led to a high carrier density of $-1.8 \cdot 10^{13}\text{cm}^{-2}$ (determined through Raman spectroscopy and plasmon wavelength measurements on monolayer graphene, Section 3.6.2) even when no bias was applied to the back gate, $V_G = 0$V. We first performed room-temperature infrared nanoscopy (Fig. 3.1(A)), where we focused infrared light of frequency $\omega = 920\text{cm}^{-1}$ onto the tip, detected the backscattered light, and isolated its near-field

component s_{nf} (*35*, *81*, *103*). A representative s_{nf} image (Fig. 3.1(B)) demonstrates contrasting domains indicating differences in their optical conductivities. Since the optical conductivity $\sigma_{TBG}(\theta, \omega)$ of TBG is sensitive to θ (*104*, *105*), we interpret these domains as regions of distinct twist angles, similar to the domains previously observed by STM (*90*).

Next, we performed photocurrent nanoscopy. Figure 3.1(C) depicts I_{PC} measured in the same region as Fig. 3.1(B). We observe two key features. First, the magnitude of the photocurrent signal is enhanced when the tip is located over domain boundaries. The magnitude of I_{PC} varies along the boundaries, as most clearly seen for the boundary between monolayer graphene (MLG) and Region B. Second, we observe varying levels of photocurrent within Region A. In Fig. 3.1(D) we plot the photocurrent along the dashed line in Fig 3.1(C). The increase in the magnitude of photocurrent when the tip is above the boundaries leads to minima with widths of about 200 nm each (half width at half minimum) while the remaining features correspond to local variations in the photocurrent signal within the domain.

In general, photocurrent arises from an interplay of optical and transport phenomena that occur at different temporal and spatial scales. Two important length scales in our case are the tip radius and the cooling length. The former, of the order of 10 nm, sets the size of the field enhancement region where non-equilibrium charge carriers are generated and is also the spatial resolution of infrared nanoscopy (*36*). The latter can be a few hundred nanometers or longer in graphene, depending on the experimental conditions (*58*, *59*) and determines the size of the "hot spot" around the tip where the electron temperature remains elevated. Assuming that photocurrent is predominantly due to the photo-thermoelectric effect (PTE) (*55*, *58*), the photocurrent scales approximately as $I_{PC} \propto \Delta T \Delta S$, where ΔT is the change in electron temperature induced around the tip and ΔS is the change in the local Seebeck coefficient S across the hot spot,

whose direction determines that of the current flow. The photocurrent generated from the PTE also varies on the length scale of the cooling length. Therefore, photocurrent data represent a coarse-grained measurement of gradients in Seebeck coefficient. We observe this effect as enhanced I_{PC} at MLG-TBG and TBG-TBG boundaries due to a discontinuity ΔS of the Seebeck coefficient across such boundaries. The slower variation in I_{PC} along the boundaries is due to the changing direction of the current flow which is dictated by the geometry of the electrical contacts (Section 3.6.3). The remaining short-range variations of I_{PC} seen in Fig 3.1(D) are attributed to short-range variations of the optical conductivity. These latter contrasts likely arise from a combination of charge puddles and twist angle variations (*97*). Further experiments are needed to distinguish between these possibilities.

We now elucidate the ability of the nano-photocurrent method for characterizing the TBG domains using gate voltage dependent measurements. As pointed out above, the photocurrent near a TBG-MLG boundary is proportional to the difference in the Seebeck coefficient across the boundary: $I_{PC} \propto \Delta S = S_{TBG} - S_{MLG}$, where S_{TBG} and S_{MLG} are the Seebeck coefficients for TBG and MLG respectively. In this work, we will neglect the correlated electron physics in the moiré flat bands (*18*, *96*): a valid assumption for all twist angles away from the magic angle. Within this assumption, the Seebeck coefficient obeys the Mott formula for both MLG and TBG (Section 3.6, (*56*)):

$$S = -\frac{\pi^2 k_B^2 T_{el}}{3|e|}\frac{1}{\sigma}\frac{d\sigma}{d\mu} \tag{3.1}$$

where σ is the electrical conductivity of graphene, μ is the chemical potential, and T_{el} is the electronic temperature. The DC conductivity of MLG, σ_{MLG} shows a symmetric dip at the charge

neutrality point (CNP) $n = 0$ (Fig. 3.2(A), top). In turn, S_{MLG} is an odd function of the carrier density with peaks above and below the CNP (*106*) (Fig 3.2(B), top). Similarly, the calculated DC conductivity of TBG σ_{TBG} (Fig. 3.2(A) bottom) indicates that σ_{TBG} has three minima: one at the CNP and two more at carrier densities $n = \pm n_s$ associated with superlattice band edges (*89*). The Mott formula then predicts that the Seebeck coefficient S_{TBG} of TBG should exhibit characteristic zigzag-like variations versus carrier density close to $n = \pm n_s$ (Fig. 3.2(B), bottom). We note that direct measurement of the Seebeck coefficient of TBG through conventional thermoelectric measurements should also reveal the characteristic zigzag pattern.

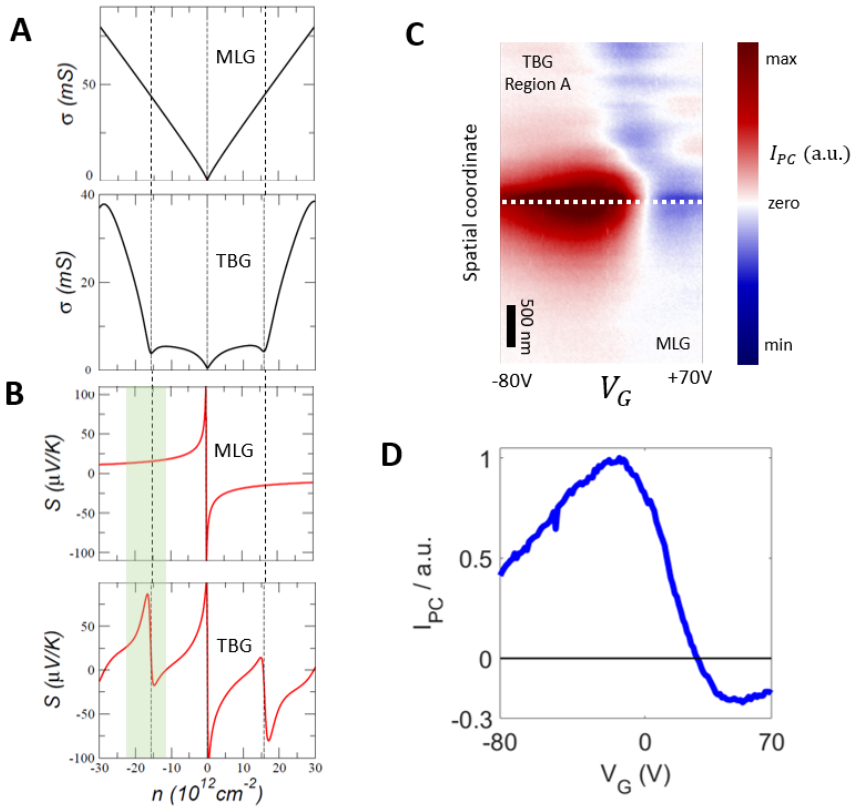

Figure 3.2 | Photocurrent spectroscopy at the interface between twisted bilayer graphene and monolayer graphene. (A) Calculated DC conductivity of MLG and TBG with $\theta = 2.65°$. (B) Calculated Seebeck coefficients for MLG and TBG with $\theta = 2.65°$. The dashed lines correspond

to the superlattice band edges and the green area corresponds to the experimentally measured range of densities in (C) and (D). (C) A nano-photocurrent carrier density sweep across a MLG-Region A interface acquired at $T = 200$K. (D) Gate voltage dependence of the photocurrent at the MLG-Region A boundary at $T = 200$K (white dashed line in (C)).

For moderately small twist angles, the analysis of the photocurrent signal can be further simplified. For $\theta > 1°$, $|n_s| > 3 \cdot 10^{12}$cm^{-2}, the Seebeck coefficient of MLG at $n = \pm n_s$ can be neglected in a first approximation compared to that of TBG (*57*, *106*), so that $I_{PC} \overset{\propto}{\sim} S_{TBG}$. Since S_{TBG} changes sign at $n = \pm n_s$, the photocurrent I_{PC} is also expected to change sign as well. Detection of such a zero crossing of I_{PC} measured locally as a function of n can then be used to estimate n_s and thereby the twist angle of TBG. We denote this estimate by θ_{PC}.

Nano-photocurrent experiments are robust to device architecture and disorder effects. The existence of the zero crossing in I_{PC} does not depend on geometric factors such as the position of the electrical contacts used to measure I_{PC} or the size and relative location of the TBG domains. Therefore, we can study multiple twist angle domains across the device with a single pair of electrical contacts. Further modelling developed in Section 3.64 shows that the sign change is also insensitive to fine details such as disorder strength which affects σ_{MLG} and σ_{TBG} and a finite value of S_{MLG} at $n = \pm n_s$, so long as σ_{TBG} exhibits a minimum at $n = \pm n_s$.

Since the SBEs in TBG are observable only at cryogenic temperatures (*95*), we performed nano-photocurrent experiments in a home-built ultra-high-vacuum platform for low temperature nano-imaging (*107*). Figures 3.2(C) and 3.2(D) show the results of such an experiment across a MLG/TBG interface at $T = 200$K. We see that the interface serves as a strong source of photothermoelectric current when the near-field probe is brought within proximity of a few

hundred nanometers. Recording I_{PC} while scanning repeatedly across this interface and changing the bias V_g applied to the gate electrode produces a spatial map of photocurrent at different carrier densities. For this particular MLG/TBG interface, we find a sign change in $I_{PC}(n)$ at a density $n_A = -1.58 \cdot 10^{13}\text{cm}^{-2}$ corresponding to $\theta_{PC} = 2.61°$ (Section 3.6.2). Further evidence for the presence of a SBE at this specific carrier density comes from the observation of line-like features in I_{PC} close to the sign change that only appear in the TBG region. Such features, previously observed in MLG and BLG close to CNP (*60*, *108*), can arise from spatial inhomogeneities in carrier density (*4*, *108*) as well as local variations in the twist angle (*97*) which lead to comparatively large spatial variations in Seebeck coefficient and serve as local sources of photocurrent. In our data, these features are spatially confined to the TBG region and only appear when n is close to n_A. The totality of these observations suggest that the Seebeck coefficient in TBG reveals spatial variations most prominently for carrier densities $n \approx n_A$, thereby confirming the presence of the SBE in Region A at $n = n_A$.

We applied the same protocol of nano-photocurrent imaging and gate sweeps at the Region B-MLG interface (Fig 3.1(C)). For Region B, we found no sign change at either $T = 200\text{K}$ or $T = 40\text{K}$ (data shown in Section 3.6.5). By constraining the densities at which the first order and second order superlattice band edges appear (Section 3.6.5.2), we conclude that $2.27° < \theta_{PC} < 2.34°$ for Region B. We have, therefore, measured the twist angle for two different regions of our device through nano-photocurrent with the same pair of electrical contacts.

3.3 Nano-infrared measurements of large angle twisted bilayer graphene

The large carrier density and limitations of the back-gate in our device prevented us from reaching the CNP or the SBEs for electron-doped Fermi levels in TBG. To confirm that our

assignment of θ_{PC} is accurate, we performed nano-infrared imaging experiments. In nano-IR experiments, infrared light incident on the metallic tip launches surface plasmon polaritons in graphene (*65*, *109*) which are reflected by physical (*48*, *49*) or electronic boundaries (*33*, *39*, *77*) and form standing wave patterns that can be directly imaged (*48*, *49*). The wavelength and the spatial decay length of the plasmons are directly related to the optical conductivity of the material at the energy of the incident light (*48*, *49*, *69*).

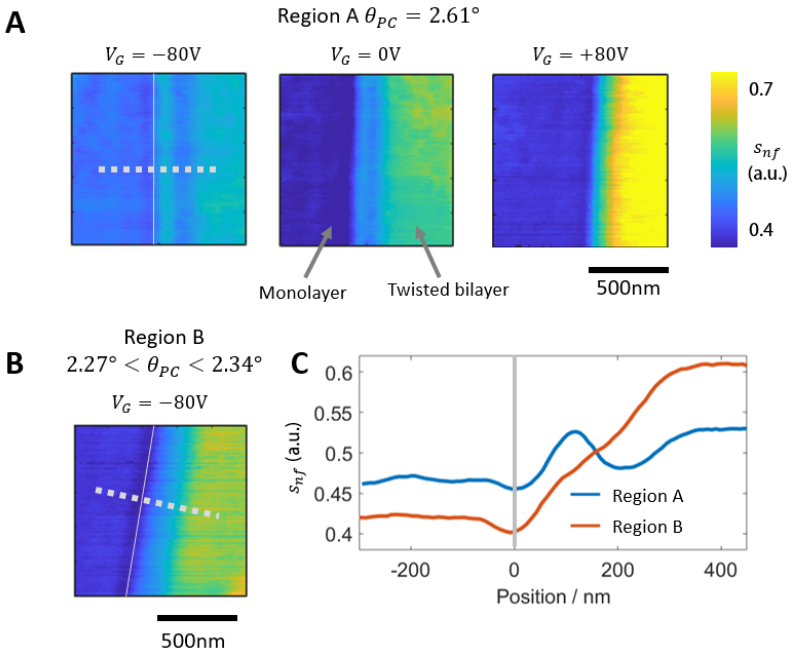

Figure 3.3 | Nano-infrared images of MLG-TBG interface. (A) Amplitude of the backscattered light s_{nf} images of Region A at three different values of V_G, demonstrating the gate voltage dependent plasmonic properties. (B) s_{nf} image of Region B at $V_G = -80\text{V}$. (C) Line profiles along the grey dashed lines in Fig 3.2(A) and 3.2(B) illustrating the difference in the plasmonic fringes. Grey solid lines indicate the MLG-TBG boundary. All images were acquired at $T = 300\text{K}$ with infrared light of frequency $\omega = 920\text{cm}^{-1}$.

Our nano-infrared imaging data taken at a MLG-TBG interface for Regions A and B are shown in Fig 3.3. We observe strong fringes on the TBG side of the MLG-TBG boundary, as seen in the line profiles in Fig 3.3(C), which we assign to plasmons propagating in TBG that are reflected by the MLG-TBG boundary. Plasmons propagating in MLG are also visible as faint fringes on the MLG side. The fringes in TBG are gate tunable (Fig 3.3(A)) and are strongly dependent on the twist angle (Fig 3.3(B), 3.3(C)), resulting from the optical conductivity of TBG being highly sensitive to the carrier density and twist angle.

We now compare our nano-infrared imaging data to theoretical models. We average the measured amplitude of the back scattered light s_{nf} in the TBG regions and plot it as a function of carrier density. We calculated the optical conductivity of TBG $\sigma_{TBG}(\theta, n)$ at $\omega = 920\text{cm}^{-1}$ using the continuum model ((*13*), Section 3.6) for the nine commensurate angles between 1.79° and 3.15°. We then applied a theoretical model of tip-sample coupling (*35*) to calculate $s_{nf}(\theta, n)$ from $\sigma_{TBG}(\theta, n)$ (Section 3.6). The results of our calculations are shown in Figure 3.4(B). The experimentally measured near-field optical response recorded from TBG in Regions A and B (Fig. 3.4(A)) are in excellent agreement with the calculations, thereby validating our estimates of the twist angle deduced from photocurrent nanoscopy.

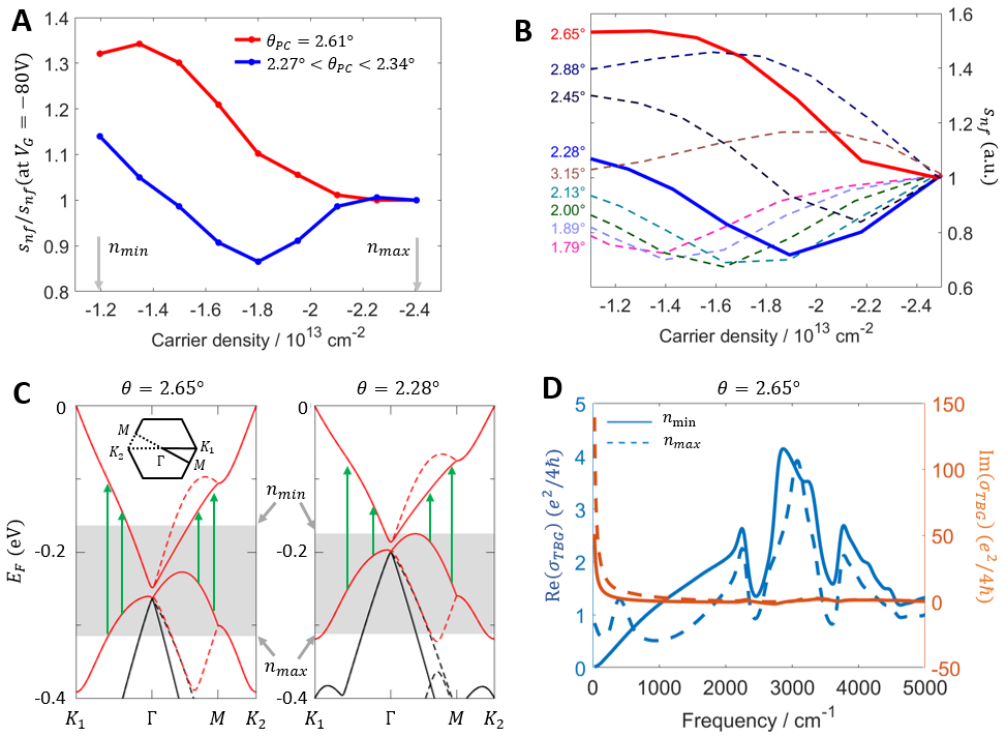

Figure 3.4 | Optical response of TBG at small angles. (A, B) s_{nf} as a function of carrier density in experiment (A) and in calculations based on the continuum model (B) at $\omega = 920\text{cm}^{-1}$. (C) Band structures for two different twist angles illustrating the twist angle dependent changes. Grey areas represent the range of carrier densities accessed in the experiment. The green arrows represent the optical transitions that are suppressed as the carrier density increases. Solid and dashed lines correspond to the solid and dashed paths through the moiré Brillouin zone as shown in the inset. (D) Real and imaginary parts of the optical conductivity calculated for $\theta = 2.65°$ at $n_{min} = -1.10 \cdot 10^{13}\text{cm}^{-2}$ (solid) and $n_{max} = -2.48 \cdot 10^{13}\text{cm}^{-2}$ (dashed).

3.4 Interband transitions and twist angle dependent nano-infrared signal

The features observed in $s_{nf}(n)$ provide further insight into the band structure of TBG. The decrease in $s_{nf}(n)$ for $\theta = 2.65°$ and the dip for $\theta = 2.28°$ for increasing n indicate the

presence of optical transitions that are being tuned by carrier density. Comparison with the calculated band structures for TBG at the associated twist angles demonstrates this is indeed the case. Figure 3.3(C) presents the band structure for TBG for $\theta = 2.65°$ and $\theta = 2.28°$. The Fermi energy E_F range accessible in our experiment is shown in gray, where the upper boundary corresponds to $n_{min} = -1.1 \cdot 10^{13}$ cm^{-2} and the lower boundary corresponds to $n_{max} = -2.48 \cdot 10^{13}$ cm^{-2}. We see that towards the higher range of attainable E_F, transitions between the minibands such as those shown by the green arrows are suppressed. This suppression leads to a decrease in the real part of the optical conductivity at the probing frequency of 920cm^{-1} (Figure 3.3(D)) and a corresponding drop in $s_{nf}(n)$ for $\theta = 2.65°$. For $\theta = 2.28°$, $s_{nf}(n)$ begins to increase at $n < -1.8 \cdot 10^{13}\text{cm}^{-2}$ as transitions between other minibands begin to contribute (Section 3.6.6).

The cryogenic photocurrent nanoscopy technique utilized here can be applied broadly to characterize the electronic structure of TBG and its variation across macroscopic structures. Photocurrent nanoscopy can also be applied to moiré patterns in other vdW heterostructures. When graphene is placed on hBN, twist-angle dependent SBEs, similar to those in TBG, appear (*17*, *110*). Photocurrent nanoscopy is well suited to resolve local changes in the twist angle in such structures. Domains of different stacking orders in multilayer graphene such as ABC and ABA stackings in trilayer graphene (*111*) can also be probed with nano-photocurrent imaging. Recently, evidence for local variations of the excitonic properties due to moiré patterns in transition metal dichalcogenide (TMD) bilayers (*112–115*) has been reported. While far-field photocurrent experiments have demonstrated sensitivity to the exciton resonance in TMDs (*116*), cryogenic photocurrent nanoscopy needs to be applied to resolve sub-micron changes in the excitonic properties of TMD bilayers.

3.5 Conclusion

To conclude, we have demonstrated the utility of nano-photocurrent technique to locally probe the electronic structure of small-angle TBG and to determine its twist angle with nano- and mesoscale spatial resolution. The technique detects local variations in the photothermoelectric effect in graphene, which is highly sensitive to formation of a superlattice band edge in TBG, thus providing a fast, robust and transport-compatible method for evaluating the twist angle of TBG. Photocurrent nanoscopy does not require any special device architectures and only necessitates optical access to the graphene layers together with a pair of global electrical contacts. Photocurrent nanoscopy can also be extended to characterize the electronic structure of other van der Waals heterostructures such as multilayer graphene and TMDs.

3.6 Supplementary Material

3.6.1 Materials and Methods

3.6.1.1 Device fabrication

Our device consists of twisted bilayer graphene fabricated using the tear-and-stack technique with the graphene directly on SiO_2. First a layer of boron nitride (BN) is picked up using an adhesive polymer poly(bisphenol A carbonate) (PC) coated on a stamp made of transparent elastomer polydimethylsiloxane (PDMS). A large flake of monolayer graphene is identified and the BN flake is used to tear the graphene flake into two and pick up one half. The substrate is then rotated by a controlled angle and the second half of the graphene flake is picked up. The entire stack is then placed directly on a silicon dioxide/silicon substrate without a bottom BN layer. The presence of dopants on the SiO_2 surface leads to a high carrier density in graphene even without

the application of a gate voltage. The same device was investigated in our previous work on photonic crystals (Ref (*94*), Chapter 2).

3.6.1.2 Infrared nano-imaging

Infrared nano-imaging was performed with a commercial scattering-type scanning near-field optical microscope (s-SNOM) based on a tapping mode atomic force microscope from Neaspec GmbH. Our light source was a quantum cascade laser obtained from DRS Daylight Solutions, tunable from 900 cm^{-1} to 1200 cm^{-1}. The light from the laser was focused onto a metallic tip oscillating at a tapping frequency of around 250 kHz with a tapping amplitude of around 60 nm. The scattered light was detected using a liquid nitrogen cooled HgCdTe (MCT) detector. To suppress far-field background signals, the detected signal was demodulated at a harmonic n of the tapping frequency. In this work, we used $n = 3$.

3.6.1.3 Nano-photocurrent

Room temperature nano-photocurrent measurements were performed in a commercial s-SNOM from Neaspec GmbH. Low temperature nano-photocurrent measurements were performed in a home-built ultrahigh vacuum chamber (*107*). The incident laser power was around 20mW for room temperature experiments and 40mW for low temperature experiments. The current was measured using a Femto DHPCA-100 current amplifier. To isolate the photocurrent contributions from the near-fields localized under the tip, the measured current was demodulated at a harmonic n of the tapping frequency. In this work we used $n = 2$. The gate sweeps were performed by scanning the same line repeatedly while slowly changing the gate voltage. We typically swept the gate voltage at a rate of 100mV/sec while the time required to scan a single line was about 10 seconds.

3.6.2 Carrier density and superlattice band edges

3.6.2.1 Estimating the carrier density in our device

We estimate the carrier density in two ways: plasmon wavelength in monolayer graphene and Raman experiments. Both experiments confirm that the carrier density at $V_G = 0\text{V}$ is $\sim -1.8 \cdot 10^{13}\text{cm}^{-2}$. This extremely large carrier density is likely the result of doping from the SiO_2 surface that the graphene directly sits on. In the room temperature nano-infrared experiments, we were able to apply gate voltages between $V_G = -80\text{V}$ and $V_G = +80\text{V}$. However for the low temperature nano-photocurrent experiments, we could only reach $V_G = +70\text{V}$.

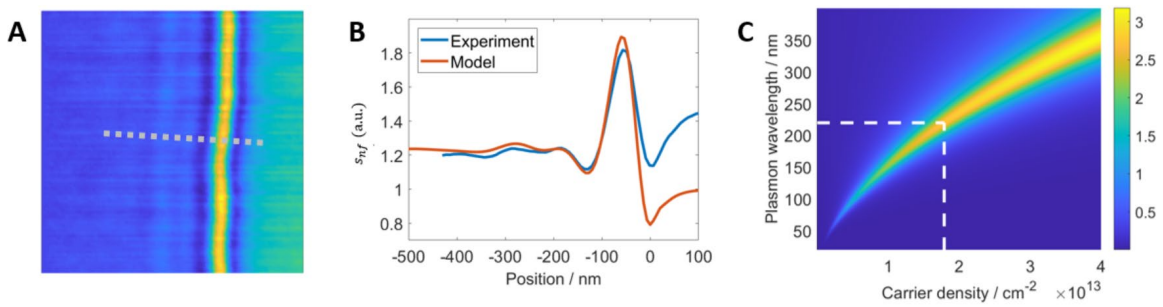

Figure 3.5 | Nano-infrared image of MLG used to estimate the carrier concentration. (A) Nano-infrared image acquired at a MLG edge. (B) Line profile perpendicular to the edge along with a fit using $\lambda_p = 220$nm. (C) Plasmon dispersion for the BN/MLG/SiO2/Si heterostructure. A plasmon wavelength of 220nm corresponds to a carrier concentration of $1.78 \cdot 10^{13}$cm^{-2}.

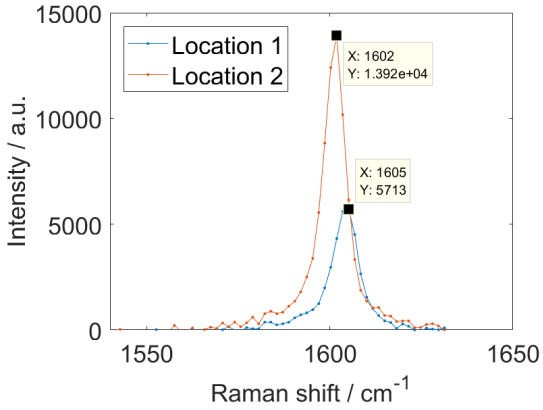

Figure 3.6 | Raman measurements on MLG at $V_G = 0$V. The position of the G peak is around 1603cm^{-1} which corresponds to a carrier density of $\sim -1.75 \cdot 10^{13}$cm^{-2} (*117*).

3.6.2.2 Carrier density at the superlattice band edges

The carrier density at which SBEs occur can be calculated as follows. The first SBE appears when the first moiré band is filled. Since the band structure of TBG is four-fold degenerate

(including spin and valley), this corresponds to 4 carriers per moiré unit cell. The area of the moiré unit cell is given by:

$$A_M = \frac{\sqrt{3}}{2}\lambda_M^2 \tag{3.2}$$

Therefore, the density at the SBE, n_s is given by:

$$n_s = \frac{4}{A_M} = \frac{4}{\frac{\sqrt{3}}{2}\,\lambda_M^2} = \frac{4}{\frac{\sqrt{3}}{2}\left(\frac{a}{2}/\sin\left(\frac{\theta}{2}\right)\right)^2} \tag{3.3}$$

where a = 0.246nm is the lattice constant of monolayer graphene. Eq 3.3 provides a direct relationship between n_s and θ and allows for a determination of θ from a measurement of n_s.

3.6.3 Large area nano-infrared and nano-photocurrent images

Large area nano-infrared and nano-photocurrent images are shown in Figure 3.7. The electrode configuration for nano-photocurrent experiment in shown in Fig 3.7(A). The electrodes labeled '1' and '2' served as source and drain respectively. The electrode labeled 'float' was left floating. Previous work on photocurrent generation in graphene has shown that the measured geometric pattern of the photocurrent is strongly sensitive to the geometry of the electrical contacts (*59*). The unusual geometry used here results is responsible for the variations of the measured signal across the boundaries, as seen in Figure 3.1(C).

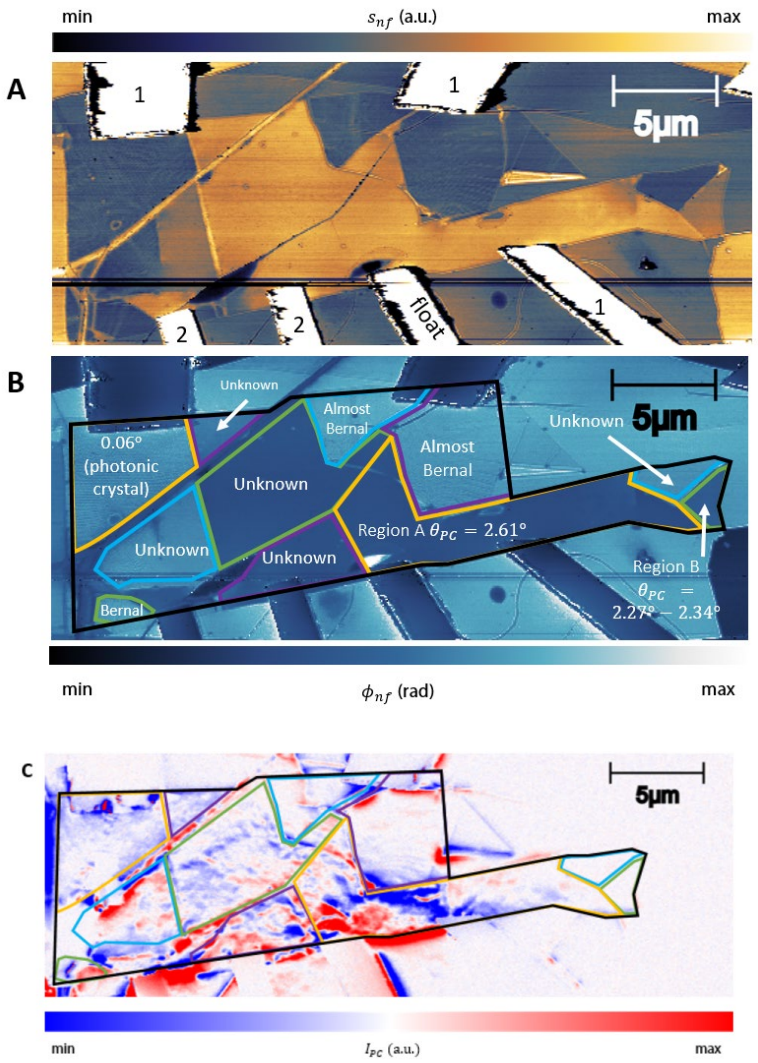

Figure 3.7 | Large area images of our device. (A) Nano-infrared image of the amplitude s_{nf}. The bright white regions are the gold electrodes and the numbers indicate the electrode configuration used for photocurrent experiments. (B) Nano-infrared image of the phase ϕ_{nf}. The various regions of the sample are marked. 'Unknown' refers to regions that we were unable to determine the twist angle conclusively. (C) Nano-photocurrent image. The colored lines in (B) and (C) correspond to the boundaries of domains with different twist angles. All images were acquired at $V_G = 0$V and at room temperature.

3.6.4 Simple model for photocurrent at a MLG-TBG interface

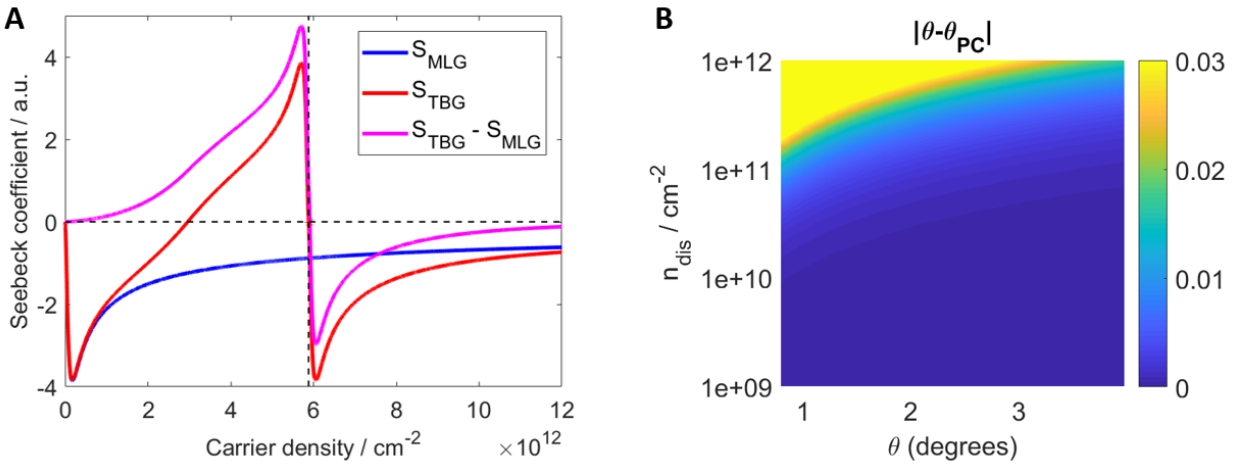

Figure 3.8 | Simple model for photocurrent at a MLG-TBG interface. (A) Seebeck coefficient for MLG, TBG and their difference as a function of carrier density. The parameters used are $\theta = 1.59°$ and $n_{dis} = 1 \cdot 10^{11}\text{cm}^{-2}$. The horizontal dashed line represents $S = 0$ and the vertical dashed line represents the SBE for the TBG. (B) A color plot of $|\theta - \theta_{PC}|$ as a function of θ and n_{dis}. A significant difference between θ and θ_{PC} is only observed for $n_{dis} > 10^{11}\text{cm}^{-2}$.

In the following, we develop a simple model for the photocurrent generated at a MLG-TBG interface. First, we assume that the resistivity of MLG can be parametrized by a single quantity n_{dis} which is the full-width half-maximum (FWHM) of the resistivity as a function of carrier density and is a measure of the disorder in the device:

$$R_{MLG} = \left(1 + \frac{n^2}{n_{dis}^2}\right)^{-1}$$

For TBG, we can consider three contributions: one from the CNP and two from the SBEs:

$$R_{TBG} = \left(1 + \frac{n^2}{n_{dis}^2}\right)^{-1} + \left(1 + \frac{(n-n_s)^2}{n_{dis}^2}\right)^{-1} + \left(1 + \frac{(n+n_s)^2}{n_{dis}^2}\right)^{-1}.$$

We can then use the Mott formula to calculate the Seebeck coefficient for MLG and TBG and use that to estimate the difference between the actual twist angle θ and the twist angle estimated from the nano-photocurrent measurements θ_{PC}. Figure S3.8(A) shows an example of the Seebeck coefficient curves that result from the above model. Figure 3.8(B) shows the relationship between $|\theta - \theta_{PC}|$ as a function of θ and n_{dis}. From Fig 3.8(B), we see that the difference between θ and θ_{PC} is significant only when n_{dis} exceeds $\sim 10^{11} cm^{-2}$. The latest generation of high quality encapsulated graphene devices show $n_{dis} \sim 10^{9}$ cm^{-2} (*118*). Furthermore, at small twist angles, the SBEs show finite electronic gaps (*119*, *120*) which would lead to sharper changes in the resistance and Seebeck coefficient as a function of the density close to the SBEs, leading to a smaller difference between θ and θ_{PC}. Therefore, for practical experiments, θ and θ_{PC} can be considered to be identical.

3.6.5 Photocurrent data for other twist angles and temperatures

3.6.5.1 Nano-photocurrent data for Region A $\theta_{PC} = 2.61°$ *at* $T = 40\text{K}$

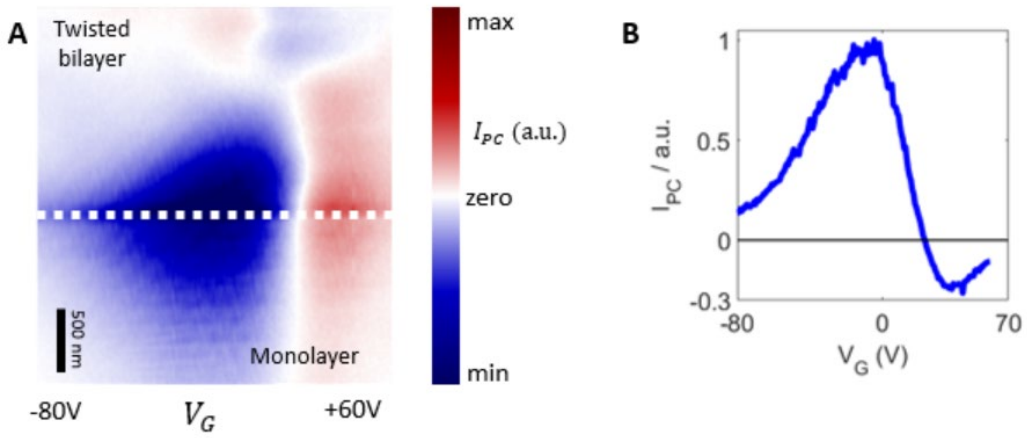

Figure 3.9 | Nano-photocurrent data for the $\theta_{PC} = 2.61°$ region at $T = 40\text{K}$. (A) Nano-photocurrent image. (B) Line profile along the white dashed line in (A). The sign change in I_{PC} occurs at a density of $-1.62 \cdot 10^{13}\text{cm}^{-2}$ which is very similar to the sign change density at $T = 200\text{K}$ of $-1.58 \cdot 10^{13}\text{cm}^{-2}$ (shown in Figure 3.1).

3.6.5.2 Nano-photocurrent data for Region B ($2.27° < \theta_{PC} < 2.34°$)

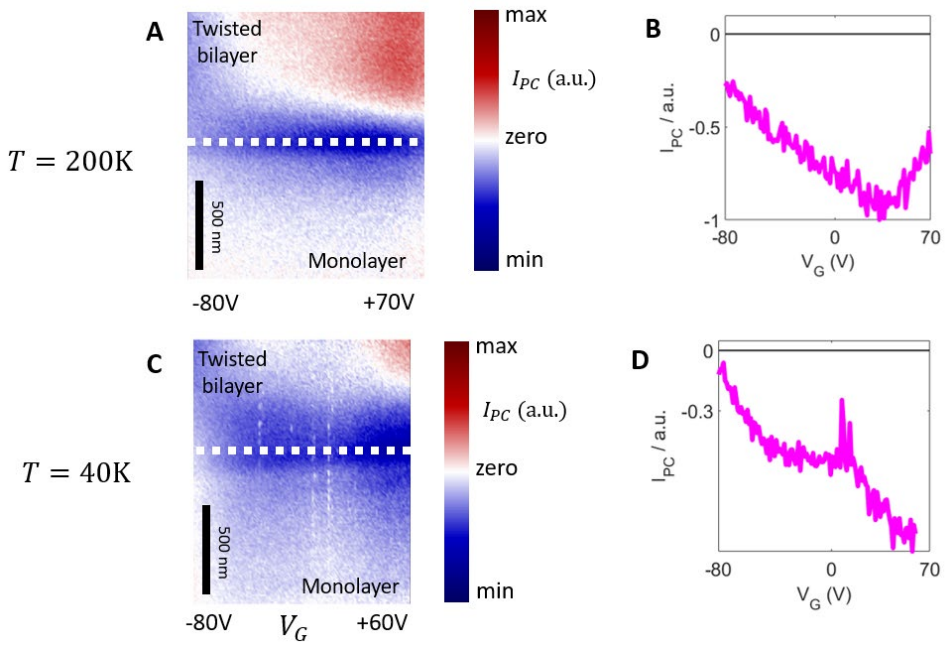

Figure 3.10 | Nano-photocurrent data for the $2.27° < \theta_{PC} < 2.34°$ region (A) Nano-photocurrent image and (B) Line profile at $T = 200$K. (C) Nano-photocurrent image and (D) Line profile at $T = 40$K.

For this region, we do not observe a sign change in I_{PC}. However, we can place bounds on the twist angle by considering the range of carrier densities accessible in our experiment. There are two possibilities. In the first possibility, the twist angle is so large that the SBE density is greater than n_{max}. This requirement leads to a bound of $\theta_{PC} > 3.21°$. The second possibility is that the twist angle is so small that the SBE density is below n_{min}. This requirement leads to a bound of $\theta_{PC} < 2.34°$. However, a lower bound may also be established in this case by requiring that the second order SBE (observed at smaller angles in (*121*, *122*) and predicted by our calculations in Figure 3.12, Section 3.6.6) be above n_{max}, leading to the bound $\theta_{PC} > 2.27°$. Combining the two bounds, we get $2.27° < \theta_{PC} < 2.34°$. Because this second possibility is a more stringent

requirement on θ_{PC}, we use this requirement earlier in the chapter. The good agreement between the nano-infrared signal in Fig 3.3 is further confirmation that our estimate of θ_{PC} is accurate.

In the $T = 40$K data for Region B, we observe a suppression in photocurrent at $V_G \sim 12$V. We believe that this effect is likely the result of Region A being at the SBE. Since Region B is located away from the electrodes, the photocurrent must flow through Region A to reach the electrodes. If Region A were to become gapped, it will lead to an apparent suppression of the photocurrent from Region B.

3.6.5.3 Real space nano-photocurrent images of Region A

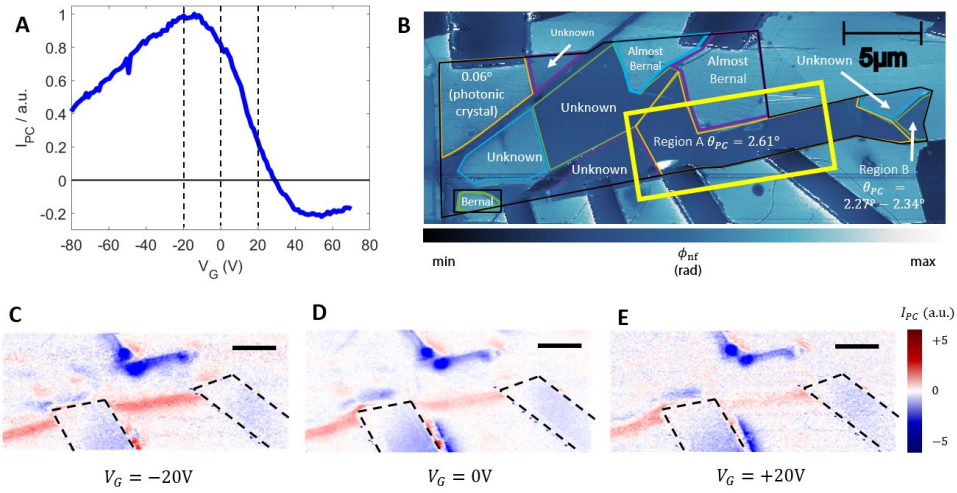

Figure 3.11 | Real space nano-photocurrent images of Region A and its boundary with MLG. (A) Gate voltage dependence of the photocurrent at a Region A-MLG interface (same as Fig 3.1(E)). (B) Large area near-field phase image (same as Fig 3.7(B)). The yellow rectangle marks the region shown in panels C-E. (C-E) Nano-photocurrent image at three different values of V_G. The photocurrent at the boundary decreases as V_G changes from -20V to +20V as expected from the voltage dependence in panel A. Panel A was acquired at $T = 200$K and panels C-E were acquired at $T = 160$K.

3.6.6 Conductivity and Seebeck coefficient calculations

The DC conductivity and Seebeck coefficient of MLG and TBG were calculated using semiclassical Boltzmann theory (*123*, *124*) within the continuum model. We assumed an energy dependent scattering rate originating from Coulomb interactions as well as short-ranged scatterers and used Eq 2 and Eq 3 from Ref (*123*). For the temperature range used in our experiments, the Seebeck coefficient can be obtained from the conductivity as function of the chemical potential using the Mott formula (Eq 9 of (*123*)) thus justifying the use of Mott formula also in TBG (Figure 3.11).

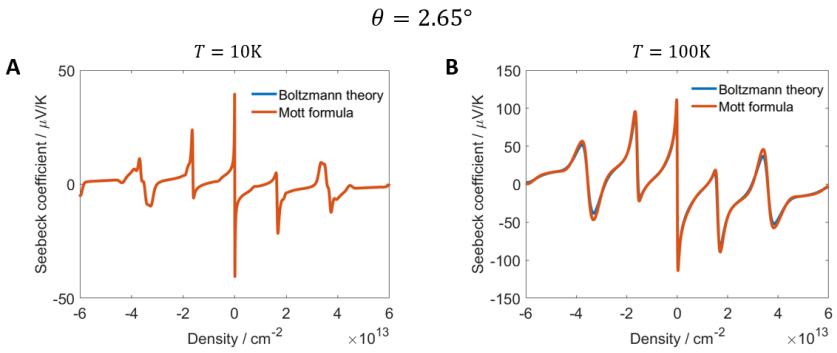

Figure 3.12 | Comparison between Boltzmann theory and the Mott formula. Seebeck coefficient of TBG with $\theta = 2.65°$ calculated using Boltzmann theory and the Mott formula at $T = 10\text{K}$ and $T = 100\text{K}$. The good agreement justifies the use of Mott formula in TBG.

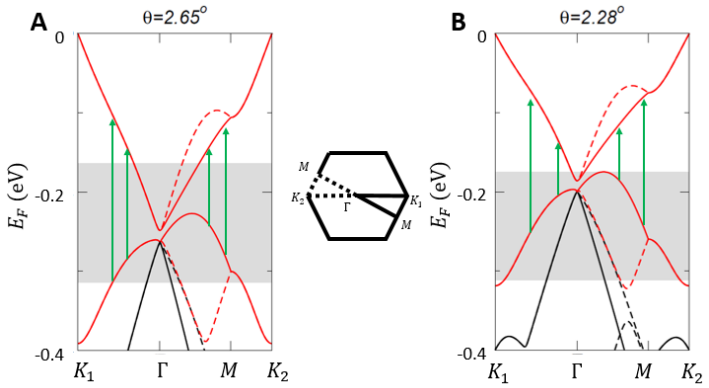

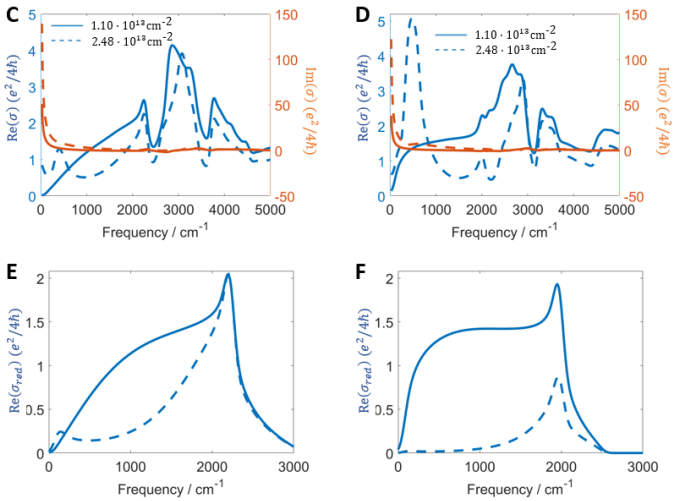

Figure 3.13 | Optical conductivity spectra for different twist angles. (A, B) Band structures for twisted bilayer graphene with $\theta = 2.65°$ and $\theta = 2.28°$ (same as Fig 3.4(C)). (C, D) Optical conductivity spectra for $\theta = 2.65°$ and $\theta = 2.28°$ at $n = 1.1 \cdot 10^{13}\text{cm}^{-2}$ (solid) and $n = 2.48 \cdot 10^{13}\text{cm}^{-2}$ (dashed). (E, F) Re(σ_{red}) spectra including only the transitions between the red bands in (C, D).

Optical conductivity of TBG was calculated again using a continuum model. First, the real part of the optical conductivity was obtained by replacing the delta-function by a Gaussian with variance of 3 meV. The imaginary part was then obtained from the Kramers-Kronig relation after adding the constant background $\sigma_0 = e^2/2\hbar$ for frequencies larger the cut-off frequency set by the continuum model (*104*). The Drude peak in the absorption was neglected due to the large relaxation times estimated to significantly exceed 1fs.

Figure 3.12 shows the optical conductivity spectra of TBG with $\theta = 2.65°$ and $\theta = 2.28°$. Fig 3.12(E) and 3.12(F) show the real part of the optical conductivity Re(σ_{red}) obtained by considering only the two red bands in Fig 3.13(A) and 3.13(B). Re(σ_{red}) is suppressed at $n =$

$2.48 \cdot 10^{13}\text{cm}^{-2}$ as compared to $n = 1.10 \cdot 10^{13}\text{cm}^{-2}$ because the red bands are no longer occupied. However, $\text{Re}(\sigma)$ for $\theta = 2.28°$ still shows a strong peak at 500cm^{-1} at the higher density. This resonance does not arise from the red bands, but is the result of transitions from other moiré-modified bands at more negative Fermi energies.

3.6.7 Lightning rod model

We used the lightning rod model (LRM) (*35*) to calculate the expected near-field amplitude of our hBN/TBG/SiO_2/Si heterostructure. The inputs for the LRM are the dielectric constants for each of the layers, the thicknesses of the layers and the radius of curvature of the tip. We used the output of the continuum model calculations for the conductivity of the TBG. For the dielectric constants of hBN and SiO_2, we used the parametrizations reported in Ref (*125*) and Ref (*126*) respectively. We estimated the radius of curvature of the tip to be around 15nm for our nano-infrared experiments.

Chapter 4: Domain walls and their photocurrent response

4.1 Introduction

Quasi-periodic moiré patterns and their effect on electronic properties of twisted bilayer graphene have been intensely studied. At small twist angle θ, due to atomic reconstruction, the moiré superlattice morphs into a network of narrow domain walls separating micron-scale AB and BA stacking regions. We use scanning probe photocurrent imaging to resolve nanoscale variations of the Seebeck coefficient occurring at these domain walls. The observed features become enhanced in a range of mid-infrared frequencies where the hexagonal boron nitride substrate is optically hyperbolic. Our results illustrate the capabilities of the nano-photocurrent technique for probing nanoscale electronic inhomogeneities in two-dimensional materials.

Twisted bilayer graphene (TBG), consisting of two graphene sheets rotated with respect to each other, has emerged as a tunable platform for studying exotic electronic phases. Transport experiments have revealed that when the graphene layers are twisted by a magic angle of $\theta \sim 1.1°$, TBG can become a superconductor (*19*), a correlated insulator (*18*), or a quantum anomalous Hall insulator (*22*, *23*, *127*). A key feature of TBG is the moiré superlattice: a long-range variation in the atomic stacking arising from geometric interference of the lattice periodicities in the two graphene sheets. Scanning probe studies of TBG with $\theta \sim 1.1°$demonstrated spatial variations in the electronic properties occurring on the length scale of tens of nanometers (*90*–*93*).

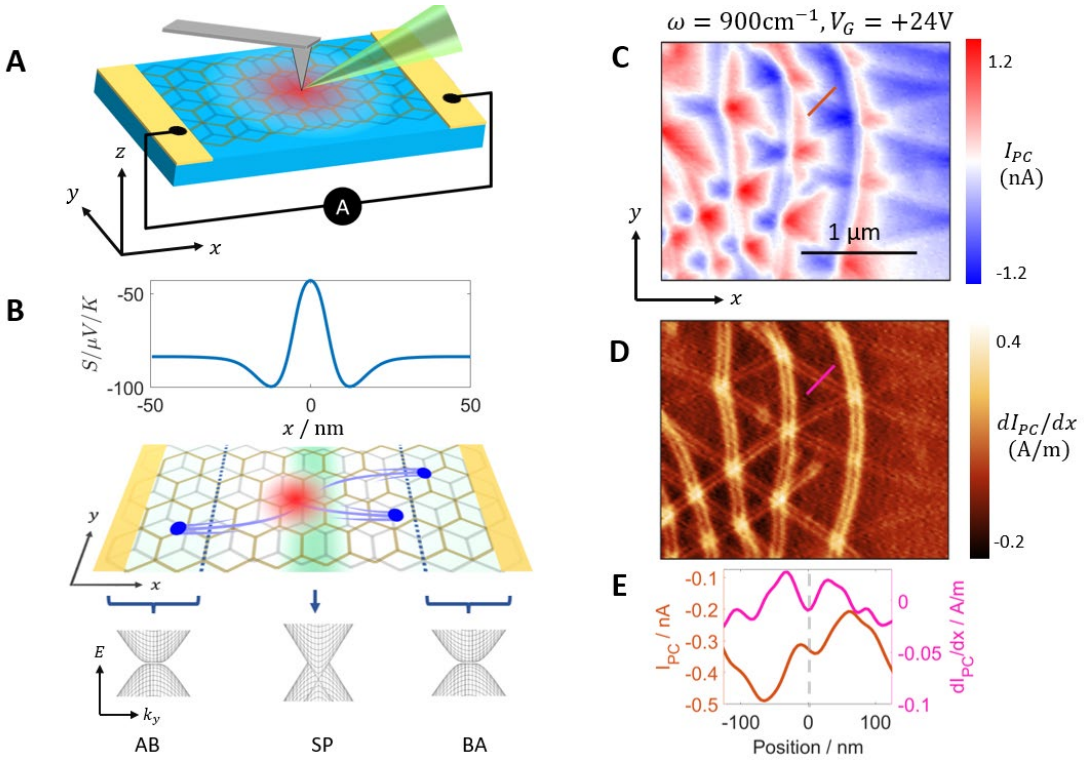

Figure 4.1 | Photocurrent in minimally twisted bilayer graphene. (A) A schematic of scanning photocurrent setup. The red region represents the hot carriers generated under the tip. (B) Top: Seebeck coefficient S profile across a domain wall calculated from first principles (Section 4.5.3). The DW is located at $x = 0$. Middle: perspective view of the experiment showing photocurrent generation at the domain wall. The green background represents the Seebeck coefficient profile and the blue dots represent carriers generated by thermoelectric effect. Bottom: schematic of the BLG band structure across the DW for three different stackings AB, BA and saddle point (SP). (C) Photocurrent (I_{PC}) image taken with $\omega = 900$ cm^{-1} and $V_G = +24$ V at $T = 300$ K. (D) Spatial gradient of the photocurrent defined as dI_{PC}/dx of the data in (C). (E) Line profiles of I_{PC} and dI_{PC}/dx across a DW (shown as red and magenta lines in (C) and (D)).

In minimally twisted bilayer graphene (MTBG), the moiré pattern periodicity is large, e.g., 140 nm for $\theta \approx 0.01°$ and prone to atomic relaxation. In the relaxed state, the Bernal stacked domains (AB and BA) dominate while the less stable stacking configurations are reduced to a network of narrow domain walls (DWs). TEM measurements have shown that the DWs are 6-9 nm wide (*31*). Previous transport (*32*), nano-infrared (Refs (*34*, *94*), Chapter 2), and STM (*128*) studies have revealed the existence of topological states at the DWs when an electronic bandgap is opened by a sufficiently large interlayer bias between the graphene sheets. At smaller interlayer biases, the change in the atomic stacking across the DW still leads to a change in the electronic properties.

Scanning nano-photocurrent imaging has emerged as a novel optoelectronic probe capable of resolving changes in DC transport properties of graphene with nanometer scale spatial resolution (*4*). Previous nano-photocurrent experiments have resolved charge inhomogeneities and grain boundaries in monolayer graphene (*4*) and mapped variations in twist angle of TBG at twist angles $\theta > 1°$ (Ref (*129*), Chapter 3). Here we use scanning nano-photocurrent imaging to study domain walls in MTBG. We show that the photocurrent patterns arise from DC Seebeck coefficient variations occurring at the DWs on a nanometer length scale. We further propose and demonstrate a mechanism that utilizes the intrinsic hyperbolicity of the hBN substrate to enhance the DW features in photocurrent images.

4.2 Photocurrent imaging at $\omega = 900\ \mathrm{cm}^{-1}$

Figure 4.1(A) shows a schematic of our experiment. Infrared light is focused onto the apex of a sharp metallic tip which enhances the electric field underneath the tip. The enhanced field locally generates a photocurrent which we collect through electrical contacts at zero bias. In

graphene, the photocurrent arises from electronic inhomogeneities through the photothermoelectric effect (PTE), schematically shown in Figure 4.1(B) (*55*, *58*, *60*). Photocurrent images are acquired by raster scanning the tip across the sample. Our technique overcomes the diffraction limit and provides a spatial resolution of about 20 nm while also allowing for simultaneous nano-infrared imaging (*4*). Our device consists of two graphene layers with a minimal relative twist encapsulated between 37 nm bottom hexagonal boron nitride (hBN) layer and 6nm top hBN layer. The entire stack rests on a 285 nm SiO_2/Si substrate with the SiO_2 layer serving as the gate dielectric. Piezoresponse force microscopy (PFM) (*130*) before encapsulation of the device revealed domain walls with a periodicity of about 500 nm (Section 4.5.1).

Figure 4.1(C) shows a representative photocurrent image of our device acquired at room temperature with laser frequency of $\omega = 900\ \mathrm{cm}^{-1}$. We use a color scheme that enables easy identification of the sign of the photocurrent: red and blue represent positive and negative currents respectively while white represents regions where the measured current is zero, thus highlighting the zero-crossing contours. Some of the zero-crossing contours form easily identifiable lines in the y-direction while others form a meandering pattern. On closer inspection, we find a series of fine structures in the photocurrent image that form a hexagonal lattice. These features are more clearly revealed in the map of the photocurrent gradient, dI_{PC}/dx, shown in Figure 4.1(D). The periodicity of these features is consistent with the domain walls observed in PFM images before encapsulation (Section 4.5.1). In the dI_{PC}/dx image, the vertical domain walls appear to be more intense because of the contact configuration used in our experiments, as explained in Section 4.5.3.1. The lattice structure and the matching periodicity lead us to conclude that the fine features correspond to the domain walls of a relaxed moiré superlattice in TBG.

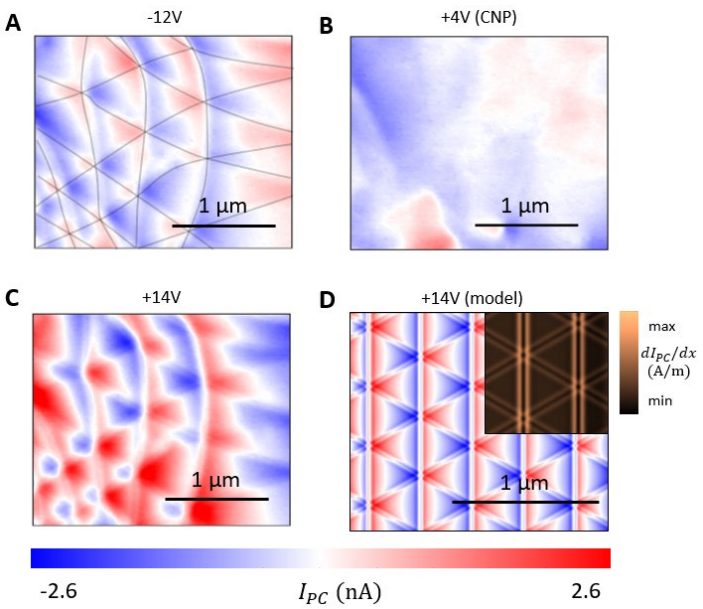

Figure 4.2 | Thermoelectric origin of the photocurrent in TBG. (A - C) Gate voltage dependence of the photocurrent (I_{PC}) at $\omega = 900\text{cm}^{-1}$ and $T = 300\text{K}$. Gate voltage is indicated above each panel. (D) Calculated photocurrent pattern using the Shockley-Ramo formalism (*59*) with material parameters corresponding to $V_G = +14\text{V}$ (more details in Section 4.5.3). The top-right inset shows the calculated image of dI_{PC}/dx (compare with Figure 4.1(D)).

Next, we study the gate dependence of the photocurrent maps as plotted in Figure 4.2(A - C). Transport experiments on our device showed that the charge neutrality point (CNP), where the carrier density is minimal and the majority carriers change from holes to electrons, occurs at $V_G = +4$ V (Section 4.5.1). Photocurrent imaging at the CNP (Fig 4.2(B)) does not show any of the features observed in Fig 4.1(C). A comparison of the images at $V_G = -12$ V (Fig 4.2(A)) and $V_G = +14$ V (Fig 4.2(C)) reveals that the photocurrent has identical meandering pattern and fine DW features for positive and negative gate voltages except for a sign change. These results show that the meandering patterns and the DW features are antisymmetric with respect to the carrier type.

As the gate voltage increases further in both the positive and negative direction, we find that the patterns weaken and eventually become unresolvable (Section 4.5.2). We note that the carrier densities in Figure 4.2 are too low to produce significant plasmonic effects in bilayer graphene (Section 4.5.1.2).

Previous theoretical (*58*) and experimental (*55*, *60*, *131*) investigations have discovered that the dominant mechanism for photocurrent generation in graphene is the photothermoelectric effect (PTE). In this mechanism, the absorption of incident light generates hot carriers in graphene. When the hot carriers encounter variations in the Seebeck coefficient, a thermoelectric voltage is generated which drives a current through the sample. The spatial profile of the measured current is therefore directly related to the Seebeck coefficient profile in the sample. PTE shows several characteristic features in experiments. First, since Seebeck coefficient is antisymmetric with respect to the sign of the carriers, the resulting photocurrent patterns also change sign when the carrier type changes from holes to electrons (*55*, *60*). Second, the Seebeck coefficient of bilayer graphene rapidly diminishes as the carrier density increases (*56*, *60*). Therefore, any variations in the Seebeck coefficient and the resulting photocurrent must also become small. Both features are present in our data, strongly suggesting that the photocurrent patterns we observe arise from PTE.

To confirm our hypothesis that the photocurrent arises from PTE and to gain a deeper understanding of our results, we calculated the expected photocurrent patterns from PTE. The input to these calculations are the Seebeck coefficient profile and the hot carrier temperature profile. We computed the former for an isolated domain wall using a generalized Boltzmann approach (Section 4.5.3) and the resulting profile is shown in Figure 4.1(B). To compare with our experiment, we superposed the one-dimensional Seebeck profiles in a hexagonal pattern to generate a two-dimensional lattice of domain walls (Section 4.5.3.4). Next, we computed the spatial

profile of the hot carriers. We first computed the electric field at the graphene surface using two different models for the tip (1) a "lightning-rod model" in which the tip is represented by a conducting hyperboloid and (2) a simplified common approximation of the tip by a vertically oriented point dipole (Sections 4.5.3.3 and 4.5.3.4). Since the conductivity of the graphene sheet is dominated by the in-plane components, we assumed that the radially symmetric in-plane field, E_r, governs the generation of hot carriers. We then solved the heat equation to determine the spatial profile of the hot carrier temperature (Section 4.5.3.1).

The Seebeck coefficient profile and the electron temperature profile are sufficient to calculate the local thermoelectric voltage for a given tip position. For gapless materials such as graphene, the photocurrent collected by distant electrodes also depends on the contact geometry. We used the Shockley-Ramo formalism of Ref (*59*) to include the effects of the contacts and our calculation procedures are described in more detail in Section 4.5.3.

The photocurrent pattern resulting from the hyperboloid tip calculation is shown in Figure 4.2(D). Our results reproduce the key features of our data including the meandering patterns and the fine features at the domain walls. We can now correlate the features in the photocurrent images with those in the Seebeck coefficient. The fine features and the zero-crossing contours that form straight lines along the y-axis arise from the domain walls themselves. On the other hand, the meandering zero-crossing contours go across domain walls, and arise from the interference of photocurrents generated by neighboring domain walls. The good agreement between calculations and data confirms that our photocurrent experiments directly probe the nanometer-scale Seebeck coefficient variations present at the domain walls.

While the first-principles Seebeck coefficient profile produced a photocurrent pattern similar to the experiment, we note that our experiment is not sensitive to the fine details of the

Seebeck coefficient at the domain wall. In fact, any change in Seebeck on a length scale significantly shorter than the spatial extent of the hot carriers (typically called the cooling length (*4*)) will produce a pattern similar to the experiment, as we demonstrate in Section 4.5.3.3.

4.3 Photocurrent imaging at frequencies within the Reststrahlen band of hBN

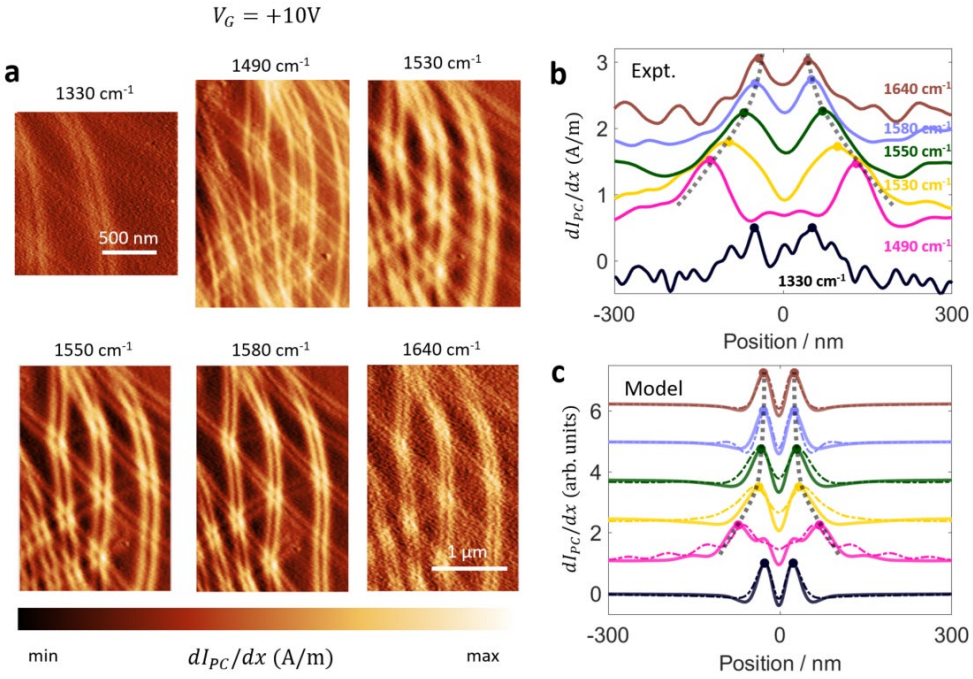

Figure 4.3 | Domain wall photocurrent patterns in the hBN Reststrahlen band. (A) Gradient of photocurrent (dI_{PC}/dx) for several frequencies around the hBN Reststrahlen band. (B) Experimental line profiles of dI_{PC}/dx for several frequencies. The black dashed lines are guides to the eye. (C) Photocurrent profiles calculated using the frequency dependent electric field profiles. The thick solid lines correspond to the hyperboloid tip and the thin dashed lines correspond to the point dipole model. The theoretical curves are normalized to their respective maxima. Curves in panel (B) and (C) are offset vertically for clarity.

So far, the hBN layers which surround the graphene sheet have not played an active role. We now show that the optical properties of hBN can be exploited to enhance the photocurrent features from the DWs. Over two frequency bands in the mid-infrared, referred to as the lower and upper Reststrahlen bands, the permittivity of hBN along its in-plane and out-of-plane principal axes have opposite signs (*132*). Such behavior, known as hyperbolicity, leads to highly confined phonon polaritons (*41*, *44*, *65*, *132*, *133*) and hyperlensing effects (*134*, *135*). Here, we specifically focus on the upper Reststrahlen band (1376 to 1614 cm^{-1}) where hBN transverse dielectric constant in the xy-plane becomes negative ($\epsilon_t < 0$). The out-of-plane dielectric constant remains positive ($\epsilon_z > 0$) and is weakly frequency dependent.

We performed photocurrent experiments at several frequencies around the upper Reststrahlen band and the data is shown in Figure 4.3(A). We observe a clear change in the width of the domain wall feature with frequency. Specifically, we find that at the lower end of the Reststrahlen band (e.g., $\omega = 1490\ \mathrm{cm}^{-1}$ and $\omega = 1530\ \mathrm{cm}^{-1}$ in Fig. 4.3(A)) the domain wall feature is wider compared with pattern below the reststrahlen band (compare, for example, with $\omega = 900\ \mathrm{cm}^{-1}$ of Figure 4.1(D)). As the frequency increases, the width of the broad features decreases. Finally, at frequencies above the Reststrahlen band ($\omega = 1640\ \mathrm{cm}^{-1}$ in Fig. 4.3(A)), the width of the feature returns to its value below the Reststrahlen band. Furthermore, at $\omega = 1490\mathrm{cm}^{-1}$ we observe two faint peaks in between the two stronger peaks. These effects are further confirmed by the frequency-dependent line profiles shown in Fig 4.3(B). From the line profiles, we see that the fainter peaks at $\omega = 1490\mathrm{cm}^{-1}$ are approximately coincident with the original peaks at $\omega = 1330\mathrm{cm}^{-1}$ and $1640\mathrm{cm}^{-1}$.

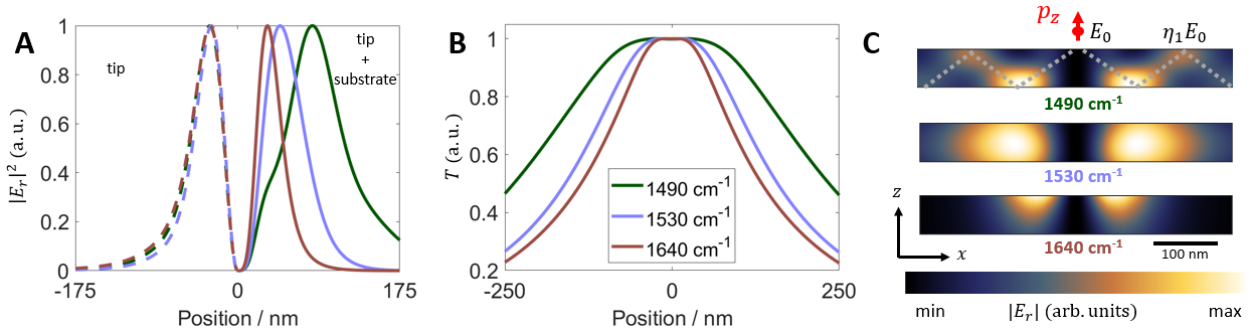

Figure 4.4 | Local electric field and temperature inside and outside the Reststrahlen band. (A) In-plane electric field $|E_r|^2$ at the graphene layer calculated for a hyperboloid tip. The left half (dashed lines) shows the field of the tip alone and the right half (solid lines) shows the total field from the tip and the substrate. (B) Hot carrier temperature T calculated using the total field from (A). (C) Cross section of a hBN slab showing the electric field resulting from excitation by a point dipole located above the hBN surface. 1490 cm^{-1} and 1530 cm^{-1} are inside and 1640 cm^{-1} is outside the Reststrahlen band, respectively. The dashed line in the 1490 cm^{-1} image shows the polariton propagation. E_0 and $\eta_1 E_0$ represent the magnitude of the in-plane field at the zeroth order and the first order maxima respectively.

Since our experiments at $\omega = 900$ cm^{-1} and the related modelling have shown that the photocurrent pattern is of PTE origin, any change in the pattern must be due to either a change in the Seebeck coefficient profile or the hot carrier profile. The Seebeck coefficient is not expected to change with the frequency of light incident on the material in the linear regime and the laser power used in our experiment (~20mW, see Section 4.5.1) is too weak to produce a significant non-linear effect. Therefore, we are led to conclude that change in the hot carrier distribution must be responsible for the observed change in width.

The spatial profile of Joule heating power is determined by the electric field profile under the tip and the real part of the optical conductivity of bilayer graphene, $\mathrm{Re}(\sigma)$. The frequency dependence data of Figure 4.3 was collected at $V_G = +10\mathrm{V}$, where the estimated Fermi energy in the Bernal stacked regions is low ($E_F \approx 10\mathrm{meV}$, refer to Section 4.5.1.2) and the optical conductivity is dominated by the frequency-independent interband conductivity (*136*, *137*). Therefore, we conclude that the electric field profile under the tip must change with frequency within the Reststrahlen band in order to reproduce the experimental observations shown in Figure 4.3. To model the observed change in width, we used the "lightning rod" model and a point dipole model to compute the radial electric field at several frequencies around the Reststrahlen band (Sections 4.5.3.3 and 4.5.3.4). The photocurrent profiles from our modeling are shown in Figure 4.3(C) and show good agreement with the experiment.

The electric field at the graphene layer can be thought of as the sum of two separate parts. The first part is the incident field from the tip and the second part is the field reflected by the hBN substrate in response to the tip excitation. The left panels in Figure 4.4(A) show the tip field and the right panels show the total field. We see that the tip field is weakly dependent on the frequency but the field reflected by the substrate is strongly modified inside the Reststrahlen band. The wider electric field leads to a wider hot carrier temperature profile (Figure 4.4(B)) and a broader photocurrent pattern (Figure 4.3(C)).

The origin of this widening is closely related to a previously observed effect in hBN slabs, known as hyperlensing (*102*, *134*, *135*). In hyperlensing, a sub-wavelength antenna launches phonon polariton rays that propagate inside the hBN slab. Here, our tip acts as the antenna. The total in-plane field at the hBN surface can be thought of as a series of concentric rings centered below the tip with a radius of r_k^{max} for the k-th ring. The electric field at the k-th ring is given by

$E_k = \eta_k E_0$, where η_k is related to the permittivity of the hBN slab and the substrate (Section 4.5.3.4). The $k = 0$ ring corresponds to the field from the tip itself with magnitude E_0 while $k = 1, 2, \ldots$ correspond to phonon polaritons propagating in the hBN slab (see Fig 4.4(C) and Section 4.5.3.4). Therefore, inside the Reststrahlen band, the zeroth order maximum is frequency independent but the higher order maxima are strongly frequency dependent.

Typically, the magnitude of the field at the $k = 1$ ring is expected to be smaller than the field created directly by the tip ($|\eta_1| < 1$). However, for several frequencies inside the Reststrahlen band, $|\eta_1| > 1$, so E_1 dominates and leads to a broad frequency-dependent electric field profile and photocurrent pattern. The faint central features in dI_{PC}/dx at $\omega = 1490\text{cm}^{-1}$ can now be understood as arising from E_0 while the stronger broader features arise from E_1. In principle, the polariton reflections corresponding to E_2 and higher order terms should be reflected in the photocurrent profile. Our simulations suggest that a sharper tip and more widely separated domain walls (i.e., smaller twist angle) could reveal such features in future photocurrent experiments (Section 4.5.3.4).

4.4 Conclusion

In conclusion, we have demonstrated that nano-photocurrent experiments are sensitive to nanoscale changes in the Seebeck coefficient at the domain walls in MTBG. Our modeling of the photocurrent patterns is consistent with experiment. We further demonstrate a hyperbolic optoelectronic effect where the domain wall photocurrent patterns are enhanced by the hyperbolicity of the hBN substrate.

4.5 Supplementary Material

4.5.1 Materials and Methods

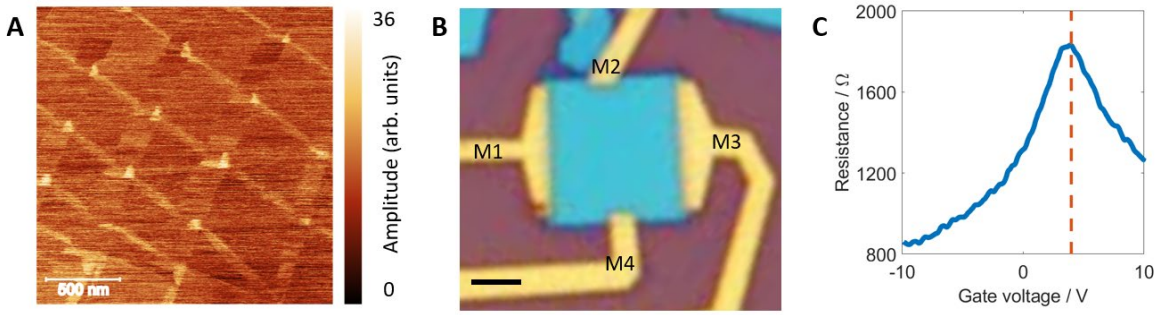

Figure 4.5 | Device fabrication. (A) Piezoresponse force microscopy image of the graphene layers before encapsulation showing domain walls. (B) Optical microscope image showing the final contact configuration. Scale bar 3μm. (C) Two probe resistance measured using M1 and M3 contacts as a function of V_G applied to the Si back gate. The dashed line corresponds to $V_G = +4\text{V}$ which is taken to be the charge neutrality point (Figure 4.2(A)).

The minimally twisted bilayer graphene device was fabricated using the dry transfer method. Piezoresponse force microscopy (PFM) (*130*) was performed before encapsulation to ensure that a moiré pattern with a large periodicity was present, as shown in Figure 4.5(A). The contact geometry was specifically designed for easy interpretation of photocurrent experiments (Figure 4.5(B)). We used the M1-M3 contacts for all photocurrent experiments.

The properties of bilayer graphene depend not only on the carrier density but also on the interlayer bias. In our experiment, we have a single Si back gate which allows us to control the carrier density accurately. Here, we describe our estimate of the interlayer bias values for different gate voltages. First, we assume that the interlayer bias is zero at charge neutrality point $V_G = +4\text{V}$.

This assumption is reasonable for the ultra-high quality, doubly-encapsulated devices studied in this work (*138*).

For a given gate voltage, we can directly calculate the displacement field below the graphene layers:

$$D_{lower} = \frac{\epsilon_{lower} V_G}{d_{lower}}$$

where ϵ_{lower} and d_{lower} are the dielectric constant and thickness of the SiO_2 dielectric layer. Because we have no top gate, the displacement field above the graphene layers $D_{upper} = 0$ and effective displacement field across the graphene is given by:

$$\overline{D} = \frac{D_{upper} + D_{lower}}{2} = \frac{D_{lower}}{2}.$$

We use Ref (*10*) to estimate the interlayer bias V_i from $\overline{D}$. To estimate E_F, we keep V_i fixed and vary the Fermi energy E_F until the carrier density we calculate with a tight-binding model matches the value expected from capacitance calculations. Figure 4.6 shows a plot of the estimated E_F and V_i for several gate voltages. We find that the estimated Fermi energy is linear with gate voltage. At small displacement fields, the band structure of bilayer graphene can be well approximated to be parabolic (*8*). In 2 dimensions, a parabolic dispersion leads to a constant density of states and a linear dependence of the Fermi energy on carrier density, which is consistent with our estimate. We note that the carrier densities considered in this manuscript (Figures 2 and 3) are too low to produce significant plasmonic effects. In bilayer graphene, plasmons are typically observed in nano-infrared imaging for $V_G - V_{CNP} > \sim 30\text{V}$ (*71*).

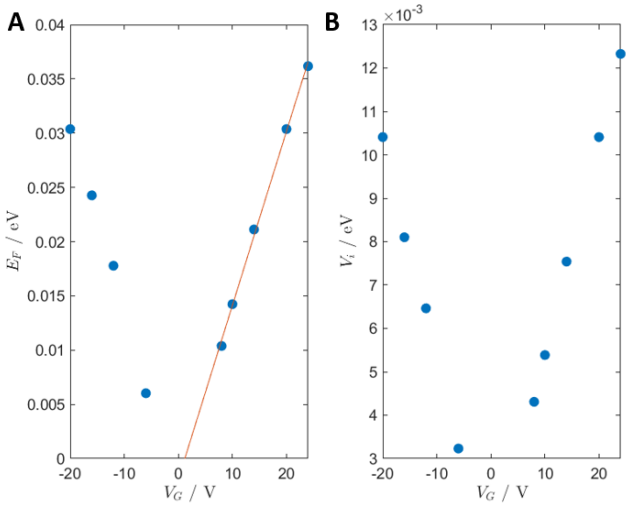

Figure 4.6 | Estimated Fermi energy and interlayer bias for bilayer graphene with a single gate. The dots correspond to specific gate voltages and the red line is a linear fit.

4.5.2 More photocurrent data

Here, we describe our analysis methods for the photocurrent data and include all of the collected images. The photocurrent signal was demodulated at a harmonic of the tip tapping frequency with a lock-in amplifier. The phase offset of the demodulation signal is arbitrary since the phase only determines the direction of the current and otherwise does not contain any meaningful information. Therefore, for each photocurrent image, we adjusted the phase offset so as to maximize the signal in the in-phase component and minimize it in the out-of-phase component. Stated more rigorously, $S_{in}(x,y), S_{out}(x,y)$ are the raw data images for in-phase and out-of-phase lock-in output channels. For an offset phase ϕ_0, the corrected signal $S'_{in}(x,y), S'_{out}(x,y)$ is the result of rotation by ϕ_0:

$$\begin{pmatrix} S'_{in} \\ S'_{out} \end{pmatrix} = \begin{pmatrix} \cos\phi_0 & \sin\phi_0 \\ -\sin\phi_0 & \cos\phi_0 \end{pmatrix} \begin{pmatrix} S_{in} \\ S_{out} \end{pmatrix}$$

The offset angle ϕ_0 is chosen as to minimize the variance of S'_{out} across the image.

4.5.2.1 $\omega = 900\ cm^{-1}$

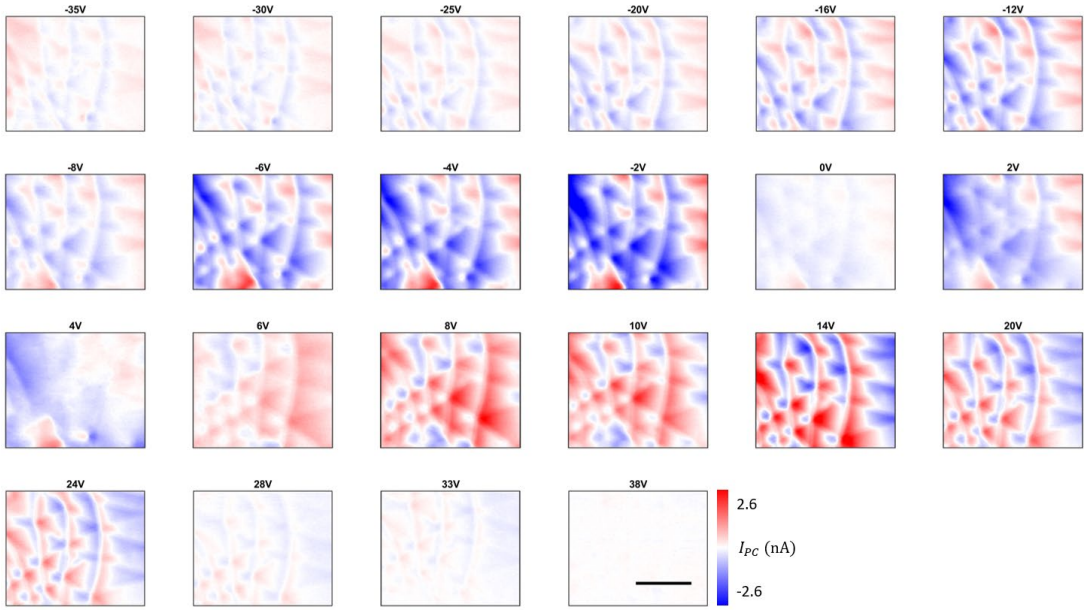

Figure 4.7 | Photocurrent data for several gate voltages at $\omega = 900\text{cm}^{-1}$. Scale bar 1μm.

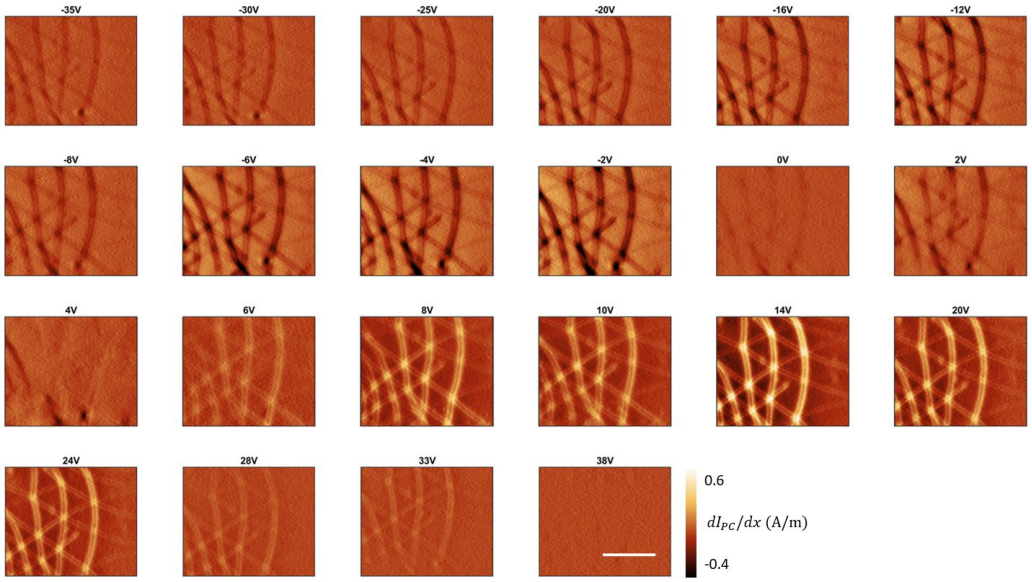

Figure 4.8 | Photocurrent gradient for several gate voltages at $\omega = 900\text{cm}^{-1}$. Scale bar 1μm.

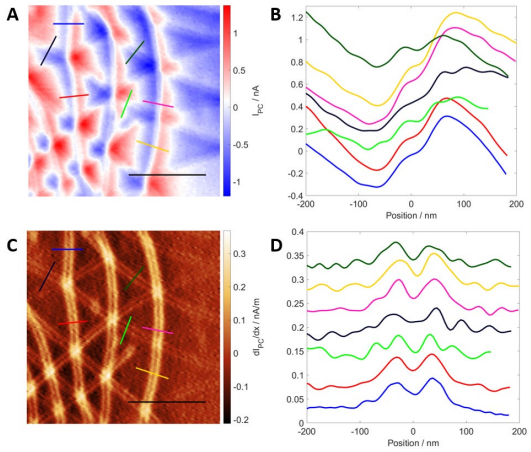

Figure 4.9 | Photocurrent line profiles at $V_G = +24$V. (A) Nano-photocurrent image at $V_G = +24$V (same as Figure 4.1(B)). (B) Multiple line profiles across the domain walls. Each profile is offset by an arbitrary number for clarity. (C) and (D) same as (A) and (B) but for dI_{PC}/dx.

4.5.2.2 Frequencies in the Reststrahlen band of hBN

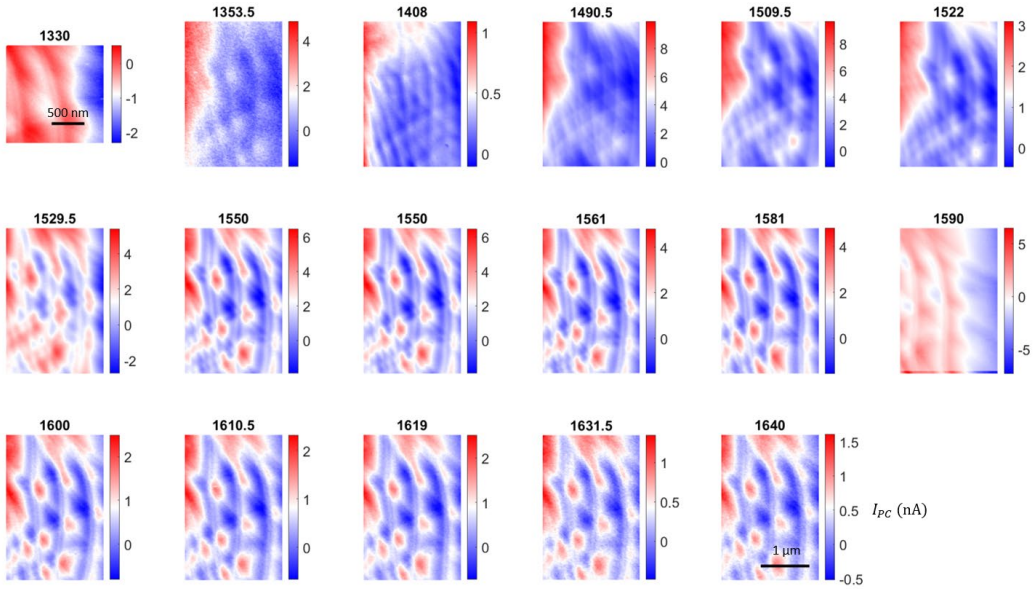

Figure 4.10 | Frequency dependent photocurrent images in the hBN reststrahlen band.

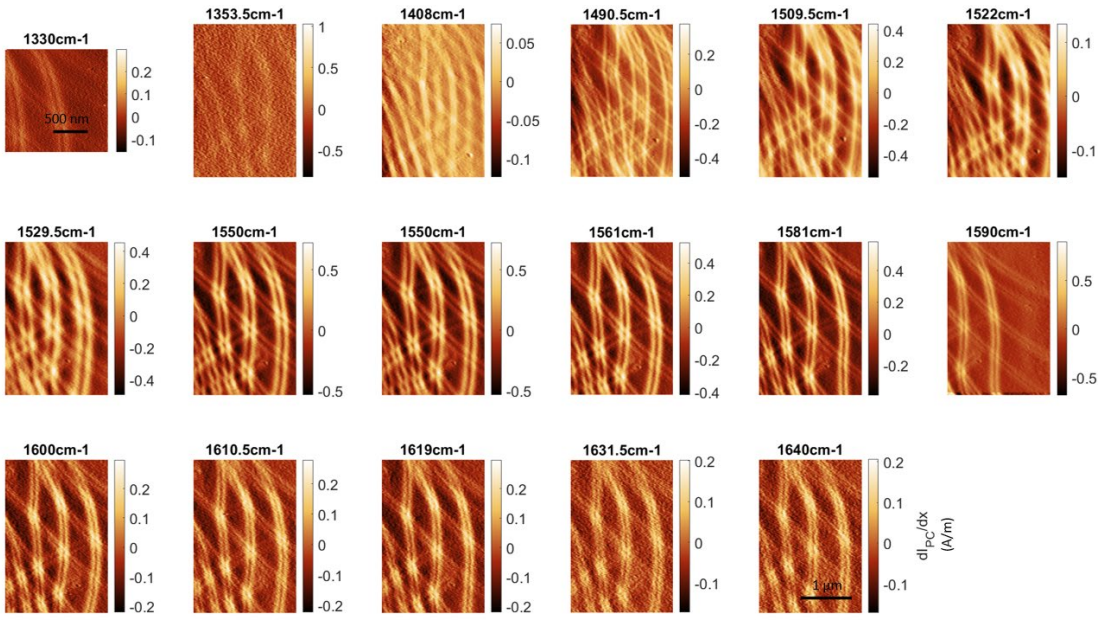

Figure 4.11 | Frequency dependent dI_{PC}/dx images in the hBN reststrahlen band.

4.5.3 Photocurrent model

4.5.3.1 Photocurrent calculation

In gapless materials such as graphene, the spatial photocurrent profiles are described by the Shockley-Ramo formalism (*59*). In this formalism, an auxiliary potential ϕ is defined as solution of Laplace's equation, $\nabla \cdot (\sigma^T \nabla \phi) = 0$ (σ is the dc conductivity tensor) with the contact configuration dependent boundary conditions: $\phi = 1$ at current collecting contacts (where the current is being measured) and $\phi = 0$ at the rest of the grounded contacts. According to the Shockley-Ramo formalism, one can show that the measured photocurrent would then be:

$$I_{PC} = \iint d^2\boldsymbol{r}' \boldsymbol{J}_{local}(\boldsymbol{r}') \cdot \nabla\phi(\boldsymbol{r}')$$

Where $\boldsymbol{J}_{local}$ is the locally generated photocurrent density. In our case the photocurrent is generated through the photothermoelectric effect, and for a tip positioned at a point $\boldsymbol{r}$ would therefore yield the following photocurrent reading:

$$I_{PC}(\boldsymbol{r}) = \iint d^2\boldsymbol{r}'\, \sigma(\boldsymbol{r}')\, S(\boldsymbol{r}')\, \nabla T(\boldsymbol{r}', \boldsymbol{r}) \cdot \nabla \phi(\boldsymbol{r}')$$

where $T(\boldsymbol{r}', \boldsymbol{r})$ is the temperature at $\boldsymbol{r}'$ as a result of a tip located at $\boldsymbol{r}$ and S is the Seebeck coefficient tensor.

Since we are interested in a 1D domain wall, we can simplify the problem with a quasi-1D geometry. We assume that the sample is infinite in the y direction, both σ and S are independent of y, and we have a grounded contact at $x = 0$ and a collecting contact at $x = L$. We further assume that S is diagonal and isotropic. These assumptions yield: $\phi(x) = \int_0^x dx' \frac{1}{\sigma(x')} / \int_0^L dx' \frac{1}{\sigma(x')}$. After substitution into the photocurrent expression we get:

$$I_{PC}(\boldsymbol{r}) = \frac{\Sigma}{L} \iint d^2\boldsymbol{r}'\, S(\boldsymbol{r}') \frac{\partial T(\boldsymbol{r}', \boldsymbol{r})}{\partial x}$$

Where $\Sigma \equiv L \left(\int_0^L dx' \frac{1}{\sigma_{xx}(x')} \right)^{-1}$. Finally, we assume the shape of the temperature profile to be independent of tip position, such that: $T(\boldsymbol{r}', \boldsymbol{r}) = T(\boldsymbol{r}' - \boldsymbol{r})$. This assumption is justified if the absorption and thermal properties are not strongly modulated as a function of position. The last assumption formulates the above expression for the measured photocurrent as a 2D convolution of two terms such that:

$$I_{PC}(\boldsymbol{r}) = \frac{\Sigma}{L} \left(S * \frac{\partial T}{\partial x} \right)(\boldsymbol{r}) \qquad \text{(Eq 4.1)}$$

The remaining task in order to calculate the photocurrent is to calculate the temperature spatial profile, $T(\boldsymbol{r})$. We describe it by the diffusion equation:

$$-\kappa \nabla^2 \tau(\boldsymbol{r}) + g\tau(\boldsymbol{r}) = P(\boldsymbol{r}) \qquad \text{(Eq 4.2)}$$

where $\tau = T - T_0$ is the electronic temperature change relative to a background thermal bath at T_0, κ is the in-plane thermal conductivity of graphene, g is the out-of-plane thermal coupling to the substrate (both assumed to be spatially uniform for simplicity) and P is the

absorbed heat distribution (which is estimate in this study using the lightning rod model as described in Section 4.5.3.3). Following (*4*), the general solution can be obtained by a Green's function approach, where we first solve for the Green's function G that satisfies the impulse response equation:

$$-\kappa\nabla^2 G(\boldsymbol{r}) + gG(\boldsymbol{r}) = \delta^{(2)}(\boldsymbol{r})$$

Where $\delta^{(2)}(\boldsymbol{r})$ is the 2D delta function. The general solution to Eq 4.2 for an arbitrary $P(\boldsymbol{r})$ is then given by the convolution $\tau = G * P$. We can solve for the Green's function through a Fourier analysis. We define $\tilde{G}(k_x, k_y) = \int_{-\infty}^{\infty} dx \int_{-\infty}^{\infty} dy\, G(x,y) e^{-i(k_x x + k_y y)}$ to be the Fourier transform of $G(x,y)$. One can then show that:

$$\tilde{G}(k_x, k_y) = \frac{1}{4\pi^2} \frac{1}{g + \kappa(k_x^2 + k_y^2)}$$

Taking the inverse Fourier transform gives us the Green's function

$$G(\boldsymbol{r}) = K_0\left(\frac{r}{\sqrt{\kappa/g}}\right)$$

where $K_0(x)$ is the 0th order modified Bessel function of the second kind and $l_{cool} = \sqrt{\kappa/g}$ is a thermal length-scale which is typically called the cooling length. In our simulations, we used $l_{cool} = 100\text{nm}$ for the room temperature $\omega = 900\text{cm}^{-1}$ data (Fig 4.2(D)) and $l_{cool} = 200\text{nm}$ for the $T = 200\text{K}$ data in the hBN Reststrahlen band (Figure 4.3(C) and 4.3(B)).

Assuming the graphene sheet thermal conductivity of $\kappa \sim 10^{-6}$ W/K (*139*) and a room temperature cooling length of $l_{cool} = 100$ nm, the interfacial thermal resistance in our samples is about $R_T = 1/g = l_{cool}^2/\kappa \sim 10^{-8}$ m^{2}K/W, comparable to theoretically predicted (*140*) and experimentally measured (*141*) values. Note that this parameter appears to strongly depend on the interface and sample quality. In a previous photocurrent experiment (*142*), this thermal resistance was estimated to be as high as 10^{-5} m^{2}K/W.

The Shockley-Ramo formalism also provides an explanation for the asymmetry between the domain wall dI_{PC}/dx profiles along different directions in Figure 4.1. The profiles along the y-direction are significantly stronger because of the $\partial T/\partial x$ term in Eq 4.1. The domain walls along the other directions contribute less to the convolution in Eq 4.1 and therefore appear weaker in the experiment. This behavior is captured directly in Fig 4.2(D).

4.5.3.2 First principles calculations of Seebeck coefficient across the domain wall

We will analyze the static transport properties across a single AB/BA domain wall. The Hamiltonian is adopted from (*34*) where the optical properties across a single domain wall were discussed i.e., we consider the general Hamiltonian of bilayer graphene

$$H = \begin{pmatrix} H_0 & U^{\dagger} \\ U & H_0 \end{pmatrix}, U = \begin{pmatrix} U_{AA} & U_{AB} \\ U_{BA} & U_{BB} \end{pmatrix},$$

where $H_0 = \hbar v_F \sigma \cdot \boldsymbol{k}$ denotes the Hamiltonian of a single layer graphene and U the interlayer coupling with $U_{AA} = U_{BB} = \frac{t_1}{3}\left[1 + 2\cos\left(\frac{2\pi}{3}\frac{\delta}{a_0}\right)\right], U_{AB} = \frac{t_1}{3}\left[1 + 2\cos\left(\frac{2\pi}{3}\left(\frac{\delta}{a_0} + 1\right)\right)\right], U_{BA} = \frac{t_1}{3}\left[1 + 2\cos\left(\frac{2\pi}{3}\left(\frac{\delta}{a_0} - 1\right)\right)\right]$ (*143*). A single AB-BA domain wall at $x = 0$ with width w is then modeled by the displacement field $\delta(x) = \frac{2}{\pi}\arctan\left[\exp\left(\frac{\pi x}{w}\right)\right] + 1$. For numerical convenience, we add another, independent, single BA/AB domain wall in order to implement periodic boundary conditions.

The particle current and heat-flow due to electrons is given by (*144*)

$$\begin{pmatrix} \vec{J} \\ \vec{U} \end{pmatrix} = \begin{pmatrix} \mathbf{K_0} & \mathbf{K_1} \\ \mathbf{K_1} & \mathbf{K_2} \end{pmatrix} \begin{pmatrix} e\vec{\nabla}\phi \\ T^{-1}\vec{\nabla}T \end{pmatrix} \qquad \text{(Eq 4.3)}$$

where the tensors $\mathbf{K}_{\boldsymbol{l}}$ with $l = 0, 1, 2$ read

$$\mathbf{K}_l = \frac{g_s g_v}{A} \sum_{\boldsymbol{k},n} \vec{v}_{\boldsymbol{k},n}\, \vec{v}_{\boldsymbol{k},n}^{T} \tau_{\boldsymbol{k},n} \left(\epsilon_{\boldsymbol{k},n} - \mu\right)^{l} \left(-\frac{\partial f^0_{\boldsymbol{k},n}}{\partial \epsilon_{\boldsymbol{k},n}}\right).$$

These quantities depend on the relaxation time $\tau_{\boldsymbol{k},n}$ and $\vec{v}_{\boldsymbol{k},n} = \langle \boldsymbol{k}, n | \hat{\vec{v}} | \boldsymbol{k}, n \rangle$ where $\epsilon_{\boldsymbol{k},n}$ and $|\boldsymbol{k}, n\rangle$ denote the eigenvalues and eigenvectors of the underlying Hamiltonian, respectively with $\boldsymbol{k}$ inside the first Brillouin zone. Furthermore, $f^0_{\boldsymbol{k},n}$ denotes the Fermi-Dirac distribution function at chemical potential μ, A denotes the area of the sample, $g_s = g_v = 2$ the spin and valley degeneracy, and $\hat{\vec{v}}$ is the velocity operator. Typical transport properties such as the dc conductivity, the Seebeck coefficient and the thermal conductivity are then defined by $\sigma_{dc} = e^2 \mathbf{K}_0$, $S = -(eT)^{-1} \mathbf{K}_0^{-1} \mathbf{K}_1$, and $\kappa = T^{-1}(\mathbf{K}_2 - \mathbf{K}_1 \mathbf{K}_0^{-1} \mathbf{K}_1)$.

Eq 4.3 can be generalized to define the local current response i.e., $\mathcal{J}(\vec{r}) = \int d\vec{r}\,' \mathcal{K}(\vec{r}, \vec{r}\,') \nabla\chi(\vec{r}\,')$ with $\mathcal{J}(\vec{r}) = \left(\vec{J}(\vec{r}), \vec{U}(\vec{r})\right)^T$ and the corresponding definitions for $\mathcal{K}(\vec{r}, \vec{r}\,')$ and $\chi(\vec{r})$. We then applied the local approximation (*145*) which amounts to $\mathcal{K}_{loc}(\vec{r}) = \int d\vec{r}\,' \mathcal{K}(\vec{r}, \vec{r}\,')$ and obtained the local transport quantities such as the Seebeck coefficient that were discussed earlier in the chapter.

4.5.3.3 Electric field profiles using the lightning rod model

The electric field relevant for calculating a temperature profile at the graphene layer is computed using the lightning rod of probe-sample near-field interaction (*35*). Here the near-field probe is considered as an ideally conducting metallic hyperboloid (roughly conical in shape) 19 microns in height with a taper angle of about 20 degrees to the probe axis, and a curvature radius of 75 nm at its apex. For a chosen sample configuration comprising a multi-layer stack (here a 7 nm top hBN layer, nearly charge-neutral graphene bilayer atop a 36 nm hBN slab over an SiO_2

substrate), a specified probe-sample distance d, and illumination energy, the model predicts the axisymmetric charge distribution $\lambda(z) \equiv dQ/dz$ along the probe. For the ideally conducting probe, this charge conforms to the external profile of the probe in a quasi-continuum of rings of radius $\mathcal{R}(z)$, where z denotes the probe's axial coordinate. From $\lambda(z)$, we evaluate the electric near-field from the probe in the graphene plane using the angular spectrum representation:

$$\boldsymbol{E_{probe}}(\rho, d) = \int_0^L dz\, \lambda(z) \int dq\, q\, [J_0(q\rho)\hat{z} + J_1(q\rho)\hat{\rho}]\, J_0(q\mathcal{R}(z)) e^{-q(d+z)}$$

Here ρ denotes the in-plane radial coordinate from the probe axis, q is a Fourier momentum. As an integral sum of Bessel functions $J_1(q\rho)$, the radial field $E_{\rho,probe}$ presents a roughly "donut"-shaped in-plane distribution as shown in Fig. 4.4. The total field inclusive of fields reflected from the sample is then given similarly by:

$$\boldsymbol{E_{total}}(\rho, d) = \int_0^L dz\, \lambda(z) \int dq\, q \begin{bmatrix} \big(1 + r_p(q)\big) J_0(q\rho)\hat{z} + \\ \big(1 - r_p(q)\big) J_1(q\rho)\hat{\rho} \end{bmatrix} J_0(q\mathcal{R}(z)) e^{-q(d+z)}$$

Here $r_p(q)$ denotes the momentum-resolved Fresnel reflection coefficient for p-polarized fields computed for our heterostructure with a transfer matrix method.

We now turn our attention to the electric fields associated with generating the temperature profile relevant for the PTE underlying our photocurrent imaging. Since photocurrents were obtained at the $n = 2, 3$ harmonics of the probe tapping frequency Ω, the spatially-resolved distribution of thermal power deposited in the graphene at these harmonics is given by:

$$P_n(\rho) \approx \mathrm{Re}(\sigma) \left|E_{\rho,n}\right|^2$$

Here σ represents the optical conductivity of graphene and $E_{\rho,n}$ denotes the radially polarized total field demodulated at harmonic n:

$$E_{\rho,n}(\rho) \equiv \frac{\Omega}{\pi} \int_0^{2\pi/\Omega} dt\, \cos n\Omega t \cdot E_\rho(\rho, d = \cos \Omega t)$$

Since the lightning rod model predicts a physically meaningful electric field profile for all probe-sample distances d, the power distribution $P_n(\rho)$ for $n = 2,3$ was straightforwardly calculated with the relevant products of demodulated field distributions $E_{\rho,n}(\rho)$ inclusive of reflected fields from the sample.

Figure 4.12 shows the field and temperature profiles for several frequencies. We note that the dT/dx profile is qualitatively similar to our observed photocurrent pattern. Let's say, the Seebeck profile is narrow compared to the dT/dx such that it can be approximated as a delta function. Then, from Eq 4.1, we see that the photocurrent profile will be identical to dT/dx. Therefore, we conclude that any Seebeck coefficient profile that is significantly narrower than the cooling length will produce a photocurrent pattern that is consistent with our experimental data.

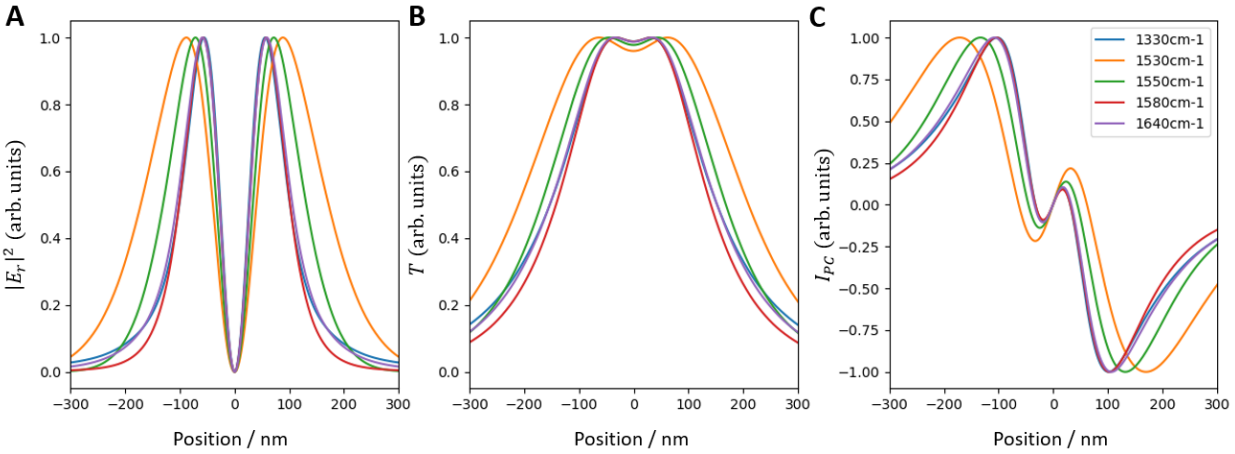

Figure 4.12 | Electric field and temperature profiles. (A - C) Radial electric field E_r, hot carrier temperature T and $dT/dx = \hat{x} \cdot \nabla T$ profiles at various frequencies. The tip is located at the origin.

4.5.5 Converting 1D profiles to 2D profiles – superposition model

To convert the 1D profiles calculated in Section 4.5.3.2 into 2D profiles, we used a simple superposition model. However, the superposition model may not accurately reproduce the Seebeck profile at the AA sites. Here, we compare the relative importance of the domain walls and the AA sites to the calculated photocurrent pattern by separating their relative contributions.

First, we define a mask which is a series of Gaussians centered on the AA sites. Let the n AA sites be located at $\{x_n, y_n\}$. Then, the mask is given by

$$M(x,y) = \sum_n \exp\left(-\frac{(x-x_n)^2 + (y-y_n)^2}{w_{AA}^2}\right)$$

where w_{AA} is the width of the Gaussians. Then we separate the Seebeck coefficient at the AA sites by multiplying the Seebeck coefficient from the superposition model by the mask:

$$S_{AA}(x,y) = S_{2D}(x,y)M(x,y)$$

The domain wall contribution is then

$$S_{DW}(x,y) = S_{2D}(x,y)(1 - M(x,y))$$

such that

$$S_{AA}(x,y) + S_{DW}(x,y) = S_{2D}(x,y)$$

Furthermore, since convolution is linear, the following is also true:

$$I_{PC,AA} + I_{PC,DW} = I_{PC}$$

where $I_{PC,AA}$, $I_{PC,DW}$ and I_{PC} are the photocurrent patterns arising from S_{AA}, S_{DW} and S_{2D} respectively.

Figure 4.20 shows the Seebeck coefficient and photocurrent patterns arising from the profiles calculated above. We see that $I_{PC,AA}$ is simply a series of dipoles centered at the AA sites and does not resemble the pattern observed in the experiment. At the same time, $I_{PC,DW}$ reproduces both the meandering pattern as well as the fine features at the domain walls. The spatial patterns

in the sum I_{PC} are only slight modifications to $I_{PC,DW}$. Therefore, we conclude that the 1D Seebeck coefficient variation across the domain wall is dominant in explaining the observed experimental pattern, thus justifying the use of the superposition model.

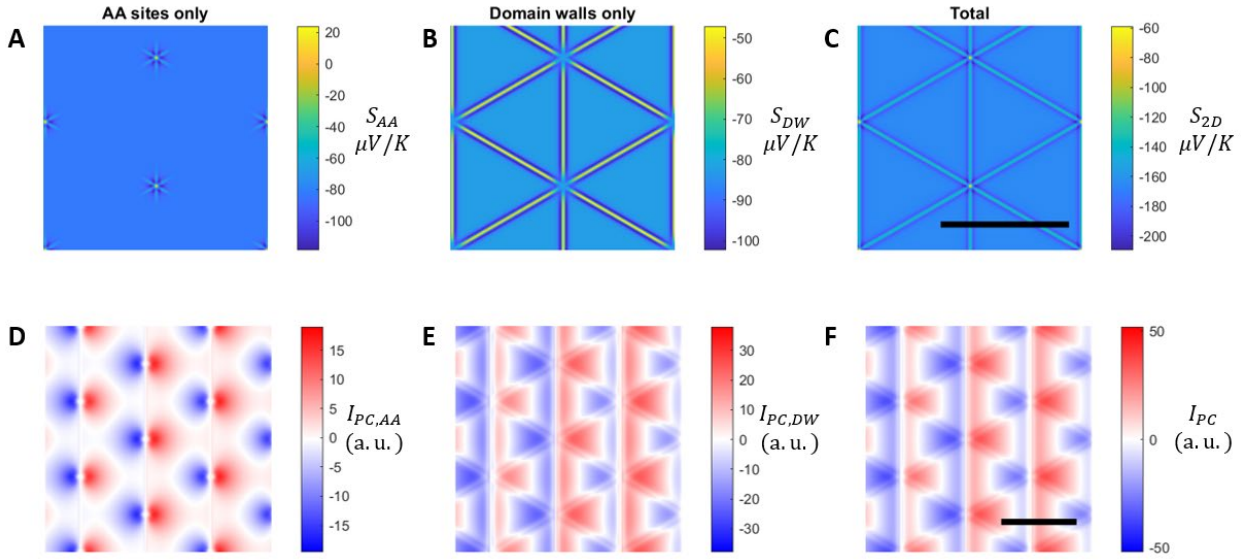

Figure 4.20 | Relative importance of the AA sites and the domain walls to the calculated photocurrent pattern. (A) Seebeck coefficient of the AA sites only S_{AA} (B) Seebeck coefficient of the domain walls only S_{DW} (C) Total Seebeck coefficient calculated with the superposition model S_{2D}. (D – F) Calculated photocurrent patterns for the Seebeck coefficients in (A – C). Scale bars 500nm.

Chapter 5: Nano-optics compatible top gates

5.1 Introduction

Graphene-based heterostructures display a variety of phenomena that are strongly tunable by electrostatic local gates. Monolayer graphene (MLG) exhibits tunable surface plasmon polaritons, as revealed by scanning nano-infrared experiments. In bilayer graphene (BLG), an electronic gap is induced by a perpendicular displacement field. Gapped BLG is predicted to display unusual effects such as plasmon amplification and domain wall plasmons with significantly larger lifetime than MLG. Furthermore, a variety of correlated electronic phases highly sensitive to displacement fields have been observed in twisted graphene structures. However, applying perpendicular displacement fields in nano-infrared experiments has only recently become possible (1). In this work, we fully characterize two approaches to realizing nano-optics compatible top-gates: bilayer MoS_2 and MLG. We perform nano-infrared imaging on both types of structures and evaluate their strengths and weaknesses. Our work paves the way for comprehensive near-field experiments of correlated phenomena and plasmonic effects in graphene-based heterostructures.

Graphene-based van der Waals (vdW) heterostructures display a variety of phenomena including superior plasmonic properties (*38*, *48*, *49*, *65*), tunable band structures (*13*, *14*, *88*), topological edge states (*27*, *28*, *32*), and correlated phases such as superconductivity (*18*, *19*). This large variety of electronic phases arises because the properties of graphene are strongly tunable by electrostatic gates. The optical excitations corresponding to these phases lie in the infrared range of the electromagnetic spectrum (*7*), where the wavelength of light, λ_0, ranges from 1μm to 100μm. Probing such heterostructures with conventional far-field optical experiments is challenging because of their limited lateral dimensions compared to λ_0. However, tip-based scanning nano-

infrared experiments can overcome the diffraction limit and achieve a spatial resolution better than 10nm (*37*).

Nano-infrared experiments have established monolayer graphene (MLG) as an excellent platform for plasmonics because of a large confinement ratio λ_0/λ_p (λ_p is the plasmon wavelength) (*44*, *45*, *65*), tunability with an external gate (*48*, *49*) and long lifetimes for the SPPs approaching 2 ps (*38*, *47*). While MLG is well studied, the plasmonic properties of bilayer graphene are relatively unexplored (*71*). When bilayer graphene is gapped and the Fermi level lies in the gap, exotic plasmonic phenomena are predicted to occur. Gapped BLG under photoexcitation is predicted to amplify SPPs (*146*) while domain wall solitons in gapped BLG could host one-dimensional SPPs with lifetimes approaching 10^2 ps (*50*).

Nano-infrared experiments have also begun to probe multilayer graphene-based Moiré systems that are known to host correlated electronic phenomena such as twisted bilayer graphene (TBG) (*18*), twisted trilayer graphene (TTG) (*147*) and twisted double bilayer graphene (TDBG) (*148*, *149*). The electronic properties of all these systems are strongly sensitive to perpendicular displacement field. For example, the correlated insulator phases in TTG and TDBG appear only for a limited range of displacement fields (*147*, *148*).

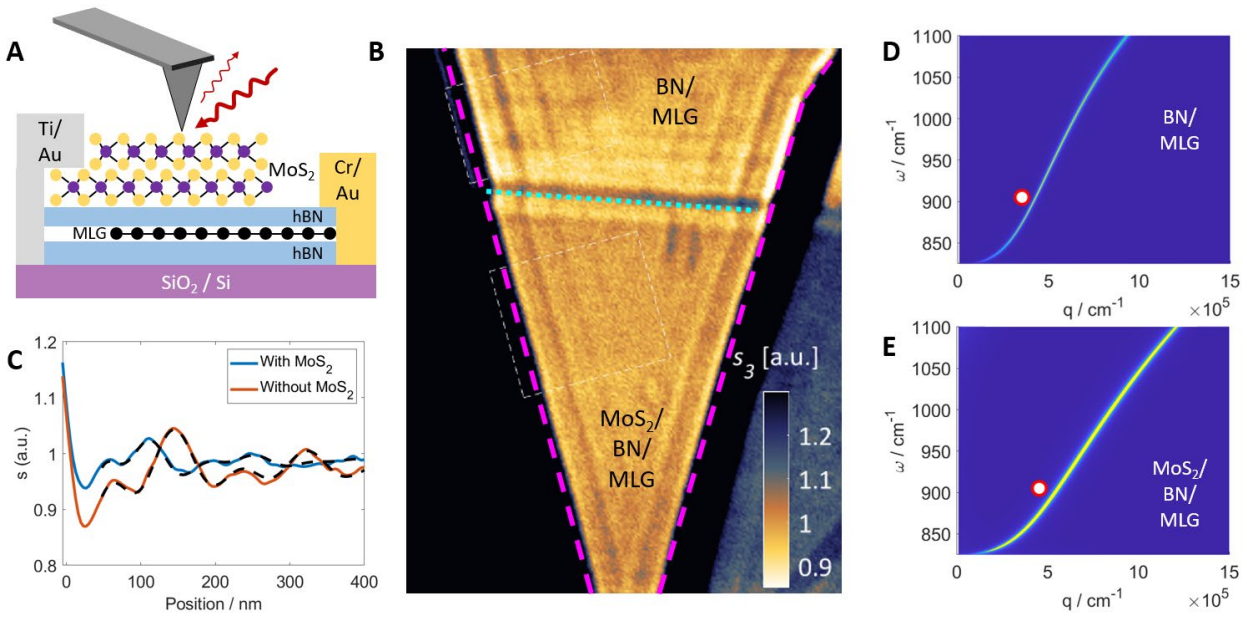

Figure 5.1 | Nano-optics measurements on MoS_2-gated monolayer graphene. (A) Schematic of our nano-infrared experiment and our device. Bilayer MoS_2 is contacted by Ti/Au from above while the graphene has a side contact made of Cr/Au. (B) Two-dimensional image of the nano-infrared amplitude s over our device for $V_{bg} = +80\text{V}$ and $V_{tg} = 0\text{V}$. The edges of MLG and MoS_2 are represented by magenta dashed and green dotted line represents respectively. (C) Line profiles of the nano-infrared amplitude s across a graphene edge showing plasmon polaritons. Black dashed lines represent fits to a damped oscillations model (Section 5.5.3). (D) Calculated imaginary part of the reflection coefficient $\text{Im}(r_P)$ matching the two experimental heterostructures: (D) BN/MLG/BN/SiO_2 (E) MoS_2/BN/MLG/BN/SiO_2. The bright contour of maximal values corresponds to the plasmon mode. The circles in (D) and (E) correspond to experimental data extracted from panel (C) (Section 5.5.3).

In transport experiments, perpendicular displacement field can be introduced using an evaporated metal layer or a graphite layer as a top-gate in conjunction with a back-gate. While

transport (*9*) and some far-field optical experiments (*10*, *150*, *151*) can be performed on such structures, they are incompatible with nano-infrared experiments for multiple reasons. First, such layers are relatively thick (tens of nm) which make the underlying graphene layer inaccessible to nano-optics experiments. When the layers are made thinner, the presence of a high density of high mobility free carriers leads to plasmonic effects in the top-gate which modifies and obscures the behavior of the underlying graphene layer.

Recent work has shown that MLG could be used as a top gate to study Moiré patterns in vdW heterostructures (*152*). However, the capabilities and limitations of the top gate were not fully explored. While Ref (*152*) showed that two-dimensional domains in a Moiré pattern could be visualized through a MLG top gate, it's not yet known if the plasmonic phenomena in the underlying graphene layer and one-dimensional features such as domain walls in BLG can be resolved. In this work, we demonstrate and fully characterize two approaches for nano-optics compatible top gates: bilayer MoS_2 and MLG. We are able to visualize the plasmons in the MLG and TBG layers underneath the MoS_2 top-gate. We further demonstrate a depletion of the carrier density of the underlying graphene layers with the top-gate through measurements of the plasmon wavelength and nano-infrared scattering amplitude. We then explore the use of a MLG layer as the top-gate for BLG. The doped MLG layer is a robust top-gate, but has strong optical response at mid-infrared frequencies of its own. We therefore explore the possibility of selectively probing the underlying BLG through nano-photocurrent imaging and are able to visualize domain walls in the BLG layer. Our work paves the way for realization of fully tunable vdW devices compatible with nano-optics experiments.

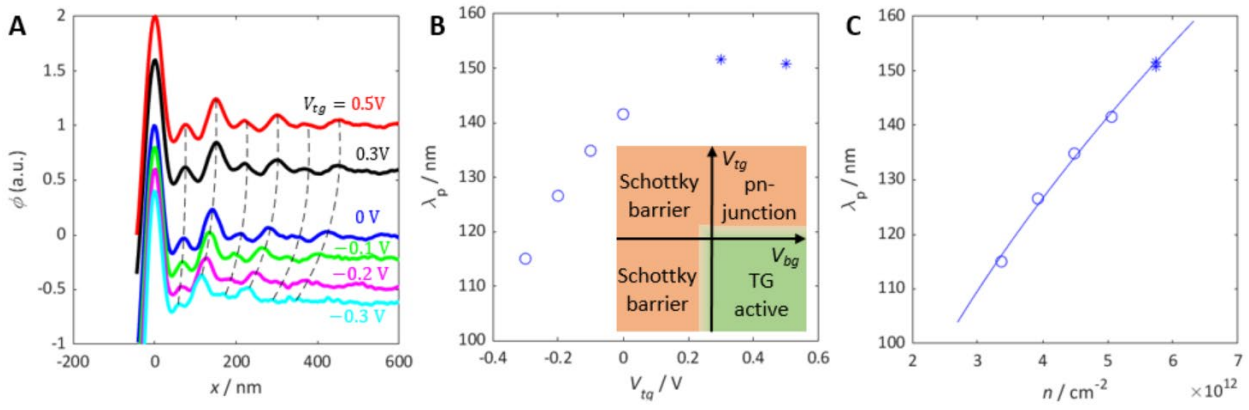

Figure 5.2 | Carrier density modulation in monolayer graphene with MoS_2 top-gate. (A) Line profiles of the nano-infrared phase ϕ for various values of V_{tg} at $V_{bg} = +80$V, showing a clear change in the plasmon wavelength. The data is scaled and shifted for clarity. Dashed lines follow the plasmonic peaks and are used to extract λ_p. (B) Plasmon wavelength as a function of the top-gate voltage V_{tg}. Circles represent $V_{tg} \leq 0$V and asterisks represent $V_{tg} > 0$V. Inset shows the behavior of the MoS_2 top-gate for various V_{tg} and V_{bg} values. The top-gate is most effective in one of the four quadrants and its performance decays quickly in other quadrants. (C) λ_p as a function of the estimated carrier density in the graphene layer n. The data points for $V_{tg} > 0$V cluster together because the top-gate is ineffective (described in text).

5.2 Strengths and weaknesses of a MoS_2 top gate

Figure **5.**1(A) shows a schematic of our experimental setup. Our first device consists of monolayer graphene encapsulated between hexagonal boron nitride (hBN) layers. The thickness of the top hBN layer is kept small (2 nm) to allow optical near-field access to the underlying graphene layer. A bilayer of MoS_2 is then placed on the top hBN layer for use as a top-gate while a doped silicon layer underneath the heterostructure serves as the bottom-gate. We chose MoS_2 because it is expected to be transparent to mid-infrared light. We study this device using a scanning

nano-infrared microscope where incident light from a quantum cascade laser is focused onto the apex of a sharp metallic tip. We used light of frequency $\omega = 1/\lambda_0 = 905$ cm^{-1} for all experiments in this manuscript. The amplitude s and phase ϕ of the scattered light are detected with an interferometric method (*153*). The sharpness of the tip provides the momentum necessary to launch SPPs which propagate radially outward from the tip. When the SPPs encounter a physical (*48*, *49*) or electronic (*39*) boundary, they are reflected and form a standing wave pattern that we directly visualize.

Figure **5.**1(B) shows a two-dimensional map of the nano-infrared amplitude s measured on our device with $V_{bg} = +80$V and $V_{tg} = 0$V. The green dotted line marks the edge of the MoS_2 layer such that the area above the line does not contain MoS_2. We observe clear fringes parallel to the edges of the MLG (marked by magenta dashed lines) throughout the image. These fringes confirm that we are able to launch and image SPPs in the MLG layer even when the MLG is underneath MoS_2.

A comparison of the fringes above and below the MoS_2 boundary in Fig **5.**1(B) indicates that the plasmon wavelength is smaller in the region with MoS_2. In Fig **5.**1(C), we plot the line profiles extracted across the graphene edge from both regions. The line profiles confirm that the plasmon wavelength is reduced to 138 nm under the MoS_2 layer (blue line in Fig **5.**1(C)) compared to 177 nm without MoS_2 (orange line in Fig **5.**1(C)). This reduction is due to the large static dielectric constant of MoS_2 and the resulting screening. This change in plasmon wavelength is consistent with the calculated change in plasmon dispersion (Fig **5.**1(D) and **5.**1(E)).

Figure **5.**2 demonstrates the tuning of carrier density in the MLG layer with the MoS_2 top-gate. Figure **5.**2(A) shows line-profiles of the nano-infrared phase ϕ for different values of top-gate bias V_{tg} for a fixed value of back-gate bias $V_{bg} = +80$V. We observe a clear change in the plasmon

wavelength as V_{tg} is changed. At negative values of V_{tg}, we observe a decrease in the plasmon wavelength which is consistent with a depletion of the carrier density in the graphene layer. When V_{tg} is tuned to $+0.3$V, we observe an increase in λ_p. But a further increase in V_{tg} to $+0.5$V does not change λ_p, indicating that the carrier density in MLG does not change (Figure 5.2(B) and 5.2(C)). This limitation is the result of a pn-junction forming in the MoS_2 layer as described below. Taken together, our results confirm that we are able to deplete the carrier density in the graphene layer which is necessary for realizing gapped BLG.

We now turn to the BLG region of our heterostructure that is also covered by the MoS_2 top-gate. The BLG in our heterostructure was produced by a 'tear-and-stack' technique (Section 5.51) which resulted in a small twist angle (estimated to be ~0.02°) between the layers and a large Moiré pattern. Atomic relaxation leads to the formation of larger domains of Bernal bilayer graphene separated by domain walls (*26*) that host topological states (*27*, *28*, *32*). The change in optical conductivity arising from the topological states reflects plasmon polaritons leading to fringes in nano-infrared experiments (Refs (*34*, *94*), Chapter 2). Changing the carrier density and interlayer bias across the BLG changes the optical conductivity across the domain wall and modifies the fringe pattern (*34*). Figure **5.**3(B) shows the nano-infrared amplitude over a region containing several domain walls for $V_{bg} = +80$V and $V_{tg} = 0$V. We observe features in the amplitude that correspond to plasmons reflecting off the domain walls (Refs (*77*, *94*), Chapter 2). As we increase V_{tg}, we observe a clear change in the plasmonic pattern that confirms the changing carrier density and interlayer bias in the BLG layer. By demonstrating dual-gating and observing propagation of plasmons, we have thus shown the feasibility of performing nano-infrared studies of a dual gated system using this approach.

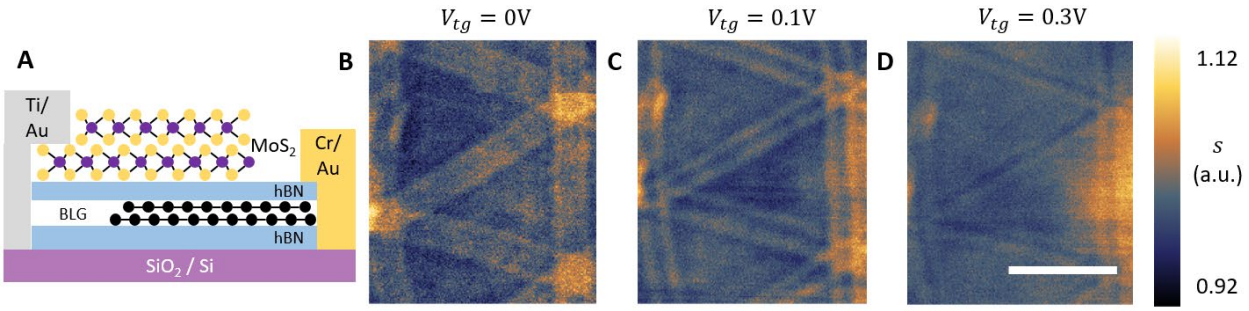

Figure 5.3 | Demonstration of top-gating effect in bilayer graphene domain walls. (A) Schematic of the heterostructure. (B, C, D) Nano-infrared amplitude image of domain walls in BLG for three different top-gate voltages with $V_{BG} = +80\text{V}$. Scale bar 400nm.

Next, we discuss the limitations of the TMD top-gate. First, we consider the performance of the top-gate at a negative V_{bg}. Because of the high work function of MoS_2, evaporated metals typically make n-type contact to MoS_2 (*154*). The geometry of our device is such that the titanium metal contacts to the MoS_2 lie outside the graphene region (Fig **5.**1(A)). Therefore the contact resistance at the Ti/MoS_2 layer depends only on V_{bg}. At a large negative V_{bg}, the Schottky barrier at the Ti/MoS_2 junction is too large and renders the top-gate ineffective. Therefore, unless doped by local gates (*155*), the MoS_2 top-gate is only functional for positive V_{bg} where n-type carriers are injected into the MoS_2 layer.

At a fixed, positive V_{bg}, the region by the contacts remains n-doped and the application of V_{tg} starts to change the carrier density in the MoS_2 region directly above the graphene layer. When V_{tg} is negative, the carriers in the MoS_2 layer are all n-type. However, as V_{tg} becomes positive, the MoS_2 region above the graphene becomes hole-like. Since the carriers close to the contacts remain electron-like, a pn-junction forms in the MoS_2 layer along the graphene edge. This pn-junction isolates the Ti contacts from the MoS_2 region above the graphene layer and causes the top-gate to

become ineffective. Taking the effects of the Schottky barrier and the pn-junction together, we conclude that the top-gate is most effective only in one of the four quadrants in the $V_{tg} - V_{bg}$ plane and its performance decays quickly in the other quadrants, as illustrated in the inset of Fig **5.**2(B).

5.3 Strengths and weaknesses of a monolayer graphene top gate

To achieve full control over the properties of BLG, we could consider other materials as a top-gate. While a p-type TMD such as WS_2 can lead to a top-gate that is functional at negative V_{bg}, the pn-junction limitation would still restrict its functionality to just one quadrant in the $V_{bg} - V_{tg}$ plane. This limitation arises directly because of the electronic bandgap and therefore would be present for any semiconductor. Only a gapless ambipolar material, such as monolayer graphene, can overcome this limitation.

We now explore the possibility of using monolayer graphene (MLG) as a top-gate for BLG. The ambipolar nature of MLG means that the contacts do not restrict the range of operational gate voltages. However, MLG has a strong optical response of its own in mid-infrared frequencies. At the same time, if the Fermi energy in the top gate layer is very small, interband transitions in the top gate layer will lead to an increased damping that can obscure the plasmonic features in nano-infrared imaging (Section 5.5.4.1). Therefore, we also explored the nano-photocurrent technique which can selectively probe the underlying BLG layer.

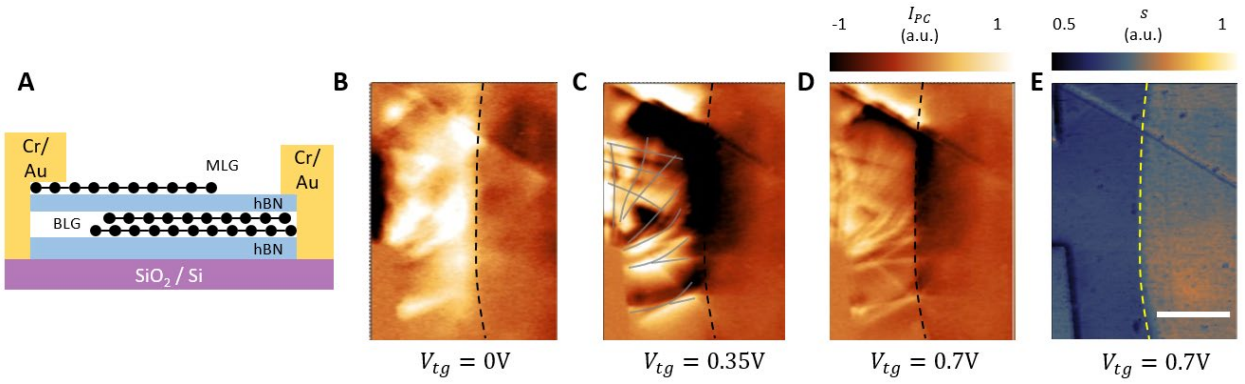

Figure 5.4 | Monolayer graphene as a top-gate for domain walls in bilayer graphene. (A) Schematic of the heterostructure (B, C, D) Nano-photocurrent images for three different V_{tg} showing domain walls in the underlying bilayer graphene. (E) Nano-infrared amplitude image at $V_{tg} = 0.7\text{V}$. Black dashed lines in (B-D) and yellow dashed line in (E) correspond to the boundary of the top-gated region. Grey solid lines in (C) indicate the domain walls in BLG. Scale bar 1μm.

Figure 5.4(A) shows a schematic of our heterostructure with a MLG top gate. Figure 5.4(E) shows the nano-infrared amplitude image of our device with $V_{bg} = 0\text{V}$ and $V_{tg} = +0.7\text{V}$. The yellow dashed line indicates the boundary of the MLG top gate. We observe a nano-infrared contrast indicating that the top gate is active but we see no other features, most likely because the carrier density in the bilayer graphene is too low (Section 5.5.1.3). Figure 5.4 (A-D) shows the results of nano-photocurrent experiments (*4*) at different V_{tg}. As V_{tg} is increased from zero, the nano-photocurrent begins to resemble the photocurrent profiles seen in other twisted BLG heterostructures (Refs (*156*, *157*), Chapter 4) and are known to arise from domain walls. Based on the periodicity of the Moiré pattern, we estimate a twist angle of ~0.1°. The irregularity of the domain wall pattern in Fig 5.4 in comparison to Fig 5.3 is due to strain accumulated during the

fabrication process. These results demonstrate that we are able to resolve the domain wall pattern in nano-photocurrent through a doped MLG top gate.

5.4 Direct comparison between MoS_2 and monolayer graphene top gates

Finally, we directly compare the properties of MLG and bilayer MoS_2 top gates for nano-infrared experiments with the following hypothetical scenario. We consider an encapsulated heterostructure of monolayer graphene with a carrier density of $n = 6 \cdot 10^{12}\text{cm}^{-2}$ with either a MLG top gate (Fig. 5.5(A)) or a TMD top gate (Fig. 5.5(B)). We then vary the carrier concentration only in the top gate to observe how strongly the top gate modifies the behavior of the underlying graphene layer. The plasmonic dispersions in both cases are shown in Figure 5.5. The dispersion changes significantly with a MLG top gate while it remains mostly unchanged in case of the TMD top gate. The large change in the dispersion with the MLG top gate is due to strong hybridization between the plasmonic modes in the two graphene layers (*158–160*). The smaller change in dispersion with a TMD top gate demonstrates that the hybridization of the plasmonic modes is negligible with a TMD top gate. The thickness of the TMD top gate leads to a small but significant effect on the plasmonic dispersion, as discussed in Section 5.5.5. These results suggest that a TMD top gate allows direct access to the plasmonic phenomena in the underlying graphene layer in nano-infrared experiments with minimal obscuring.

In conclusion, our results demonstrate two near-field compatible top gates for BLG. With MoS_2, we were able to study plasmons through scattering nano-infrared experiments and demonstrate the depletion of carriers in the underlying graphene layers. With a MLG top gate, we were able to visualize the domain walls in the underlying BLG through nano-photocurrent

experiments. Our work paves the way for exploring the plasmonic properties of gapped bilayer graphene with scanning nano-infrared and nano-photocurrent experiments.

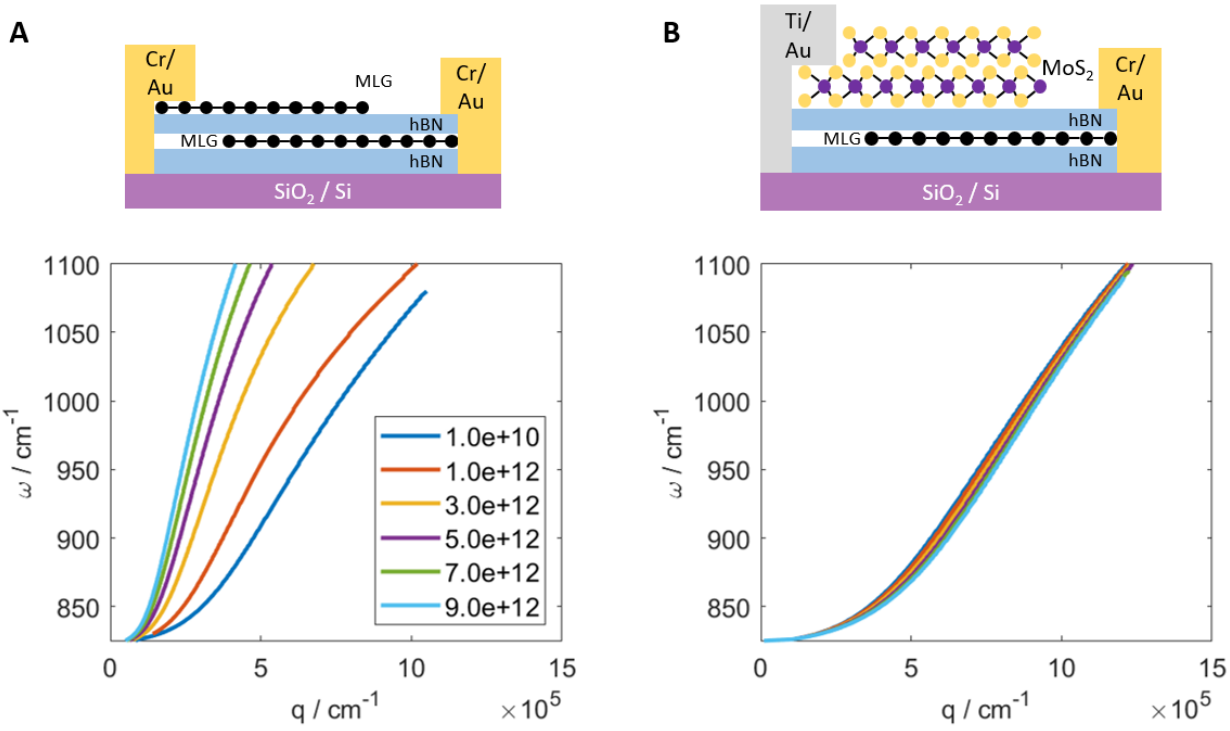

Figure 5.5 | Direct comparison between the MLG and TMD top gates. (A) Change in the dispersion of the plasmonic mode of the heterostructure as the carrier density in the top gate is varied for a MLG top gate. (B) Similar plot as (A) for bilayer MoS_2 top gate. The thicknesses of the top and bottom hBN are 5nm and 30nm respectively and the underlying MLG layer is doped to $n = 6 \cdot 10^{12}\mathrm{cm}^{-2}$.

5.5 Supplementary material

5.5.1 Materials and Methods

5.5.1.1 Device fabrication

The results shown in Figs 5.1-5.3 were obtained from a MoS_2 top-gated device (Device 1) consisting of graphene layers encapsulated in hexagonal boron nitride with a MoS_2 layer on top. The stack was fabricated using the dry transfer method. A poly(bisphenol A carbonate) (PC) coated on a stamp made of transparent elastomer polydimethylsiloxane (PDMS). The two graphene layers to form the bilayer graphene were assembled by tearing a large single layer of graphene and stacking them together. The inherent strain in this process results in one of the layers twisting slightly relative to the other layer and leads to the formation of domain walls (*26*). The contacts to the TMD layer were made of titanium while side contacts (*161*) to the graphene layer were made of chromium and gold.

The MLG top-gated device (Device 2) was also fabricated with the dry transfer method but with a poly(propylene carbonate) (PPC) coated stamp. The heterostructure was fabricated in the reverse order so that the MLG top-gate was not contaminated by contact with the PPC polymer and flipped onto a SiO_2/Si chip. After flipping, the heterostructure was annealed in vacuum to remove the PPC residue. Electrical contacts to the graphene layers were made with chromium and gold.

The results shown in Fig 5.14 were obtained from another MoS_2 top-gated device (Device 3) that was also fabricated with the dry transfer method.

5.5.1.2 Plasmon wavelength and dispersion calculations

The dielectric constants for MoS_2, hBN, and SiO_2 used in the reflection coefficient calculations of Fig 5.1(D), 5.1(E), and the rest of the manuscript were obtained from Refs (*162*), (*132*), and (*163*) respectively. The plasmon wavelength used to plot the crosses was determined by the spacing between the fringes in the spatial profiles of the near-field phase (Fig 5.2(A)).

For the calculations in Figure 5.5, we assumed that the dielectric properties of a doped MoS_2 layer can be described by a Drude model,

$$\epsilon = \epsilon_\infty + \frac{\omega_p^2}{\omega^2 - i\gamma\omega}$$

$$\omega_p^2 = \frac{ne^2}{m^*\epsilon_\infty}$$

where ϵ_∞ and ϵ_0 are the high-frequency and low-frequency dielectric constants, ω_p is the plasma frequency, γ is the damping, n is the carrier density and m^* is the effective mass of the carriers and e is the electron charge. We obtained values for ϵ_∞ from Ref (*162*): along ab-plane $\epsilon_\infty = 15.2$ and along the c-axis $\epsilon_\infty = 6.2$. The band structure of TMDs is anisotropic with the out-of-plane effective mass expected to be smaller than the in-plane effective mass but is not known accurately. Here, we assumed that the effective mass $m^*$was isotropic as a worst case scenario and equal to the measured in-plane effective mass $m^* = 0.45\, m_0$ (*164*), , where m_0 is the free electron mass. The plasmon dispersion is insensitive to γ and we used $\gamma = 300\text{cm}^{-1}$, based on Ref (*165*).

5.5.1.3 Bilayer graphene parameter estimates

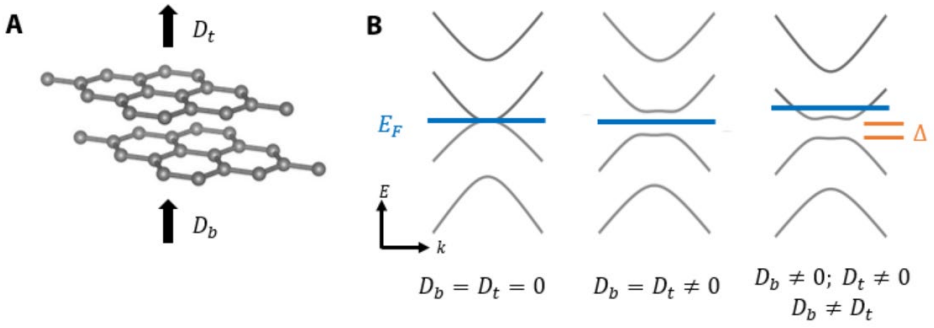

Figure 5.6 | Band structure of bilayer graphene for different displacement fields. (A) Schematic of bilayer graphene with top and bottom displacement fields, D_t and D_b, arising from the top and bottom gates. (B) Schematic band structures for various combinations of D_b and D_t. The bandgap, represented by Δ, is determined by $\overline{D} = (D_b + D_t)/2$.

In this section, we calculate the Fermi energy and interlayer bias of bilayer graphene for the heterostructures considered in this work. The top and bottom gates produce displacement fields above and below the graphene layer given by $D_t = \epsilon_t V_{tg}/d_t$ and $D_b = \epsilon_b V_{bg}/d_b$ where ϵ_t, ϵ_b and d_t, d_b are the dielectric constant and thickness of the top and bottom gate dielectrics respectively (Fig 5.6(a)). The band structure is affected by a combination of the two displacement fields, as shown schematically in Fig 5.6(b). The carrier density in the graphene layer, n, is determined by the difference $D_b - D_t$ and the band gap Δ is determined by $\overline{D} = (D_b + D_t)/2$ (*9*, *10*). We used Ref (*10*) to convert $\overline{D}$ to Δ and computed the Fermi energy E_F by varying it until the carrier density computed with a tight binding model (*34*) matched the desired carrier density. The results are summarized in Table 5.1.

n as a function of $D_b - D_t$	$n = \frac{\epsilon_0}{e}(D_b - D_t) * 1 \cdot 10^5$
V_i as a function of $\overline{D}$	$\Delta = 105\,\overline{D} + 11.1\,\overline{D}^2 - 6.36\,\overline{D}^3$ (based on Ref (*10*))
E_F as a function of n	$E_F = 1.97 \cdot 10^{-14}\,n - 5.32 \cdot 10^{-28} n^2 + 1.00 \cdot 10^{-41}\,n^3$ (based on the tight binding model of Ref (*34*))

Table 5.1 | Polynomial fits for calculating the parameters of BLG for a set of gate voltages. D_b, D_t and $\overline{D}$ are in units of V/nm, n is in units of cm^{-2}, and Δ and E_F are in units of meV.

The gate voltages used in Figures 5.4(D) and 5.4(E) correspond to $D_t = 0.4$ V/nm and $D_b = 0$. Based on the fits in Table 5.1, we see that the corresponding BLG parameters are $\Delta = 21.4$ meV and $n = 2.21 \cdot 10^{12}$ cm^{-2}. These values correspond to a Fermi energy $E_F = 41$ meV. Given that our probing energy $\omega = 905$ cm^{-1} is equivalent to 112 meV, the Fermi energy is too low to prevent interband transitions which occur at frequencies $\omega > 2E_F$. Therefore, we cannot exclude the possibility that the reason we see no nano-infrared contrast from the domain walls in Figure 5.4(E) is because of the increased damping in the BLG layer.

5.5.2 Nano-infrared images at different top-gate voltages

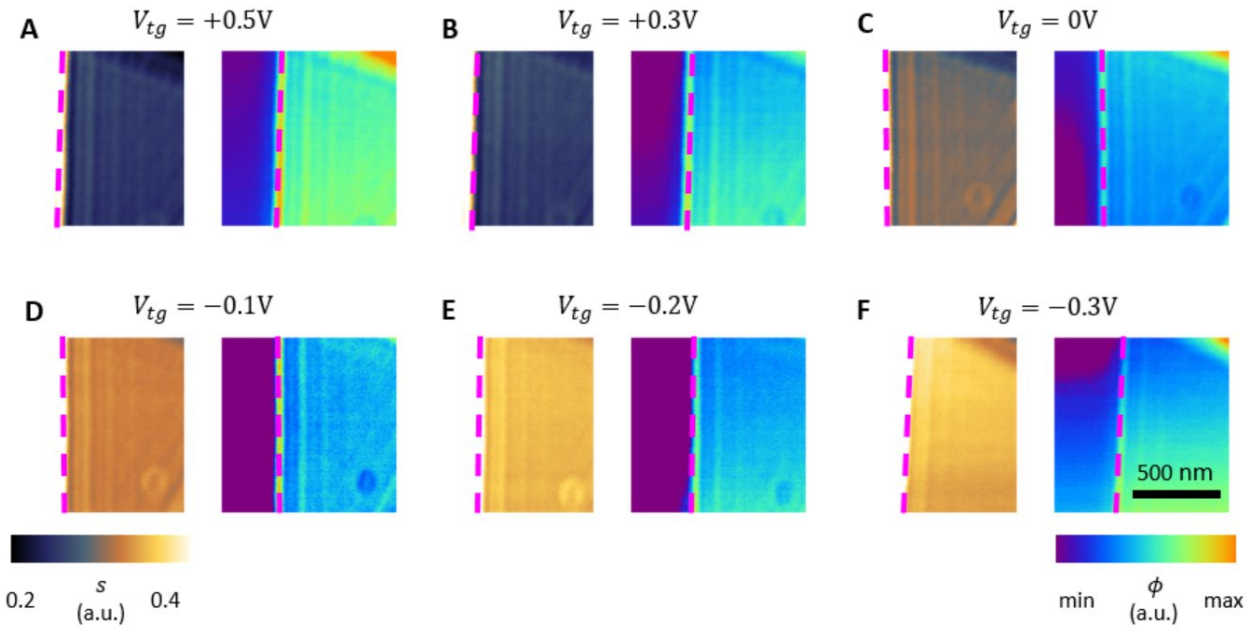

Figure 5.7 | Nano-infrared images of monolayer graphene (MLG) at $V_{bg} = +80V$ and various values of V_{tg}. The images on the left are the nano-infrared amplitude s while the images on the right are of the nano-infrared phase ϕ. The magenta lines represent the physical boundary of the MLG. The color bar limits for the amplitude images are identical for all gate voltages. The variation in the nano-infrared amplitude is consistent with a decrease (increase) of the carrier concentration as V_{tg} is decreased (increased) (*38*).

5.5.3 Line profile fits using the damped oscillations model

The nano-infrared amplitude line profiles were fit using the damped oscillations model (*47*):

$$s = \frac{\cos(2qx)\exp(-2q\gamma x)}{\sqrt{x}} + \alpha \frac{\cos(qx+\phi)\exp(-q\gamma x+\phi)}{x}.$$

Here, the first term represents plasmons that are launched by the tip and reflected by the graphene edge and the second term represents the plasmons that launched by the edge. The edge is assumed to be located at located at $x = 0$. q is the plasmon momentum defined to be $q = \frac{2\pi}{\lambda_p}$, γ is the damping of the plasmonic wave, and α and ϕ capture the difference in the magnitude and phase between the tip-launched waves and the edge-launched waves. The obtained fits are shown in Figure 5.7(A) and Figure 5.1(C). The parameters derived from the fits are shown in Figure 5.7(B).

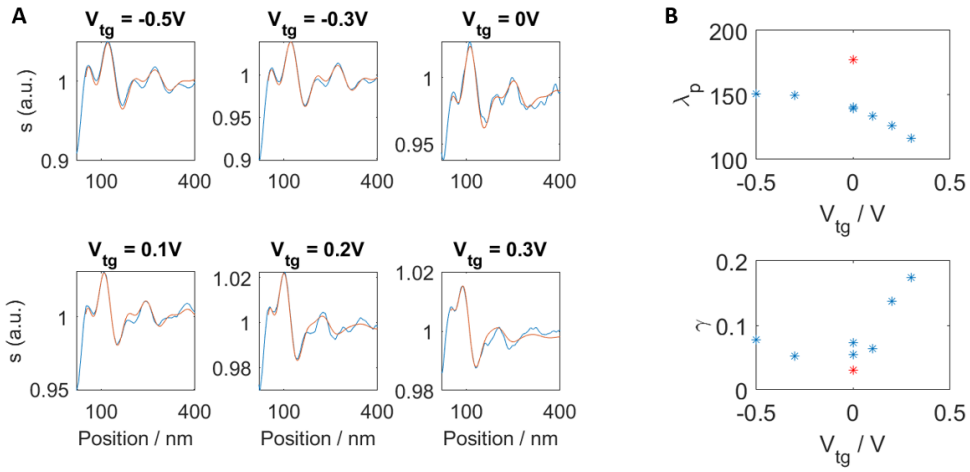

Figure 5.8 | Damped oscillations model fits for different top-gate voltages. (A) Nano-infrared amplitude line profiles for different top-gate voltages. (B) The plasmon wavelength λ_p and the damping γ extracted from the fits. The red asterisks correspond to the data without MoS_2 (red curve in Figure 5.1(C)).

5.5.4 Nano-infrared vs nano-photocurrent with an MLG top gate

In this section, we explore in detail the advantages and disadvantages of nano-infrared imaging and nano-photocurrent techniques with a monolayer graphene (MLG) top gate.

5.5.4.1 Nano-infrared imaging simulations

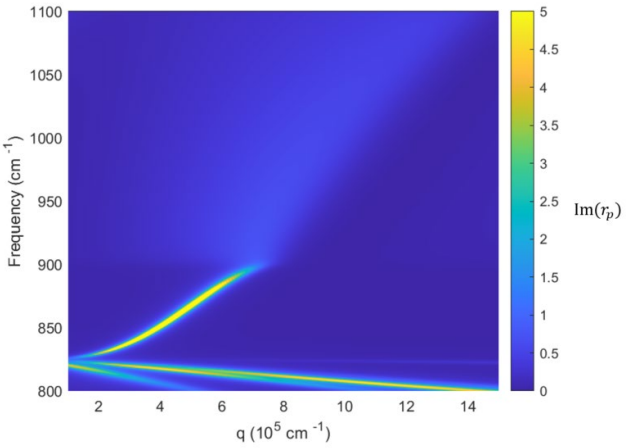

Figure 5.9 | Impact of interband transitions in MLG top gate layer on the polaritonic mode. Plot showing the imaginary part of the reflection coefficient $\mathrm{Im}(r_p)$ for a MLG/hBN (3 nm)/MLG/hBN (30 nm)/SiO_2 heterostructure. The Fermi energies of the top and bottom graphene layers are set to 56 meV (equivalent to 450 cm^{-1}) and 250 meV respectively.

If the carrier density in the MLG top gate is too low, interband transitions in the MLG top gate can affect nano-infrared imaging experiments. Figure 5.9 shows the imaginary part of the reflection coefficient $\mathrm{Im}(r_P)$ for a a MLG/hBN (3 nm)/MLG/hBN (30 nm)/SiO_2 heterostructure. The Fermi energy of the bottom layer is $E_F^{bot} = 250$ meV which is sufficient to produce a strong plasmonic mode. The Fermi energy of the top layer is $E_F^{top} = 56$ meV which is equivalent in energy to 450cm^{-1}. Therefore $\omega_{crit} = 2E_F^{top} = 900\mathrm{cm}^{-1}$ marks the onset of the interband transitions in the top gate and plasmonic mode is damped at higher energies.

Therefore, for experiments performed at $\omega = 905\ \mathrm{cm}^{-1}$, the MLG top gate is not suitable for use in nano-infrared experiments if the Fermi energy and carrier density in the top gate are

below the critical values of $E_F^{crit} \sim 56$ meV and $n_{crit} \sim 2.3 \cdot 10^{11}\text{cm}^{-2}$. The rather small value of n_{crit} suggests that this limitation will not be a major hindrance for practical experiments.

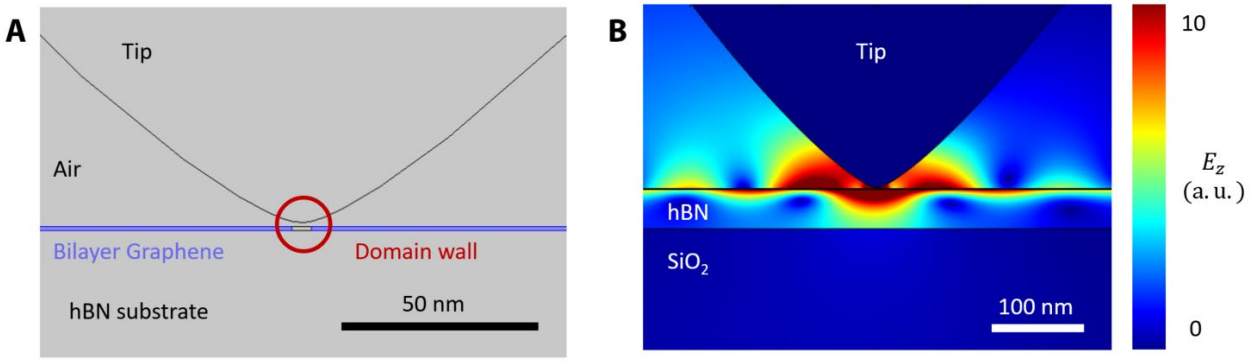

Figure 5.10 | Simulation geometry and example of the calculated electric field. (A) Sketch showing the simplified two dimensional geometry used in our COMSOL simulations for the case where the tip is stationed directly above the domain wall. (B) Typical results of the COMSOL simulation for a heterostructure with no MLG top gate. The oscillatory features in E_z correspond to plasmon polaritons excited by the tip.

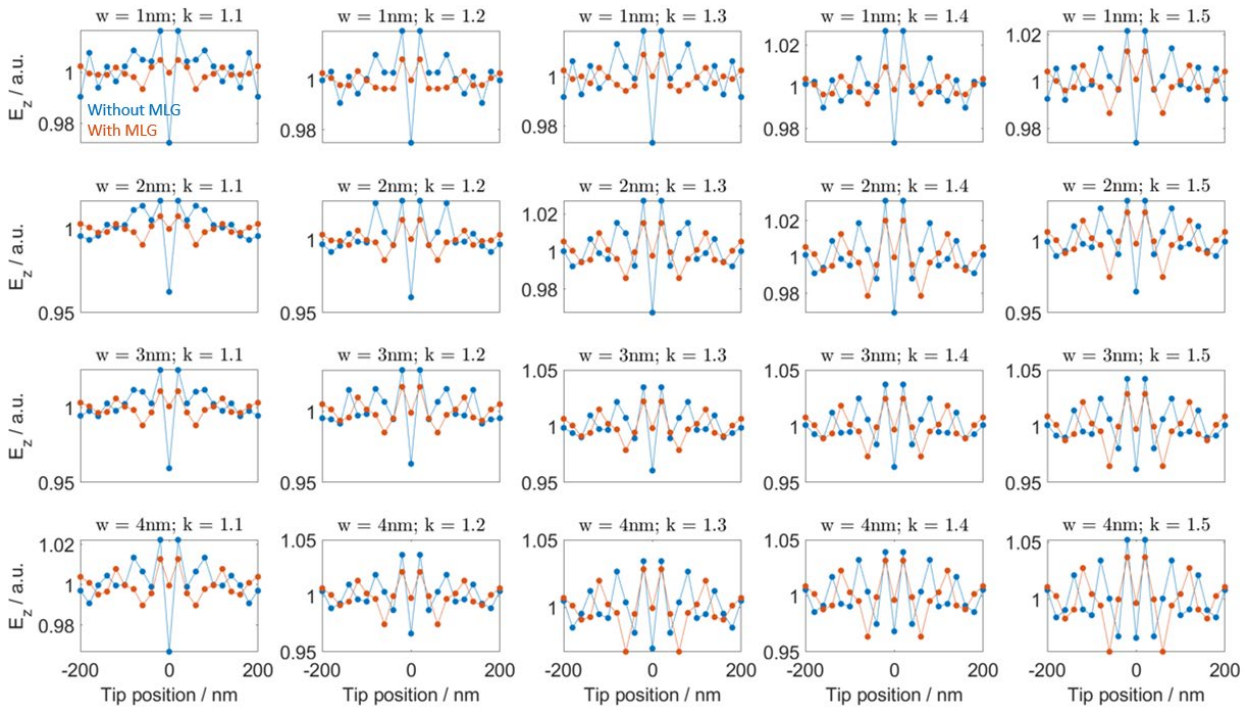

Figure 5.11 | Simulations showing plasmon reflection from domain walls in bilayer graphene with and without MLG top gate. Each panel corresponds to a different value of w and k, as indicated. The domain wall is located at the origin of the x-axis.

Next, we perform simulations to assess the possibility that plasmonic modes in the heterostructure will be scattered by domain walls in twisted bilayer graphene (Refs (*34*, *94*), Chapter 2). We use a simplified two-dimensional geometry and compute the electric field in the electrostatic limit using COMSOL software, as shown in Figure 5.10. We model the tip as a perfectly conducting hyperbola with a minimal radius of curvature of 10 nm. The graphene layers are modeled as 1 nm thick conducting sheets. To approximate the measured signal in nano-infrared experiments, we average the out-of-plane electric field E_z over a 4x4 nm^2 area under the tip. We compute the electric fields for several tip positions to obtain a line profile which can be compared with experiment. All calculations are done at a frequency of $\omega = 905$ cm^{-1}.

The conductivity of the graphene sheets is set to the same value of σ_{BLG} such that the situation with the MLG top gate corresponds to an equal and opposite carrier density in the MLG and BLG layers. We adjust $\mathrm{Im}(\sigma_{BLG})$ to obtain a plasmon wavelength of ~120 nm with no MLG top gate, a value that's typically observed in experiment (*34*, *46*, *47*) and we set $\mathrm{Im}(\sigma_{BLG})/\mathrm{Re}(\sigma_{BLG}) = 20$ (*47*). In reality, the conductivity at the domain walls in BLG is anisotropic and displays several additional features (*34*). However, a rectangular wall can serve as a good approximation (*34*, *77*). Therefore, we represent the domain wall as a rectangular region of width w and conductivity $\sigma_{DW} = k\sigma_{BLG}$ where k is a multiplicative factor. We assume that $w \sim 5$ nm and $k \sim 1.5$ are reasonable values based on Figure 5.10 in Ref (*34*). Note that larger values of w and k can only lead to stronger plasmonic reflections from the domain wall. We repeat the simulations with and without a MLG top gate and compare the results in Fig 5.11.

The results in Fig 5.11 show fringes in E_z as the tip is moved away from the domain wall. The magnitude of these oscillations is ~5% which is comparable to the experimentally observed change in nano-infrared signal without a MLG top gate (Refs (*34*, *94*), Chapter 2). These factors taken together lead us to conclude that our 2D simulations are a good approximation to real experiments. Finally, the magnitude of the plasmonic reflection with the MLG top gate is comparable to the case without a MLG top gate for all values of w and k considered. Therefore, we conclude that domain walls in bilayer graphene could be observed underneath a MLG top gate in future experiments.

5.5.4.2 Nano-photocurrent simulations: E_x at the graphene layer

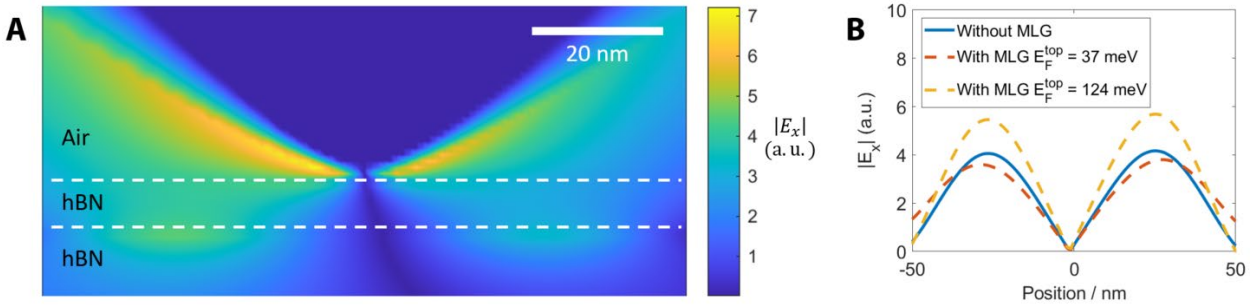

Figure 5.12 | In-plane electric field with a MLG top gate. (A) Two-dimensional plot of the absolute value of the in-plane electric field, $|E_x|$. The two dashed white lines represent the two graphene layers. $E_F^{top} = 37$ meV and $E_F^{bot} = 250$ meV. (B, C) Line profiles of $|E_x|$ for the cases with and without the MLG top gate for two different E_F^{top}. $E_F^{bot} = 250$ meV in all cases.

Photocurrent in graphene is generated through the photothermoelectric effect (*55*, *58*, *60*). The absorption of incident light generates hot carriers in graphene. When the hot carriers encounter variations in the Seebeck coefficient, a thermoelectric voltage is generated which drives a current through the sample. Since the electronic conductivity of graphene is negligible in the out-of-plane direction, the in-plane electric field determines the photocurrent response (Ref (*156*), Chapter 4).

Here, we simulate a heterostructure with monolayer graphene with Fermi energy $E_{F,bot} = 250$ meV. We either include or exclude a MLG top gate and compare the electric field profiles. Figure 5.12(A) shows the absolute value of the in-plane electric field $|E_x|$ and Fig 5.12(B) shows the line profiles at the probe graphene layer. The addition of the top gate does not significantly affect the in-plane electric field irrespective of its Fermi energy. Therefore, the photocurrent patterns produced by any Seebeck coefficient variations in the bottom graphene layer will be

similar to those produced by the same Seebeck coefficient variations in typical nano-photocurrent with no monolayer graphene top gate. These simulations establish that a monolayer graphene top gate can be successfully used for nano-photocurrent experiments under any circumstances.

5.5.5 Thickness dependence of the MoS_2 top gate

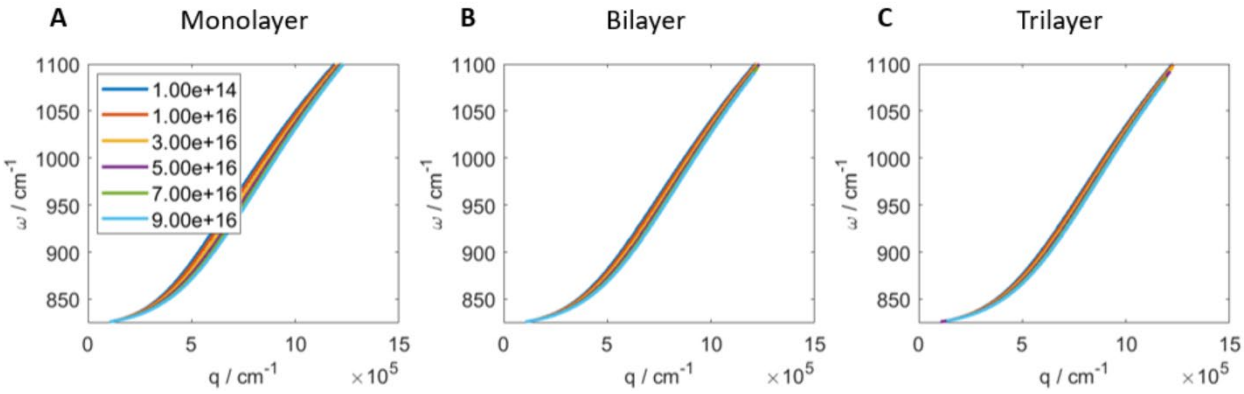

Figure 5.13 | Thickness dependence of the MoS_2 top gate. Change in the dispersion of the plasmonic mode of the heterostructure for varying carrier density in the MoS_2 top gate. The different panels correspond to different thicknesses of MoS_2. The legend corresponds to the carrier densities in the top gate. Panel (B) here is identical to Figure 5.5(B).

In our experiments, we used a bilayer MoS_2 as the top gate since it is easier to make electrical contact to multilayer MoS_2 than monolayer MoS_2 while also minimizing the thickness of the top gate. Here, we explore the effect of varying the MoS_2 thickness using the heterostructure considered in Figure 5.5. Figure 5.13 shows the same plot as Figure 5.5(B) for three different MoS_2 thicknesses. We see that the monolayer MoS_2 shows the largest change in the dispersion while the trilayer MoS_2 shows the least change. Since the areal carrier density in the top gate is fixed, having more layers

means that the charge is spread out over a thicker layer, leading to a smaller volume carrier density and a smaller screening effect.

5.5.6 Gating of bilayer graphene with MoS_2

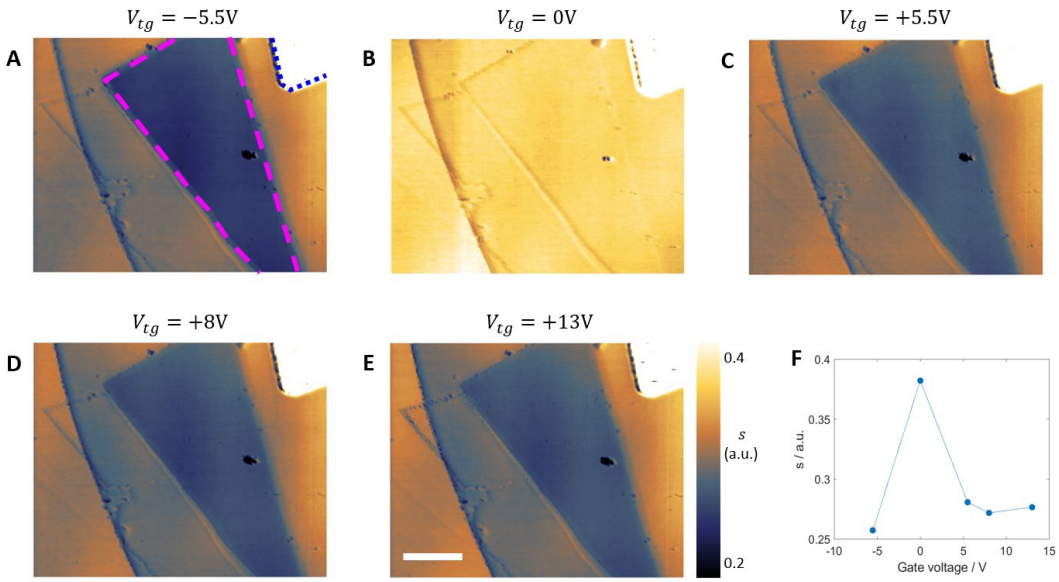

Figure 5.14 | Gating bernal bilayer graphene with a MoS_2 top-gate (Device 3). (A) – (E) Nano-infrared amplitude images for $V_{bg} = 0V$ various values of V_{tg}. The magenta dashed lines represent the boundaries of the BLG layer while the blue dotted lines represent the boundary of a gold electrode. Scale bar 2μm. (F) Dependence of the nano-infrared amplitude of the bilayer graphene layer on V_{tg}. The decrease in the nano-infrared amplitude as V_{tg} is increased is consistent with an increase in the carrier concentration in the BLG layer (*38*).

In this section, we present nano-infrared data from another bilayer graphene device (Device 3) with a MoS_2 top-gate. In this device, there were no domain walls. We observed a change in the nano-infrared signal when varying the top-gate voltage V_{tg}.

Concluding Remarks

The discovery of strongly correlated electronic phases in twisted bilayer graphene has led to an enormous interest in twisted van der Waals (vdW) heterostructures. While twisting vdW layers provides a new control knob and never before seen functionalities, it also leads to large spatial variations in the electronic properties. Scanning probe experiments are therefore necessary to fully understand the properties of twisted vdW heterostructures.

In this thesis, we studied twisted bilayer graphene with two scanning probe techniques, nano-infrared imaging and nano-photocurrent imaging. At small twist angles, we resolved the spatial variations of the electronic structure occurring within a Moiré unit cell. With nano-infrared imaging, we showed that the periodic domain walls act as a photonic crystal for propagating surface plasmon polaritons (Chapter 2). Meanwhile, with nano-photocurrent experiments, we resolved DC Seebeck coefficient changes at the domain walls (Chapter 4). At larger twist angles, we mapped the twist angle variations naturally occurring in our device with a combination of nano-photocurrent and nano-infrared imaging (Chapter 3). Given that the properties of twisted bilayer graphene are strongly dependent on a perpendicular displacement field, we also investigated different materials for use as nano-optics compatible top gates in future experiments (Chapter 5).

In conclusion, this thesis demonstrates the key role nano-optics techniques play in elucidating the rich physics present in twisted vdW heterostructures.

References

1. M. Dressel, G. Grüner, *Electrodynamics of Solids* (Cambridge University Press, 2002).

2. B. Knoll, F. Keilmann, Near-field probing of vibrational absorption for chemical microscopy. *Nature*. **399**, 134–137 (1999).

3. R. Hillenbrand, F. Keilmann, Complex optical constants on a subwavelength scale. *Phys. Rev. Lett.* **85**, 3029–3032 (2000).

4. A. Woessner *et al.*, Near-field photocurrent nanoscopy on bare and encapsulated graphene. *Nat. Commun.* **7**, 1–7 (2016).

5. K. S. Novoselov *et al.*, Electric Field Effect in Atomically Thin Carbon Films. *Science*. **306**, 666–669 (2004).

6. A. H. Castro Neto, F. Guinea, N. M. R. Peres, K. S. Novoselov, A. K. Geim, The electronic properties of graphene. *Rev. Mod. Phys.* **81**, 109–162 (2009).

7. D. N. Basov, M. M. Fogler, A. Lanzara, F. Wang, Y. Zhang, Colloquium: Graphene spectroscopy. *Rev. Mod. Phys.* **86**, 959–994 (2014).

8. E. McCann, M. Koshino, The electronic properties of bilayer graphene. *Reports Prog. Phys.* **76**, 056503 (2013).

9. J. B. Oostinga, H. B. Heersche, X. Liu, A. F. Morpurgo, L. M. K. Vandersypen, Gate-induced insulating state in bilayer graphene devices. *Nat. Mater.* **7**, 151–157 (2008).

10. Y. Zhang *et al.*, Direct observation of a widely tunable bandgap in bilayer graphene. *Nature*. **459**, 820–823 (2009).

11. K. S. Novoselov, A. Mishchenko, A. Carvalho, A. H. Castro Neto, 2D materials and van der Waals heterostructures. *Science*. **353**, aac9439 (2016).

12. A. K. Geim, I. V. Grigorieva, Van der Waals heterostructures. *Nature*. **499**, 419–425 (2013).

13. R. Bistritzer, A. H. MacDonald, Moire bands in twisted double-layer graphene. *Proc. Natl. Acad. Sci. U. S. A.* **108**, 12233–7 (2011).

14. B. Hunt *et al.*, Massive Dirac Fermions and Hofstadter Butterfly in a van der Waals Heterostructure. *Science*. **340**, 1427–1430 (2013).

15. C. R. Dean *et al.*, Hofstadter's butterfly and the fractal quantum Hall effect in moiré superlattices. *Nature*. **497**, 598–602 (2013).

16. L. A. Ponomarenko *et al.*, Cloning of Dirac fermions in graphene superlattices. *Nature*. **497**, 594–597 (2013).

17. R. Ribeiro-Palau *et al.*, Twistable electronics with dynamically rotatable heterostructures. *Science*. **361**, 690–693 (2018).

18. Y. Cao *et al.*, Correlated insulator behaviour at half-filling in magic-angle graphene superlattices. *Nature*. **556**, 80–84 (2018).

19. Y. Cao *et al.*, Unconventional superconductivity in magic-angle graphene superlattices. *Nature*. **556**, 1–17 (2018).

20. Y. Cao *et al.*, Strange Metal in Magic-Angle Graphene with near Planckian Dissipation. *Phys. Rev. Lett.* **124**, 076801 (2020).

21. Y. Cao *et al.*, Nematicity and competing orders in superconducting magic-angle graphene. *arXiv*: 2004:04148 (2020).

22. A. L. Sharpe *et al.*, Emergent ferromagnetism near three-quarters filling in twisted bilayer graphene. *Science*. **365**, eaaw3780 (2019).

23. M. Serlin *et al.*, Intrinsic quantized anomalous Hall effect in a moiré heterostructure. *Science*. **367**, 900–903 (2020).

24. L. Wang *et al.*, Correlated electronic phases in twisted bilayer transition metal dichalcogenides. *Nat. Mater.* **19**, 861–866 (2020).

25. K. Zhang, E. B. Tadmor, Structural and electron diffraction scaling of twisted graphene bilayers. *J. Mech. Phys. Solids*. **112**, 225–238 (2018).

26. H. Yoo *et al.*, Atomic and electronic reconstruction at the van der Waals interface in twisted bilayer graphene. *Nat. Mater.* **18**, 448–453 (2019).

27. I. Martin, Y. M. Blanter, A. F. Morpurgo, Topological confinement in bilayer graphene. *Phys. Rev. Lett.* **100**, 1–4 (2008).

28. Z. Qiao, J. Jung, Q. Niu, A. H. MacDonald, Electronic highways in bilayer graphene. *Nano Lett.* **11**, 3453–3459 (2011).

29. J. Jung, F. Zhang, Z. Qiao, A. H. MacDonald, Valley-Hall kink and edge states in multilayer graphene. *Phys. Rev. B.* **84**, 1–5 (2011).

30. A. Vaezi, Y. Liang, D. H. Ngai, L. Yang, E. A. Kim, Topological edge states at a tilt boundary in gated multilayer graphene. *Phys. Rev. X.* **3**, 1–9 (2013).

31. J. S. Alden *et al.*, Strain solitons and topological defects in bilayer graphene. *Proc. Natl. Acad. Sci.* **110**, 11256–11260 (2013).

32. L. Ju *et al.*, Topological valley transport at bilayer graphene domain walls. *Nature.* **520**, 650–655 (2015).

33. L. Jiang *et al.*, Soliton-dependent plasmon reflection at bilayer graphene domain walls. *Nat. Mater.* **15**, 840–844 (2016).

34. B. Y. Jiang *et al.*, Plasmon Reflections by Topological Electronic Boundaries in Bilayer Graphene. *Nano Lett.* **17**, 7080–7085 (2017).

35. A. S. McLeod *et al.*, Model for quantitative tip-enhanced spectroscopy and the extraction of nanoscale-resolved optical constants. *Phys. Rev. B.* **90**, 085136 (2014).

36. S. Mastel *et al.*, Understanding the Image Contrast of Material Boundaries in IR Nanoscopy Reaching 5 nm Spatial Resolution. *ACS Photonics.* **5**, 3372–3378 (2018).

37. Z. Fei *et al.*, Infrared nanoscopy of dirac plasmons at the graphene-SiO2interface. *Nano Lett.* **11**, 4701–4705 (2011).

38. G. X. Ni *et al.*, Fundamental limits to graphene plasmonics. *Nature.* **557**, 530–533 (2018).

39. Z. Fei *et al.*, Electronic and plasmonic phenomena at graphene grain boundaries. *Nat. Nanotechnol.* **8**, 821–825 (2013).

40. H. A. Atwater, The Promise of Plasmonics. *Sci. Am.* **296**, 56–62 (2007).

41. S. Dai *et al.*, Tunable phonon polaritons in atomically thin van der Waals crystals of boron nitride. *Science*. **343**, 1125–1129 (2014).

42. F. Hu *et al.*, Imaging exciton-polariton transport in MoSe 2 waveguides. *Nat. Photonics*. **11**, 356–360 (2017).

43. D. N. Basov, M. M. Fogler, F. J. Garcia de Abajo, Polaritons in van der Waals materials. *Science*. **354**, aag1992 (2016).

44. D. N. Basov, A. Asenjo-Garcia, P. J. Schuck, X. Zhu, A. Rubio, Polariton panorama. *Nanophotonics*. **10**, 549–577 (2020).

45. M. Jablan, H. Buljan, M. Soljačić, Plasmonics in graphene at infrared frequencies. *Phys. Rev. B*. **80**, 1–7 (2009).

46. G. X. Ni *et al.*, Ultrafast optical switching of infrared plasmon polaritons in high-mobility graphene. *Nat. Photonics*. **10**, 244–247 (2016).

47. A. Woessner *et al.*, Highly confined low-loss plasmons in graphene-boron nitride heterostructures. *Nat. Mater.* **14**, 421–425 (2015).

48. Z. Fei *et al.*, Gate-tuning of graphene plasmons revealed by infrared nano-imaging. *Nature*. **486**, 82–85 (2012).

49. J. Chen *et al.*, Optical nano-imaging of gate-tunable graphene plasmons. *Nature*. **487**, 77–81 (2012).

50. E. H. Hasdeo, J. C. W. W. Song, Long-Lived Domain Wall Plasmons in Gapped Bilayer Graphene. *Nano Lett.* **17**, 7252–7257 (2017).

51. L. Brey, T. Stauber, T. Slipchenko, L. Martín-Moreno, Plasmonic Dirac Cone in Twisted Bilayer Graphene. *Phys. Rev. Lett.* **125**, 256804 (2020).

52. J. C. W. Song, M. Y. Reizer, L. S. Levitov, Disorder-assisted electron-phonon scattering and cooling pathways in graphene. *Phys. Rev. Lett.* **109**, 1–5 (2012).

53. R. Bistritzer, A. H. MacDonald, Electronic cooling in graphene. *Phys. Rev. Lett.* **102**, 13–16 (2009).

54. M. W. Graham, S. F. Shi, D. C. Ralph, J. Park, P. L. McEuen, Photocurrent measurements of supercollision cooling in graphene. *Nat. Phys.* **9**, 103–108 (2013).

55. N. M. Gabor *et al.*, Hot carrier-assisted intrinsic photoresponse in graphene. *Science*. **334**, 648–652 (2011).

56. Y. M. Zuev, W. Chang, P. Kim, Thermoelectric and magnetothermoelectric transport measurements of graphene. *Phys. Rev. Lett.* **102**, 1–4 (2009).

57. F. Ghahari *et al.*, Enhanced Thermoelectric Power in Graphene: Violation of the Mott Relation by Inelastic Scattering. *Phys. Rev. Lett.* **116**, 1–5 (2016).

58. J. C. W. Song, M. S. Rudner, C. M. Marcus, L. S. Levitov, Hot Carrier Transport and Photocurrent Response in Graphene. *Nano Lett.* **11**, 4688–4692 (2011).

59. J. C. W. Song, L. S. Levitov, Shockley-Ramo theorem and long-range photocurrent response in gapless materials. *Phys. Rev. B*. **90**, 075415 (2014).

60. X. Xu, N. M. Gabor, J. S. Alden, A. M. Van Der Zande, P. L. McEuen, Photo-thermoelectric effect at a graphene interface junction. *Nano Lett.* **10**, 562–566 (2010).

61. J. D. Joannopoulos, S. G. Johnson, J. N. Winn, R. Meade, *Photonic Crystals: Molding the Flow of Light* (Princeton University Press, 2008).

62. L. Lu, J. D. Joannopoulos, M. Soljačić, Topological photonics. *Nat. Photonics*. **8**, 821–829 (2014).

63. Z. Wang, Y. Chong, J. D. Joannopoulos, M. Soljačić, Observation of unidirectional backscattering-immune topological electromagnetic states. *Nature*. **461**, 772–775 (2009).

64. L. Lu *et al.*, Experimental observation of optical Weyl points. *Science*. **349**, 622–625 (2015).

65. T. Low *et al.*, Polaritons in layered two-dimensional materials. *Nat. Mater.* **16**, 182–194 (2017).

66. D. A. Iranzo *et al.*, Probing the ultimate plasmon confinement limits with a van der Waals heterostructure. *Science*. **360**, 291–295 (2018).

67. D. Jin *et al.*, Infrared Topological Plasmons in Graphene. *Phys. Rev. Lett.* **118**, 1–6 (2017).

68. M. Jung, Z. Fan, G. Shvets, Midinfrared Plasmonic Valleytronics in Metagate-Tuned Graphene. *Phys. Rev. Lett.* **121**, 086807 (2018).

69. G. X. Ni *et al.*, Plasmons in graphene moiré superlattices. *Nat. Mater.* **14**, 1217–1222 (2015).

70. C. R. Woods *et al.*, Commensurate-incommensurate transition in graphene on hexagonal boron nitride. *Nat. Phys.* **10**, 451–456 (2014).

71. Z. Fei *et al.*, Tunneling Plasmonics in Bilayer Graphene. *Nano Lett.* **15**, 4973–4978 (2015).

72. F. Hu *et al.*, Real-Space Imaging of the Tailored Plasmons in Twisted Bilayer Graphene. *Phys. Rev. Lett.* **119**, 1–6 (2017).

73. S. Huang *et al.*, Topologically Protected Helical States in Minimally Twisted Bilayer Graphene. *Phys. Rev. Lett.* **121**, 037702 (2018).

74. A. Drezet *et al.*, Plasmonic Crystal Demultiplexer and Multiports. *Nano Lett.* **7**, 1697 (2007).

75. A. M. Lakhani, M. Kim, E. K. Lau, M. C. Wu, Plasmonic crystal defect nanolaser. *Opt. Express*. **19**, 18237 (2011).

76. F. Zhang, A. H. MacDonald, E. J. Mele, Valley Chern numbers and boundary modes in gapped bilayer graphene. *Proc. Natl. Acad. Sci.* **110**, 10546–10551 (2013).

77. B. Y. Jiang *et al.*, Tunable Plasmonic Reflection by Bound 1D Electron States in a 2D Dirac Metal. *Phys. Rev. Lett.* **117**, 1–10 (2016).

78. J. A. Gerber, S. Berweger, B. T. O. Callahan, M. B. Raschke, Phase-Resolved Surface Plasmon Interferometry of Graphene. *Phys. Rev. Lett.* **055502**, 1–5 (2014).

79. I. Silveiro, A. Manjavacas, S. Thongrattanasiri, F. J. García De Abajo, Plasmonic energy transfer in periodically doped graphene. *New J. Phys.* **15** (2013).

80. S. Dai *et al.*, Efficiency of Launching Highly Confined Polaritons by Infrared Light Incident on a Hyperbolic Material. *Nano Lett.* **17**, 5285–5290 (2017).

81. B. Y. Jiang, L. M. Zhang, A. H. Castro Neto, D. N. Basov, M. M. Fogler, Generalized spectral method for near-field optical microscopy. *J. Appl. Phys.* **119**, 054305 (2016).

82. P. Alonso-González *et al.*, Controlling graphene plasmons with resonant metal antennas and spatial conductivity patterns. *Science*. **344**, 1369–1373 (2014).

83. E. McCann, Asymmetry gap in the electronic band structure of bilayer graphene. *Phys. Rev. B*. **74**, 161403 (2006).

84. A. B. Kuzmenko, I. Crassee, D. Van Der Marel, P. Blake, K. S. Novoselov, Determination of the gate-tunable band gap and tight-binding parameters in bilayer graphene using infrared spectroscopy. *Phys. Rev. B*. **80**, 1–12 (2009).

85. Z. Q. Li *et al.*, Band structure asymmetry of bilayer graphene revealed by infrared spectroscopy. *Phys. Rev. Lett.* **102**, 16–19 (2009).

86. M. B. Lundeberg *et al.*, Tuning quantum nonlocal effects in graphene plasmonics. *Science*. **357**, 187–191 (2017).

87. M. Yankowitz, Q. Ma, P. Jarillo-Herrero, B. J. LeRoy, van der Waals heterostructures combining graphene and hexagonal boron nitride. *Nat. Rev. Phys.* **1**, 112–125 (2019).

88. G. Li *et al.*, Observation of Van Hove singularities in twisted graphene layers. *Nat. Phys.* **6**, 109–113 (2010).

89. Y. Cao *et al.*, Superlattice-Induced Insulating States and Valley-Protected Orbits in Twisted Bilayer Graphene. *Phys. Rev. Lett.* **117**, 1–5 (2016).

90. A. Kerelsky *et al.*, Maximized electron interactions at the magic angle in twisted bilayer graphene. *Nature*. **572**, 95–100 (2019).

91. Y. Xie *et al.*, Spectroscopic signatures of many-body correlations in magic-angle twisted bilayer graphene. *Nature*. **572**, 101–105 (2019).

92. Y. Choi *et al.*, Electronic correlations in twisted bilayer graphene near the magic angle. *Nat. Phys.* **15**, 1174–1180 (2019).

93. Y. Jiang *et al.*, Charge order and broken rotational symmetry in magic-angle twisted bilayer graphene. *Nature*. **573**, 91–95 (2019).

94. S. S. Sunku *et al.*, Photonic crystals for nano-light in moiré graphene superlattices. *Science*. **362**, 1153–1156 (2018).

95. H. Polshyn *et al.*, Large linear-in-temperature resistivity in twisted bilayer graphene. *Nat. Phys.* **15**, 1011–1016 (2019).

96. M. Yankowitz *et al.*, Tuning superconductivity in twisted bilayer graphene. *Science*. **363**, 1059–1064 (2019).

97. A. Uri *et al.*, Mapping the twist-angle disorder and Landau levels in magic-angle graphene. *Nature*. **581**, 47–52 (2020).

98. U. Zondiner *et al.*, Cascade of phase transitions and Dirac revivals in magic-angle graphene. *Nature*. **582**, 203–208 (2020).

99. X. Lu *et al.*, Superconductors, orbital magnets and correlated states in magic-angle bilayer graphene. *Nature*. **574**, 653–657 (2019).

100. M. B. Lundeberg *et al.*, Thermoelectric detection and imaging of propagating graphene plasmons. *Nat. Mater.* **16**, 204–207 (2017).

101. P. Alonso-González *et al.*, Acoustic terahertz graphene plasmons revealed by photocurrent nanoscopy. *Nat. Nanotechnol.* **12**, 31–35 (2017).

102. A. Woessner *et al.*, Electrical detection of hyperbolic phonon-polaritons in heterostructures of graphene and boron nitride. *npj 2D Mater. Appl.*, 1–5 (2017).

103. J. Aizpurua, T. Taubner, F. J. García de Abajo, M. Brehm, R. Hillenbrand, Substrate-enhanced infrared near-field spectroscopy. *Opt. Express*. **16**, 1529 (2008).

104. T. Stauber, P. San-Jose, L. Brey, Optical conductivity, Drude weight and plasmons in twisted graphene bilayers. *New J. Phys.* **15**, 113050 (2013).

105. P. Moon, M. Koshino, Optical absorption in twisted bilayer graphene. *Phys. Rev. B*. **87**, 1–11 (2013).

106. J. Duan *et al.*, High thermoelectricpower factor in graphene/hBN devices. *Proc. Natl. Acad. Sci.* **113**, 14272–14276 (2016).

107. K. W. Post *et al.*, Coexisting first- and second-order electronic phase transitions in a correlated oxide. *Nat. Phys.* **14**, 1056–1061 (2018).

108. E. J. H. Lee, K. Balasubramanian, R. T. Weitz, M. Burghard, K. Kern, Contact and edge effects in graphene devices. *Nat. Nanotechnol.* **3**, 486–490 (2008).

109. D. N. Basov, R. D. Averitt, D. Hsieh, Towards properties on demand in quantum materials. *Nat. Mater.* **16**, 1077–1088 (2017).

110. L. Wang *et al.*, Evidence for a fractional fractal quantum Hall effect in graphene superlattices. *Science*. **350**, 1231–1234 (2015).

111. L. Jiang *et al.*, Manipulation of domain-wall solitons in bi- and trilayer graphene. *Nat. Nanotechnol.* **13**, 1–5 (2018).

112. K. L. Seyler *et al.*, Signatures of moiré-trapped valley excitons in MoSe 2 /WSe 2 heterobilayers. *Nature*. **567**, 66–70 (2019).

113. K. Tran *et al.*, Evidence for moiré excitons in van der Waals heterostructures. *Nature*. **567**, 71–75 (2019).

114. C. Jin *et al.*, Observation of moiré excitons in WSe 2 /WS 2 heterostructure superlattices. *Nature*. **567**, 76–80 (2019).

115. E. M. Alexeev *et al.*, Resonantly hybridized excitons in moiré superlattices in van der Waals heterostructures. *Nature*. **567**, 81–86 (2019).

116. M. Massicotte *et al.*, Picosecond photoresponse in van der Waals heterostructures. *Nat. Nanotechnol.* **11**, 42–46 (2015).

117. A. Das *et al.*, Monitoring dopants by Raman scattering in an electrochemically top-gated graphene transistor. *Nat. Nanotechnol.* **3**, 210–215 (2008).

118. Y. Zeng *et al.*, High-Quality Magnetotransport in Graphene Using the Edge-Free Corbino Geometry. *Phys. Rev. Lett.* **122**, 137701 (2019).

119. S. Carr, S. Fang, P. Jarillo-Herrero, E. Kaxiras, Pressure dependence of the magic twist angle in graphene superlattices. *Phys. Rev. B*. **98**, 085144 (2018).

120. N. N. T. Nam, M. Koshino, Lattice relaxation and energy band modulation in twisted bilayer graphene. *Phys. Rev. B*. **96**, 1–12 (2017).

121. K. Kim *et al.*, Tunable moiré bands and strong correlations in small-twist-angle bilayer graphene. *Proc. Natl. Acad. Sci.* **114**, 3364–3369 (2017).

122. Y. Cao *et al.*, Tunable correlated states and spin-polarized phases in twisted bilayer–bilayer graphene. *Nature*. **583**, 215–220 (2020).

123. M. Cutler, N. F. Mott, Observation of Anderson Localization in an Electron Gas. *Phys. Rev.* **181**, 1336–1340 (1969).

124. T. Stauber, N. M. R. Peres, F. Guinea, Electronic transport in graphene: A semiclassical approach including midgap states. *Phys. Rev. B*. **76**, 205423 (2007).

125. M. Schubert *et al.*, Infrared optical properties of mixed-phase thin films studied by spectroscopic ellipsometry using boron nitride as an example. *Phys. Rev. B*. **56**, 13306–13313 (1997).

126. A. Kucirkova, K. Navratil, Interpretation of Infrared Transmittance Spectra of SiO2 Thin Films. *Appl. Spectrosc.* **48**, 113 (1994).

127. K. P. Nuckolls *et al.*, Strongly correlated Chern insulators in magic-angle twisted bilayer graphene. *Nature* (2020), doi:10.1038/s41586-020-3028-8.

128. L. J. Yin, H. Jiang, J. Bin Qiao, L. He, Direct imaging of topological edge states at a bilayer graphene domain wall. *Nat. Commun.* **7**, 1–6 (2016).

129. S. S. Sunku *et al.*, Nano-photocurrent Mapping of Local Electronic Structure in Twisted Bilayer Graphene. *Nano Lett.* **20**, 2958–2964 (2020).

130. L. J. McGilly *et al.*, Visualization of moiré superlattices. *Nat. Nanotechnol.* **15**, 580–584 (2020).

131. H. Cao *et al.*, Photo-Nernst current in graphene. *Nat. Phys.* **12**, 236–239 (2016).

132. J. D. Caldwell *et al.*, Sub-diffractional volume-confined polaritons in the natural hyperbolic material hexagonal boron nitride. *Nat. Commun.* **5**, 1–9 (2014).

133. E. Yoxall *et al.*, Direct observation of ultraslow hyperbolic polariton propagation with negative phase velocity. *Nat. Photonics*. **9**, 674–678 (2015).

134. S. Dai *et al.*, Subdiffractional focusing and guiding of polaritonic rays in a natural hyperbolic material. *Nat. Commun.* **6**, 1–7 (2015).

135. P. Li *et al.*, Hyperbolic phonon-polaritons in boron nitride for near-field optical imaging and focusing. *Nat. Commun.* **6**, 7507 (2015).

136. R. R. Nair *et al.*, Fine structure constant defines visual transparency of graphene. *Science*. **320**, 1308 (2008).

137. Z. Q. Li *et al.*, Dirac charge dynamics in graphene by infrared spectroscopy. *Nat. Phys.* **4**, 532–535 (2008).

138. C. Tan *et al.*, Realization of a universal hydrodynamic semiconductor in ultra-clean dual-gated bilayer graphene, 1–20 (2019).

139. A. A. Balandin *et al.*, Superior thermal conductivity of single-layer graphene. *Nano Lett.* **8**, 902–907 (2008).

140. R. Mao *et al.*, Phonon engineering in nanostructures: Controlling interfacial thermal resistance in multilayer-graphene/dielectric heterojunctions. *Appl. Phys. Lett.* **101** (2012).

141. Y. Liu *et al.*, Thermal Conductance of the 2D MoS2/h-BN and graphene/h-BN Interfaces. *Sci. Rep*. **7**, 1–8 (2017).

142. G. Cerullo *et al.*, Out-of-plane heat transfer in van der Waals stacks through electron-hyperbolic phonon coupling. *Nat. Nanotechnol.* **13**, 41–46 (2018).

143. M. Koshino, Electronic transmission through AB-BA domain boundary in bilayer graphene. *Phys. Rev. B*. **88** (2013).

144. J. M. Ziman, *Principles of the Theory of Solids* (Cambridge University Press, 1972).

145. L. Brey, T. Stauber, L. Martín-Moreno, G. Gómez-Santos, Nonlocal Quantum Effects in Plasmons of Graphene Superlattices. *Phys. Rev. Lett.* **124**, 257401 (2020).

146. T. Low, P. Y. Chen, D. N. Basov, Superluminal plasmons with resonant gain in population inverted bilayer graphene. *Phys. Rev. B*. **98**, 1–6 (2018).

147. G. Chen *et al.*, Signatures of tunable superconductivity in a trilayer graphene moiré superlattice. *Nature*. **572**, 215–219 (2019).

148. X. Liu *et al.*, Tunable spin-polarized correlated states in twisted double bilayer graphene. *Nature*. **583**, 221–225 (2020).

149. A. Kerelsky *et al.*, Moiréless correlations in ABCA graphene. *Proc. Natl. Acad. Sci.* **118**, e2017366118 (2021).

150. H. Yan *et al.*, Tunable infrared plasmonic devices using graphene/insulator stacks. *Nat. Nanotechnol.* **7**, 330–334 (2012).

151. L. Ju *et al.*, Tunable excitons in bilayer graphene. *Science*. **358**, 907–910 (2017).

152. H. Li *et al.*, Global Control of Stacking-Order Phase Transition by Doping and Electric Field in Few-Layer Graphene. *Nano Lett.* **20**, 3106–3112 (2020).

153. N. Ocelic, A. Huber, R. Hillenbrand, Pseudoheterodyne detection for background-free near-field spectroscopy. *Appl. Phys. Lett.* **89** (2006).

154. Y. Liu *et al.*, Approaching the Schottky–Mott limit in van der Waals metal–semiconductor junctions. *Nature*. **557**, 696–700 (2018).

155. L. A. Jauregui *et al.*, Electrical control of interlayer exciton dynamics in atomically thin heterostructures. *Science*. **366**, 870–875 (2019).

156. S. S. Sunku et al., Hyperbolic enhancement of photocurrent patterns in minimally twisted bilayer graphene. *Nat. Commun.* **12**, 1641 (2021).

157. N. C. H. Hesp et al., Nano-imaging photoresponse in a moire unit cell. *Nat. Commun.* **12**, 1640 (2021).

158. S. Das Sarma, A. Madhukar, Collective modes of spatially separated, two-component, two-dimensional plasma in solids. *Phys. Rev. B*. **23**, 805–815 (1981).

159. R. E. V. Profumo, R. Asgari, M. Polini, A. H. MacDonald, Double-layer graphene and topological insulator thin-film plasmons. *Phys. Rev. B*. **85**, 1–8 (2012).

160. T. Stauber, G. Gómez-Santos, Plasmons and near-field amplification in double-layer graphene. *Phys. Rev. B*. **85**, 1–8 (2012).

161. L. Wang *et al.*, One-dimensional electrical contact to a two-dimensional material. *Science*. **342**, 614–617 (2013).

162. T. J. Wieting, J. L. Verble, Infrared and Raman studies of long-wavelength optical phonons in hexagonal MoS2. *Phys. Rev. B*. **3**, 4286–4292 (1971).

163. R. Kitamura, L. Pilon, M. Jonasz, Optical constants of silica glass from extreme ultraviolet to far infrared at near room temperature. *Appl. Opt.* **46**, 8118 (2007).

164. P. V. Nguyen *et al.*, Visualizing electrostatic gating effects in two-dimensional heterostructures. *Nature*. **572**, 220–223 (2019).

165. P. Steinleitner *et al.*, Direct Observation of Ultrafast Exciton Formation in a Monolayer of WSe 2. *Nano Lett.* **17**, 1455–1460 (2017).